

## ABSTRACT

Title of Dissertation: SOVLENT REACTIVITY AND INTERFACE  
EVOLUTION AT MODEL ELECTRODES  
FOR ENERGY APPLICATIONS

Wentao Song, Doctor of Philosophy, 2016

Dissertation directed by: Professor Janice E. Reutt-Robey  
Department of Chemistry and Biochemistry

The Li-ion rechargeable battery (LIB) is widely used as an energy storage device, but has significant limitations in battery cycle life and safety. During initial charging, decomposition of the ethylene carbonate (EC)-based electrolytes of the LIB leads to the formation of a passivating layer on the anode known as the solid electrolyte interphase (SEI). The formation of an SEI has great impact on the cycle life and safety of LIB, yet mechanistic aspects of SEI formation are not fully understood. In this dissertation, two surface science model systems have been created under ultra-high vacuum (UHV) to probe the very initial stage of SEI formation at the model carbon anode surfaces of LIB.

The first model system, Model System I, is an lithium-carbonate electrolyte/graphite C(0001) system. I have developed a temperature programmed desorption/temperature programmed reaction spectroscopy (TPD/TPRS) instrument as part of my dissertation to study Model System I in quantitative detail. The binding strengths and film growth mechanisms of key electrolyte molecules on model carbon anode surfaces with varying extents of lithiation were measured by TPD. TPRS was further used to track the gases evolved from different reduction products in the early-stage SEI formation. The branching ratio of multiple reaction pathways was quantified for the first time and determined to be 70.% organolithium products vs. 30% inorganic lithium product. The obtained branching ratio provides important information on the distribution of lithium salts that form at the very onset of SEI formation.

One of the key reduction products formed from EC in early-stage SEI formation is lithium ethylene dicarbonate (LEDC). Despite intensive studies, the LEDC structure in either the bulk or thin-film (SEI) form is unknown. To enable structural study, pure LEDC was synthesized and subject to synchrotron X-ray diffraction measurements (bulk material) and STM measurements (deposited films). To enable studies of LEDC thin films, Model System II, a lithium ethylene dicarbonate (LEDC)-dimethylformamide (DMF)/Ag(111) system was created by a solution microaerosol deposition technique. Produced films were then imaged by ultra-high vacuum scanning tunneling microscopy (UHV-STM). As a control, the dimethylformamide (DMF)-Ag(111) system was first prepared and its complex 2D phase behavior was mapped out as a function of coverage. The evolution of three

distinct monolayer phases of DMF was observed with increasing surface pressure — a 2D gas phase, an ordered DMF phase, and an ordered  $\text{Ag}(\text{DMF})_2$  complex phase. The addition of LEDC to this mixture, seeded the nucleation of the ordered DMF islands at lower surface pressures (DMF coverages), and was interpreted through nucleation theory. A structural model of the nucleation seed was proposed, and the implication of ionic SEI products, such as LEDC, in early-stage SEI formation was discussed.

SOLVENT REACTIVITY AND INTERFACE EVOLUTION AT MODEL  
ELECTRODES FOR ENERGY APPLICATIONS

by

Wentao Song

Dissertation submitted to the Faculty of the Graduate School of the  
University of Maryland, College Park, in partial fulfillment  
of the requirements for the degree of  
Doctor of Philosophy  
2016

Advisory Committee:  
Professor Janice E. Reutt-Robey, Chair  
Professor Theodore L. Einstein  
Professor Yu-Huang Wang  
Professor Sang Bok Lee  
Professor John D. Weeks

© Copyright by  
Wentao Song  
2016

## Dedication

This work is dedicated to my mother.

## Acknowledgements

First and foremost, I would like to thank my advisor, Prof. Janice E. Reutt-Robey. Her persistent support, knowledge and patience helped me finish this dissertation. I would not finish this without her support.

I would like to thank Dr. Satyaveda Bharath for teaching me the basics of ultra-high vacuum (UHV) instrument operations. I would also like to thank Dr. Levan Tskipuri for educating me on knowledge of vacuum science and technology. His outstanding instrument building skill enables me to finish Chapter 4 of my dissertation.

I am grateful to my other dissertation committee member: Dr. Yuhuang Wang, Dr. Sang Bok Lee, Dr. Theodore Einstein and Dr. John Weeks.

I am thankful to my friends and co-workers in the Surface Science Group at the University of Maryland during my PhD study: Dr. Qian Shao, Dr. Yilin Wang, Mr. Jonathan Larson and Dr. Bill Cullen.

Finally I would like to thank my parents who showed great understanding, patience, support and encouragement throughout my PhD study.

## Table of Contents

Dedication .....	ii
Acknowledgements .....	iii
List of Tables .....	vi
List of Figures .....	vii
List of Abbreviations .....	ix
Chapter 1 Introduction .....	1
1.1 Energy Issues and Society .....	1
1.2 Electrical Energy Storage (EES) Technology .....	2
1.3 Lithium-ion Battery (LIB): Past and Present .....	4
1.4 Lithium-ion Battery (LIB): Challenges and Opportunities .....	5
1.5 Thesis Overview .....	8
Chapter 2 Experimental Methods .....	11
2.1 Model Systems .....	11
2.2 Enabling Methods for Model Systems .....	13
2.3 Characterization of Model Systems .....	15
2.3.1 Introduction .....	15
2.3.2 Temperature programmed desorption/temperature programmed reaction spectroscopy (TPD/TPRS) .....	15
2.3.3 Scanning Tunneling Microscopy (STM) .....	20
Chapter 3 Adsorption and Reaction Branching of Molecular Carbonates on Lithiated C(0001) Substrates .....	24
3.1 Introduction .....	24
3.2. Experimental Section .....	27
3.3 Results and discussions .....	29
3.3.1. Clean Graphite .....	29
3.3.2. Lithiated Graphite .....	32
3.3.3 Impact of Metallic Lithium .....	35
3.4 Summary .....	38
Chapter 4 Complexation and Phase Evolution at Dimethylformamide-Ag(111) Interfaces .....	40
4.1 Introduction .....	40
4.2 Experimental Section .....	43
4.2.1 Sample Preparation .....	43
4.2.3 XPS Measurements .....	45
4.2.4 Computational Details .....	45
4.3 Results .....	45
4.3.1 Low Coverages: Formation of 2-D gas (Phase I) .....	45
4.3.2 Medium Coverages: Island Formation and Growth (Phase II) .....	48
4.3.3 Near-Saturation Monolayer: Condensation of Ag(DMF) <sub>2</sub> islands (Phase III) .....	51
4.3.4 Saturated Monolayer: DMF (Phase II) – Ag(DMF) <sub>2</sub> (Phase III) Coexistence .....	52
4.4 Discussion .....	54
4.4.1 Composition and Phase Diagram .....	54



4.4.2 Phase Evolution and Surface Energetics.....	57
4.4.3 Coordination Chemistry of Ag: Surface vs. Solution and Solid State.....	59
4.5 Summary .....	60
Chapter 5 Lithium Ethylene Dicarboxylate (LEDC) – Dimethylformamide (DMF) Monolayer Films on Ag(111) .....	62
5.1 Introduction.....	62
5.2 Experimental Methods .....	64
5.3 Results.....	66
5.3.1 X-ray diffraction studies of bulk LEDC .....	66
5.3.2 STM imaging of microaerosol-deposited LEDC/DMF films .....	67
5.4 Discussion .....	68
5.5 Summary .....	72
Chapter 6 Summary and Outlook .....	74
Appendices.....	80
Appendix A. Temperature Calibration of the Constructed TPD/TPRS System.....	81
Appendix B. The MATLAB Code for the TPD/TPRS Kinetics Simulation Utilizing the Runge–Kutta Numerical Integration Method .....	85
Appendix C .....	90
Bibliography .....	98

## List of Tables

Table 3.1. EC Decomposition Products on Li(metal)/C(0001) and Their Branching Ratios Based upon 1.5 L EC (in Absolute Coverage Units).....	38
Table 4.1. Composition and Structure of Different Phases .....	55

## List of Figures

Figure 1.1. Energy density of different rechargeable batteries. <sup>7</sup> .....	3
Figure 1.2. A schematic of the Li-ion battery (LIB). <sup>13</sup> .....	5
Figure 1.3. The composition of SEI at the carbon anode surfaces in LIB. <sup>27</sup> .....	8
Figure 2.1. Molecular formula of ring carbonates and linear carbonates used in the Li-ion battery (LIB). .....	12
Figure 2.2. Molecule formula and structure of lithium ethylene dicarbonate (LEDC). .....	12
Figure 2.3. Schematic illustration of pulsed microaerosol deposition system, composed of syringe pump, nebulizer (1), cloud chamber (2), pulsed valve (3) and differential pumped chamber with skimmers. <sup>30</sup> .....	14
Figure 2.4. Schematic illustration of a quadrupole mass analyzer (QMA). .....	16
Figure 2.5. Control setup of temperature programmed desorption/temperature programmed reaction spectroscopy (TPD/TPRS). .....	18
Figure 2.6. TPD of Pentane from C (0001), monitored at $m/z = 43$ and a ramp rate of 1 K/s. ....	19
Figure 2.7. Schematic illustration of scanning tunneling microscope, showing the raster scanning of the STM tip (upper left) and tunneling junction (lower right). ....	21
Figure 3.1. TPD spectra of EC desorption from C(0001). Inset shows the Arrhenius representation of the leading edge of the spectra, whose slope yields an adsorption energy of $E_d = 0.60 \pm 0.06$ eV. Spectra were collected by monitoring $m/q = 43$ at the heating rate of 1 K/s. For clarity, high frequency noise is removed by a low pass filter. ....	30
Figure 3.2. TPD spectra of DMC desorption from C(0001). Inset shows the simulation of DMC monolayer desorption via first-order desorption kinetics with an adsorption energy value adjusted of $0.64 \pm 0.05$ eV. Spectra were collected by monitoring $m/q = 45$ at the heating rate of 1 K/s. ....	31
Figure 3.3. TPD spectra of EC on lithiated C(0001) 0.10 L – 0.30 L (left panel) and 0.60 L – 1.4 L (right panel), collected by monitoring $m/q = 43$ at the heating rate of 1 K/s. ....	32
Figure 3.4. TPD spectra of DMC on lithiated C(0001) 0.12 L – 0.40 L, collected by monitoring $m/q = 45$ at the heating rate of 1 K/s. ....	33
Figure 3.5. TPD spectrum of EC on $\text{Li}^+/\text{C}(0001)$ (black), and simulations of the 1st order desorption energy profiles at the lower (blue) and upper (red) bounds of the experimental spectrum. ....	34
Figure 3.6. Temperature programmed reaction spectra (TPRS) of EC reduction products. Upper trace is $\text{C}_2\text{H}_4$ (daughter ion $m/z = 26$ ); middle trace is $\text{C}_2\text{H}_4\text{O}$ (daughter ion $m/z = 42$ ); lower trace ( $m/z = 44$ ) shows desorption peaks from both $\text{CO}_2$ (570 K maximum) and $\text{C}_2\text{H}_4$ (600 K maximum) and a corresponding fit to asymmetric logistical functional forms to quantify the $\text{CO}_2$ (green curve) and $\text{C}_2\text{H}_4\text{O}$ (blue curve) products. ....	36
Figure 4.1. Experimental schematic of pulsed microaerosol molecular beam deposition of DMF on Ag(111). The molecular structure of DMF is shown in the upper right inset. ....	44

Figure 4.2. UHV-STM images (400 nm × 400 nm) of Ag(111) before (Figure 4.2a) and after (Figure 4.2b) deposition of $0.43 \pm 0.01$ DMF (all forms)/nm <sup>2</sup> , delivered by 2000 pulses of DMF microaerosol entrained in N <sub>2</sub> .	46
Figure 4.3. Core level XPS spectra of (a) N 1s, (b) C 1s, and (c) O 1s, fitted with peaks having a 70% Gaussian and 30% Lorentzian peak shape.	48
Figure 4.4. UHV-STM images (200 nm × 200 nm) following sequential DMF deposition: (a-b) 4000 pulses to a DMF coverage of $\Gamma_{\text{DMF (all forms)}} = 0.86 \pm 0.01$ molecules/nm <sup>2</sup> reveals nucleation of elongated islands at upper step edges (a) and on large terraces (b); (c-d) 8000 pulses to a DMF coverage of $\Gamma_{\text{DMF (all forms)}} = 1.72 \pm 0.02$ molecules/nm <sup>2</sup> reveals continued growth and change in island aspect ratio.	49
Figure 4.5. (a) Molecularly resolved UHV-STM image (3 nm × 3 nm) of Phase II and (b) the DFT + vdW computational relaxed model of DMF/Ag(111). Within this structural model the N-C=O group corresponds to the arc-shaped protrusion in the STM image.	50
Figure 4.6. Onset condensation of Ag(DMF) <sub>2</sub> complexes (Phase II) at $\Gamma_{\text{DMF (all forms)}} = 2.15 \pm 0.02$ molecules/nm <sup>2</sup> : (a) 200 nm × 200 nm image and (b) 20 × 20 nm image reveal coexistence of 2-D gas (Phase I), DMF island phase (Phase II) and Ag(DMF) <sub>2</sub> islands (Phase III).	51
Figure 4.7. STM images of DMF-Ag(111) interface at saturation coverage: (a) Large scale image shows coexistence of Phase II and Phase III; (b) Higher resolution image shows re of double-row structures (Phase III) along the substrate $[1\bar{1}0]$ direction; (c) Higher resolution magnified image of double-row structures; (d) Top-view and side-view of Ag(DMF) <sub>2</sub> double-row structural models.	53
Figure 4.8. Surface Pressure – Composition phase diagram of the binary DMF-Ag(DMF) <sub>2</sub> phases on Ag(111) at room temperature. $x_{\text{DMF}} = \Gamma_{\text{DMF}} / (\Gamma_{\text{DMF}} + \Gamma_{\text{Ag(DMF)}_2})$ . Actual measured points shown as squares. Surface pressure is estimated from Eq. (4.1).	56
Figure 5.1. Molecular structures of ring carbonates and linear carbonates as well as SEI early-stage product—lithium ethylene dicarbonate (LEDC).	63
Figure 5.2. X-ray diffraction data for bulk LEDC: synchrotron data (blue trace) and conventional data (green trace).	66
Figure 5.3.(a) Aerosol deposited films from LEDC-saturated DMF solution: STM image (200 nm × 200 nm) at a DMF coverage of $0.22 \pm 0.01$ molecules/nm <sup>2</sup> revealed two coexisting phases—2D gas (Phase I) and ordered DMF islands (Phase II), (b) coverage of ordered DMF islands (Phase II) plotted as a function of DMF coverage.	67
Figure 5.4. DMF coverage-temperature phase diagram in the submonolayer $0 - 1.00 \pm 0.05$ DMF/nm <sup>2</sup> regime. The 2D gas-ordered DMF phase boundary shift is indicated by the red arrow.	68
Figure 5.5. UHV-STM image (10 nm × 10 nm) of LEDC-seeded DMF islands with $0.43 \pm 0.01$ DMF/nm <sup>2</sup> on Ag(111). White grid shows the DMF unit cell repeat. Protrusions encircled in green are attributed to solvated LEDC.	71
Figure 5.6. Structural model of DMF-solvated LEDC on Ag(111). The white grid shows the DMF unit cell repeat and the green ellipse shows solvated LEDC.	72

## List of Abbreviations

2D	two-dimensional
3D	three-dimensional
D	Debye
DMC	dimethyl carbonate
DMF	dimethyl formamide
DFT	density functional theory
EC	ethylene carbonate
EES	electrical energy storage
LIB	Li-ion battery
LEDC	lithium ethylene dicarbonate
LEG	lithium ethylene glycolate
MOF	metal organic framework
PID	proportional–integral–derivative
PVD	physical vapor deposition
QMA	quadrupole mass analyzer
SEI	solid electrolyte interphase
STM	scanning tunneling microscopy
TPD	temperature programmed desorption
TPRS	temperature programmed reaction spectroscopy
TDS	thermal desorption spectroscopy
UHV	ultra-high vacuum



# Chapter 1 Introduction

## 1.1 Energy Issues and Society

Energy is the heart of modern civilization, and the demand for energy is constantly expanding as civilization advances. According to the International Energy Agency (IEA) Key World Energy Statistics 2015 Report<sup>1</sup>, the global total final energy consumption in 2013 is 9301 Mtoe (1 Mtoe = 11.63 TWh or terawatt-hour). This consumption approximately doubles the total energy consumption of 1973 (4667 Mtoe), showing the dramatic increase in energy consumption over the last 40 years. It is estimated that by the year 2040 the world energy consumption will reach 10748-12487 Mtoe. The ever increasing energy consumption poses serious challenges to the development of modern civilization. These challenges include: (i) a limited total energy supply. Currently the major source of energy is from the combustion of fossil fuels (e.g. oil, natural gas, coal). Formed in pre-historic eras, the total supply of these fossil fuels is fundamentally limited; (ii) environment problems caused by the combustion of fossil fuels. Burning coals and gasolines leads to serious air pollution problems in developing countries like China and India. More importantly, the greenhouse gas CO<sub>2</sub> is the major cause of the global warming effect, which impacts both developing and developed countries alike. The disruptive effects of global warming have already begun to appear in the form of rising sea levels<sup>2,3</sup>, more intense hurricanes<sup>4</sup> and heat waves<sup>5</sup>. There are several approaches to tackle these issues: (i) improve energy use efficiency, (ii) develop and adopt renewable energies (solar, wind, geothermal etc.). The majority of renewable energies are the direct or indirect

form of solar energy, originating from the nuclear fusion in the sun. Intense research and development efforts have been exerted to harvest the renewable energy, and an increasing number of renewable energy facilities have been put into use. These efforts, however, have been greatly impeded by one major obstacle—the intermittent nature of these renewable energies. To overcome this obstacle and achieve the green energy dream for humankind, science and technology breakthroughs in one key field, energy storage, especially large scale energy storage, are imperative.

## 1.2 Electrical Energy Storage (EES) Technology

Among all energy storage technologies, electrical energy storage (EES) has several advantages: (i) consumption of electrical energy does not have associated emission and electrical energy is therefore a clean energy, (ii) electric energy provides higher energy use efficiency compared to internal combustion engines due to minimal thermal energy waste, (iii) electrical energy systems can be directly integrated with electronic systems for advanced functionality (e.g. smart power management system). Therefore the electrical energy storage system becomes the natural choice for energy storage applications. Types of EES include the following<sup>6</sup>: (i) mechanical (e.g. compressed air), (ii) chemical (e.g. hydrogen and batteries), (iii) electrical (e.g. capacitors and supercapacitors), (iv) thermal (e.g. molten salt).

Batteries are the most widely used EES systems. A battery consists of one or multiple electrochemical cells. A single electrochemical cell is composed of a negative electrode (cathode), a positive electrode (anode) and electrolyte solution of ionic salts. During a discharge, the electrons flow from the anode to the cathode through the external circuit. The electrochemistry of the discharge is not reversible for



primary batteries, and reversible for secondary (i.e. rechargeable) batteries. The reusable property of the secondary batteries makes for economical use and wide applications in various areas, such as lead-acid batteries in vehicles and Li-ion batteries in portable electronic devices.

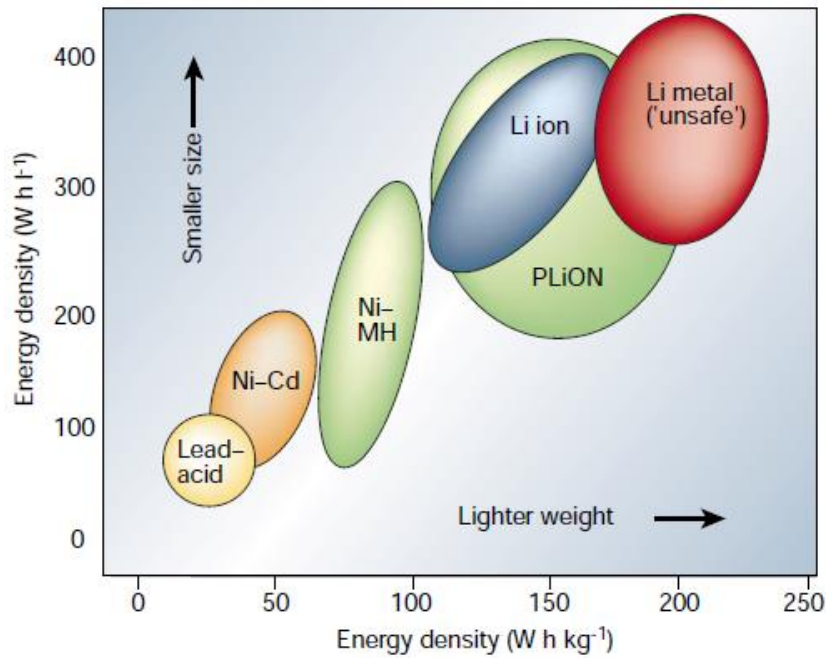
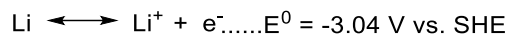


**Figure 1.1.** Energy density of different rechargeable batteries.<sup>7</sup>

There are several major dimensions to measure the performance of the rechargeable batteries: the capacity, the cell potential, the energy density, the power density, and the cycle life. The capacity is total amount of electrical charge in the cell (unit: Ah), the cell potential (unit: V) is determined by the internal electrochemistry of the cell, the energy density is the amount of electrical energy per unit of weight or volume (unit: Wh kg<sup>-1</sup> or Wh l<sup>-1</sup>), the power density is the amount of electrical power output per unit of weight or volume (unit: W kg<sup>-1</sup> or W l<sup>-1</sup>), the cycle life (unit: No. of cycles) is the number of charge/discharge cycles that the battery operates to retain 80% of its original capacity. The Li-ion battery (LIB) stands out among various

rechargeable batteries in terms of energy/power density (Figure 1.1) and has reached cycle life as high as ~1000 cycles commercially<sup>8</sup>. These optimal properties make it widely used as the power source for portable electronic device and a promising solution for larger scale energy storage.

### 1.3 Lithium-ion Battery (LIB): Past and Present



**Scheme 1.1.** Half-cell electrochemical reaction of Li.

The central concept of the LIB is based on the half-cell electrochemical reaction of Li (Scheme 1.1). Lithium is the third element in the periodic table and 25th most abundant element in the earth's crust.<sup>9</sup> It is one of the most electropositive electrode materials ( $E^0 = -3.04 \text{ V}$  vs. standard hydrogen electrode (SHE)) and the lowest-density metallic element (molecular weight:  $6.94 \text{ g}\cdot\text{mol}^{-1}$ , density  $\rho = 0.53 \text{ g}\cdot\text{cm}^3$ ). These properties give the LIB a relatively high energy density and low cost. Lithium metal was first used as an electrode material in the 1970s in rechargeable battery systems<sup>10,11</sup>, but the Li dendrite formation at the metallic lithium-liquid electrolyte interface during charge-discharge cycles causes serious safety concerns<sup>7</sup>. Lithium metal electrode was later replaced by lithium intercalated carbonaceous material-graphite to solve the safety problem. This progress, together with the discovery of a series of  $\text{Li}^+$  host materials ( $\text{Li}_x\text{MO}_2$ ,  $\text{M} = \text{Co}, \text{Ni}$  or  $\text{Mn}$ ) by Goodenough in 1980<sup>12</sup>, and of organic carbonate liquid electrolyte, making the first commercial Li-ion battery available in 1986 by Sony Corporation.<sup>7</sup>

The cathode material of the Li-ion battery is a transition metal oxide (e.g. cobalt oxide) and the anode material is typically graphite, both acting as hosts of the charge

carrier- $\text{Li}^+$  (Figure 1.2). The metallic current collectors deliver electrons from/to the electrodes. The charge separator is a  $\text{Li}^+$  permeable but electron insulating membrane used to physically separate the cathode and the anode. The liquid electrolyte is comprised of a mixture of aprotic polar organic compounds in which lithium ionic compounds such as  $\text{LiPF}_6$  are soluble. Importantly, lithium ions can be transported in the electrolyte phase, but electron transport is blocked and forced to traverse an external circuit. In the discharging mode of the LIB,  $\text{Li}^+$  are transported from the anode to the cathode and electrons concurrently flow into the cathode through outside circuit. In the charging mode of the LIB, electrons are pumped into the anode, driving  $\text{Li}^+$  from the cathode to the anode through the electrolyte phase.

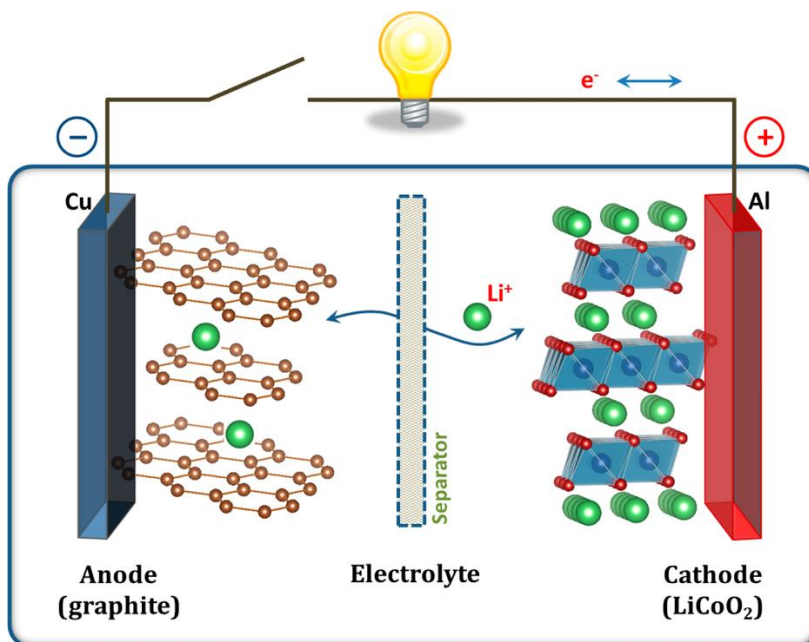


**Figure 1.2.** A schematic of the Li-ion battery (LIB).<sup>13</sup>

#### 1.4 Lithium-ion Battery (LIB): Challenges and Opportunities

Despite the widespread applications of LIBs as energy storage devices, challenges exist to hinder its extension to larger-scale applications (e.g. electric vehicles and

power grid storages). These challenges include limited energy density, limited power density, limited cycle life and safety.<sup>14</sup> These challenges also pose great opportunities to improve the performance of LIB in different aspects.

The limited energy density is attributed to the electrode materials. New electrode materials-silicon (Si)<sup>15</sup>, tin (Sn)<sup>16</sup>, composite materials<sup>17</sup>, etc., have been tested. A typical example is Si, and it has been suggested to replace graphite due to much higher energy density (4,200 mAh g<sup>-1</sup>), more than 10 times that of graphite (372 mAh g<sup>-1</sup>).<sup>18</sup> The problem with Si is that the volume expansion of bulk Si causes pulverization of this electrode during Li-ion insertion. To overcome this problem, new material architectures, such as silicon nanostructures<sup>19</sup> and C-Si composites materials<sup>20</sup>, have been developed and tested to accommodate the volume expansion of Si. Already, start-up companies are working on lowering the manufacturing cost of those research prototypes in order to push them to the market in the near future.

The cycle life is mainly due to electrolyte-electrode interactions. The conventional electrolyte is the aprotic polar organic carbonate liquid electrolyte. One key factor that determines the cycle life and safety of the LIB is the occurrence of side chemical reactions at the electrode-electrolyte interface. These side reactions involve the decomposition of the organic electrolyte at the electrode surface and lead to a buildup of a solid layer on the electrode surface known as the solid electrolyte interphase (SEI). The formation of a thick SEI layer (30-50 nm) acts as an electron insulator, preventing further reductive decomposition of the electrolyte. The SEI layer is Li-ion conducting, which allows LIBs with SEI films to remain functional during charge/discharge cycles. Despite the ability of the SEI to passivate the electrode, its

continual dissolution into the electrolyte and formation at the electrode consumes the available  $\text{Li}^+$  and leads to the capacity fade of LIBs. The SEI-related side reactions also affect the safety and stability of LIBs. Under some circumstances, the chemical reactions can cause a thermal runaway, leading to explosion of LIBs. Numerous such accidents related to LIBs have been reported by the media.

Multitude efforts have been exerted to improve the performance of the electrolyte: (i) liquid electrolyte additives have been tested and proven useful to improve the cycling performance, e.g. vinylene carbonate (VC)<sup>21</sup>, fluoroethylene carbonate (FEC)<sup>22</sup>, both being derivatives of ethylene carbonate (EC). (ii) other classes of electrolytes other than the liquid class is another major area of intensive research, which include polymers and polymer gels, solid ceramics, molten salts and others. Those classes of electrolytes typically have higher electrolyte-electrode interface stability than that of the liquid electrolyte. An example of the polymer electrolyte is poly-ethylene oxide (PEO) based electrolyte.<sup>23</sup> Notable solid ceramics electrolyte materials include: LiPON, Li garnet and LGPS. LiPON ( $\text{Li}_x\text{PO}_y\text{N}_z$  where  $x = 2y+3z-5$ ) is an amorphous material with a Li-ion conductivity of  $\sim 1 \times 10^{-6}$  S/cm at 25°C. Li garnet is a crystal structure family (example composition:  $\text{Li}_7\text{La}_3\text{Zr}_2\text{O}_{12}$ ) with a higher Li-ion conductivity ( $\sim 1 \times 10^{-3}$  S/cm) than LiPON. LGPS ( $\text{Li}_{10}\text{GeP}_2\text{S}_{12}$ ) is a crystalline material that represents a breakthrough in Li-ion conductivity ( $\sim 1 \times 10^{-2}$  S/cm at 25 °C), surpassing that of the typical liquid electrolyte in LIB.<sup>24</sup> Despite the great progress in the field, the overall performance of the polymer and solid electrolyte could still not match that of the liquid electrolyte, which is still under use and therefore will be the focus of my dissertation.

The composition of the SEI formed at the liquid electrolyte-electrode interface is a very complex mixture of inorganic and organic lithium salts as well as organic materials. (Figure 1.3) To understand this complex mixture, it is wise to divide the development of the SEI into different stages. The very initial stage of SEI formation creates monolayers in direct contact with the graphite anode surface, providing mechanical attachment and optimal Li-ion tunneling properties. It is natural to select this stage as the main target of study. As a side note, the SEI could also be formed at the cathode surface.<sup>25</sup> However the greater thickness (~50 nm)<sup>26</sup> at the graphite anode surface makes it a greater issue for capacity fading that demands research.

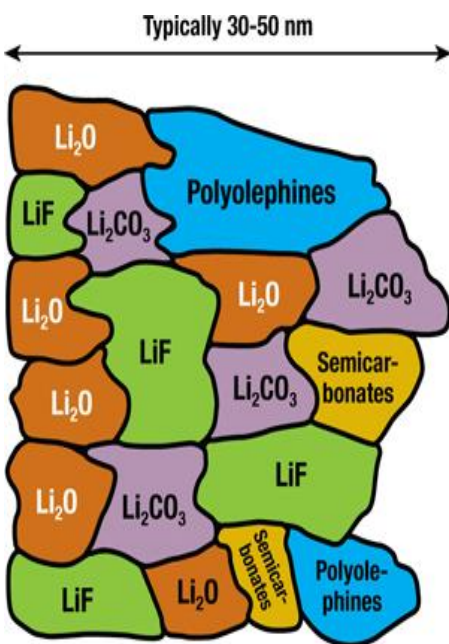


**Figure 1.3.** The composition of SEI at the carbon anode surfaces in LIB.<sup>27</sup>

## 1.5 Thesis Overview

This dissertation explores the reductive decomposition of select molecular carbonates at model carbon anode surfaces. By utilizing the techniques of UHV surface science, we are able to provide new insights on the earliest (sub-monolayer to

monolayer) stage of SEI formation, quantify the branching of decomposition pathways. We performed related structural investigations of select organolithium compounds which are key components in early-stage SEI formation. During this research, we discovered that the highly polar organic solvents needed for structural investigations of neat lithium ethylene dicarbonate films, react spontaneously with silver electrodes to form monolayer films of silver-solvent coordination compounds. An added focus of this dissertation is the detailed characterization of solvent-induced monolayer phases of Ag(111) electrode surfaces.

The overview of my PhD thesis is as follows:

In Chapter 2, the experimental methods and related instrumentations are articulated. The model systems under ultra-high vacuum (UHV) to simulate the very initial stage of SEI formation are introduced. The enabling methods to create the model systems: physical vapor deposition (PVD) and liquid microaerosol deposition methods are presented. The two major surface science techniques to characterize the model systems-temperature programmed desorption / temperature programmed reaction spectroscopy (TPD/TPRS) and scanning tunneling microscopy (STM) are described. The construction of a custom TPD/TPRS system will be specifically described in greater detail since it is an important contribution from my dissertation work.

Chapter 3 provides the first quantitative study of the electrolyte decomposition processes that occur at the initial stage of SEI formation. Ultra-thin (monolayer) model SEI layers are formed by controlled deposition of lithium and organic carbonate electrolytes on the single crystal graphite C(0001) surface. I investigated

the detailed interactions between the electrolytes and model anode surfaces with varying extent of lithiation: (i) clean C(0001), (ii)  $\text{Li}^+/\text{C}(0001)$ , (iii)  $\text{Li}(s)/\text{C}(0001)$ . New information (adsorption energies, reaction branching ratios, structure of the solvent at the interface) were obtained through quantitative analysis of collected TPD/TPRS data.

Chapter 4 and Chapter 5 are based on a key component-lithium ethylene dicarbonate (LEDC) in the ultra-thin model SEI layers created in Chapter 3. The model SEI layer is a complex mixture that precludes atomic-level structural insights. I thus select a single organolithium salt component for more detailed characterization of its properties and role in the initial stage SEI formation. The pure LEDC is moisture sensitive organolithium salt, obtained in pure form through organic synthesis. In order to control film formation, LEDC was dissolved in dimethylformamide (DMF) for aerosol deposition on Ag(111). Chapter 4 examines the interaction between the solvent DMF and Ag(111) in the absence of organolithium solutes, while Chapter 5 presents STM structural studies of monolayer film generated from LEDC-DMF deposition. We reveal that LEDC seeds the nucleation of DMF film structures, and present structural models.

Chapter 6 will give a summary and an outlook for future work.



## Chapter 2 Experimental Methods

### 2.1 Model Systems

The solid electrolyte interphase (SEI) formation at the anode of the Li-ion battery (LIB) is a complex process and it is difficult to monitor the surface physical/chemical changes *in-situ*. To understand this complex process, model systems were created under an UHV environment to simulate the interphase onset in the LIB. It is worth noting that the model system created under UHV is different from the real solid-liquid interface, since the existence of liquid would make UHV impossible. Despite the difference, the UHV model system allows us to simplify the complicated liquid electrolyte-electrode phenomenon and study key aspects of the interphase in a well-defined manner.

In my dissertation, two model systems were created. Model system I is composed of three key components: the solid electrode surface—graphite C(0001), the carbonate electrolytes and lithium. Graphite is the anode material of the commercial available LIB and C(0001) is its basal plane. Here a highly oriented pyrolytic graphite (HOPG) (Micromash, Grade A) was used as the substrate. The carbonate electrolytes used in commercially available LIB's are usually a mixture of ethylene carbonate (EC) and members of the linear carbonate family (Figure 2.1). In Model System I, dimethylcarbonate (DMC) was used as a representative of the linear carbonate family.

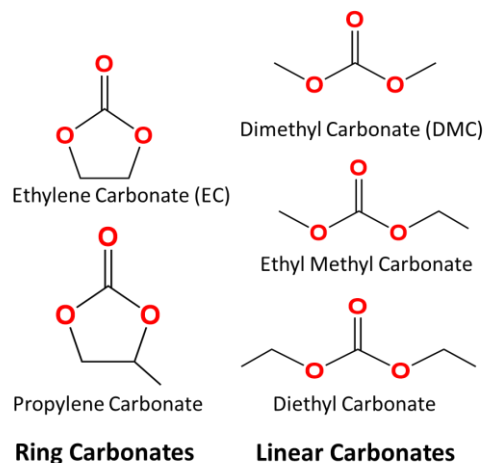


**Figure 2.1.** Molecular formula of ring carbonates and linear carbonates used in the Li-ion battery (LIB).

The Li-carbonate electrolyte/C(0001) model system (Model System I) provided the opportunity to study the interface with advanced surface spectroscopy methods, revealing the detailed interactions between the electrode and the electrolyte molecules. The results show that chemical reactions between lithiated graphite and carbonate electrolyte have multiple reaction pathways, yielding different carbonate electrolyte reduction products. Among the carbon electrolyte reduction products, one reduction product of ethylene carbonate (EC), lithium ethylene dicarbonate (LEDC), draws special attention.<sup>28</sup> (Figure 2.2)

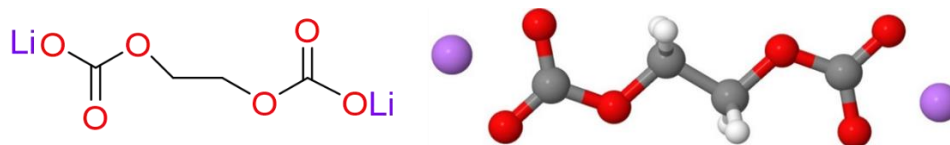


**Figure 2.2.** Molecule formula and structure of lithium ethylene dicarbonate (LEDC).

LEDC is the initial product of EC reduction and appears to play a key role in stabilizing the solid electrolyte interphase (SEI). Experiment and theory efforts have

been exerted to study this molecule, yet its atomically detailed structure in bulk and SEI form have yet to be determined.

In my dissertation, the deposition of LEDC on model electrode surface has been explored under well-defined conditions. Ag(111) was used as the substrate in the deposition studies. Ag(111) was used as the substrate due to its stability, weak interaction with LEDC, making it highly amenable to structural studies by UHV-STM imaging. The polar solvent dimethylformamide (DMF) was used to dissolve LEDC for material delivery in an aerosol deposition to Ag(111). This extended model system: LEDC-DMF/Ag(111) is referred to as Model System II.

## 2.2 Enabling Methods for Model Systems

In Model System I (Li-carbonate electrolyte/C(0001)), electrolyte molecules were deposited on the graphite C(0001) substrate using physical vapor deposition (PVD). The vapor pressure of EC (0.02 mmHg, 36.4 °C) and DMC (18 mmHg, 21.1 °C) permit the PVD method on a clean HOPG substrate through an UHV leak valve. The deposition coverage could be controlled by both the deposition gas pressure and the deposition time. The typical deposition gas pressure ranged from  $1 \times 10^{-9}$  Torr to  $1 \times 10^{-6}$  Torr, as measured by an ionization gauge. The reported deposition exposure is in units of Langmuirs ( $1 \text{ L} = 1 \times 10^{-6} \text{ Torr}\cdot\text{s}$ , where  $1 \text{ L} \approx 1$  monolayer for an assumed stick coefficient of 1). Near unity sticking coefficients are expected for substrate with reduced temperature of  $\sim 100 \text{ K}$ , as per the present study.

In Model System II (LEDC-DMF/Ag(111)), LEDC is a solid organolithium salt at room temperature and its physical properties render it unsuitable for PVD. The thermal decomposition temperature of LEDC occurs at 120°C, before the temperature

of its solid to liquid phase transition.<sup>29</sup> To enable LEDC deposition, a different deposition method—the microaerosol liquid deposition technique was utilized.

A microaerosol liquid deposition system was previously constructed (Figure 2.3) and used for this work.<sup>30</sup> To perform the deposition, LEDC was first dissolved in the aprotic polar organic solvent dimethylformamide (DMF) to form a LEDC/DMF solution (concentration ~0.4 M). The solution was then used as the deposition material and placed into a glass syringe (Hamilton 10 ml) controlled by a syringe pump (Harvard Apparatus 11 Plus). The ejected solution was subsequently mixed with dry nitrogen gas (typical gas pressure 10-20 psi) in a glass nebulizer to form a microaerosol mist. The microaerosol mist was next size-separated in a cloud chamber (Glass Expansion) and introduced into the differentially pumped chamber through a computer-controlled solenoid molecular beam valve (1mm orifice). The resultant molecular beam passed through successive differentially pumped chambers and was further defined by two skimmers before the beam reached the substrate surface.

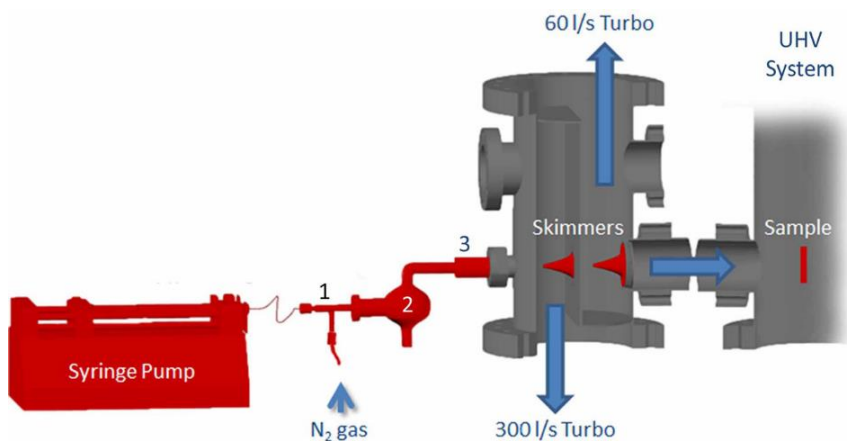


**Figure 2.3.** Schematic illustration of pulsed microaerosol deposition system, composed of syringe pump, nebulizer (1), cloud chamber (2), pulsed valve (3) and differential pumped chamber with skimmers.<sup>30</sup>

## 2.3 Characterization of Model Systems

### 2.3.1 Introduction

A variety of surface science techniques were applied to characterize the aforementioned model systems. These techniques include: Auger electron spectroscopy (AES), x-ray photoelectron spectroscopy (XPS), low energy electron diffraction (LEED), temperature programmed desorption/temperature programmed reaction spectroscopy (TPD/TPRS), atomic force microscopy (AFM) and scanning tunneling microscopy (STM). The TPD/TPRS is the major characterization tool for Model System I (Li-carbonate electrolyte/C(0001)) and I constructed the TPD/TPRS instrumentation as part of my dissertation. Therefore the TPD/TPRS and its construction process will be discussed in detail in the following section. The STM is the major characterization tool for Model System II (LEDC-DMF/Ag(111)) and a section will be devoted to introducing the STM.

### 2.3.2 Temperature programmed desorption/temperature programmed reaction spectroscopy (TPD/TPRS)

(TPD/TPRS) is a powerful characterization tool for Model System I. The physical/chemical interactions between the electrolyte and Li-Graphite in the few monolayers of electrolyte regime requires detection and identification of different chemical species with high sensitivity as a function of temperature. The mass spectrometer (typically a quadruple mass analyzer, QMA) used in TPD/TPRS provides accurate mass-to-charge ( $m/z$ ) ratio filtering and reaches sensitivity as high as  $\sim 10^{-6}$  monolayers/cm<sup>2</sup><sup>31</sup>. The QMA consists of an ionizer, four poles and an electron multiplier for signal enhancement (Figure 2.4). When gas phase

molecules/atoms enter the mass spectrometer, they are ionized in the ionizer, and then the ionized atoms or molecules are transmitted to the quadrupole, where a combination of electric/magnetic fields filter particles of a specific mass to charge ratio ( $m/z$ ). The ionized atoms/molecules then reach the electron multiplier, generating  $10^6$  electrons/ion for the collector. The high-resolution and high sensitivity render the QMA one of most widely applied tools in surface science research. In my dissertation, the mass spectrometer used is the Pfeiffer Vacuum QME 200, which has an  $m/z$  range of 0-200 amu/charge.

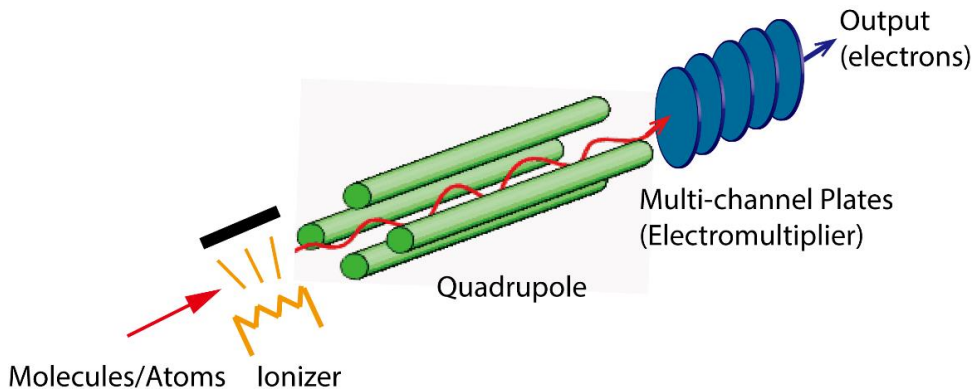


**Figure 2.4.** Schematic illustration of a quadrupole mass analyzer (QMA).

The TPD technique is also referred to as thermal desorption spectroscopy (TDS). Atoms/molecules desorb from the surface and enter into the gas phase by thermal excitation, hence the name. To enable quantitative analysis, the sample is heated linearly at a fixed rate, with typical heating rates ranging from 0.1 K/s – 20 K/s. In my system, the constant heating rate is achieved by a proportional-integral-derivative (PID) controlled feedback heating system. The heating system is composed of a tungsten grid pancake-style sample heater (Thermionics) in the ultra-high vacuum (UHV) chamber, a programmable power supply, a type-K thermocouple spot-welded

to the sample holder, and a computer system that monitors the temperature and sends the calculated real-time feedback signals to the power supply. As the temperature of the sample is ramped, atoms/molecules or adsorbates on the surface overcome the barrier to desorption, and enter into the gas phase. A conical shield was designed to guarantee that only adsorbates from the sample surface enter into the ionizer region, increasing the measurement sensitivity. The TPD system diagram is shown in Figure 2.5. The apparatus used for TPD/TPRS experiment featured a vacuum loadlock to enable sample exchange. Consequently the thermocouple was attached to the stationary sample holder. The sample (1cm × 1cm) was mounted on a stainless steel sample plate (Thermionics). The distance from the sample plate to the thermocouple was ~2 mm. Since the thermocouple was not attached directly to the sample, a temperature calibration was needed to relate the thermocouple read-out temperature to the actual sample temperature. Linear alkanes (mass range: 72-142 amu) desorb from graphite surfaces with sharp desorption features that span the 100-350 K temperature range of interest. For our calibration, TPD spectra were collected for  $C_nH_{2n+2}$ , where  $n = 5-10$ . The TPD spectra for pentane is shown in Figure 2.6. Calibration curves were obtained to relate actual surface temperature to the measured thermocouple temperature value. Calibration details are summarized in Appendix A.

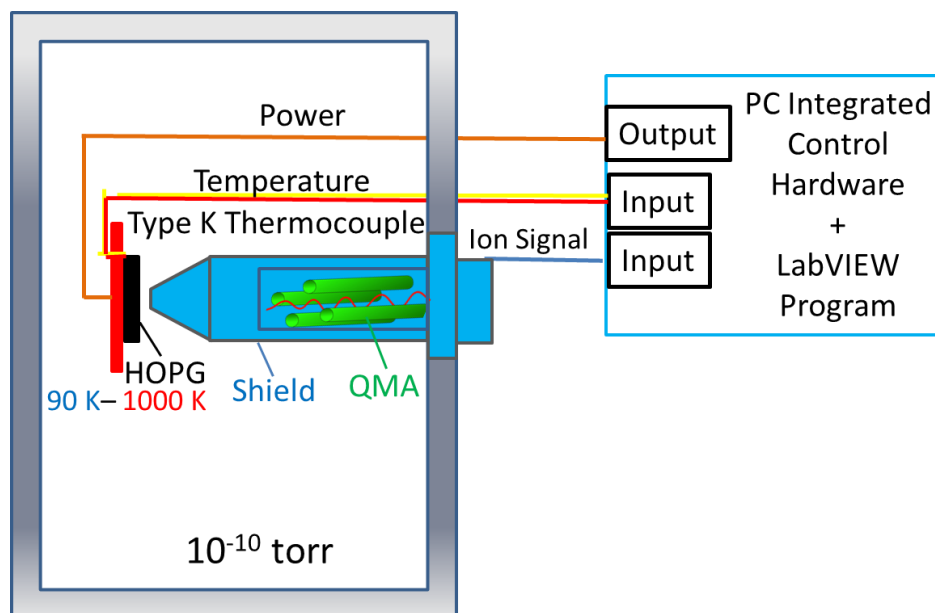


**Figure 2.5.** Control setup of temperature programmed desorption/temperature programmed reaction spectroscopy (TPD/TPRS).

The temperature programmed reaction spectroscopy (TPRS) is an interesting twist to TPD. In cases where reactive species are present on the surface, thermal excitation from the temperature ramp leads to chemical reactions on the surface. Gaseous products from the chemical reactions will get detected by the QMA. Multiple species could be monitored simultaneously by TPRS. In my TPRS instrument setup, up to 10 different  $m/z$  species could be monitored concurrently.

The TPD/TPRS spectra provide both qualitative and quantitative information, as illustrated with the TPD of pentane desorption from graphite C(0001). (Figure 2.6) The TPD spectrum plots the molecular desorption rate as a function of temperature. Two peaks are in the TPD spectrum: one peaked at 118 K, and one peaked at 143 K. This temperature difference indicates different activation energy for desorption, i.e. different desorption energy (or adsorption energy based on the principle of



microscopic reversibility). The binding strength of the lower temperature peak is obviously weaker than that of the high temperature peak. The 118 K peak is assigned to the desorption of pentane from the multilayer, and the 143 K peak is the desorption of pentane monolayer from the graphite C(0001) surface.<sup>32</sup> In a TPRS spectrum, the desorption temperature profile of the evolved gas specie peaks reflects activation energy of the surface reactions.

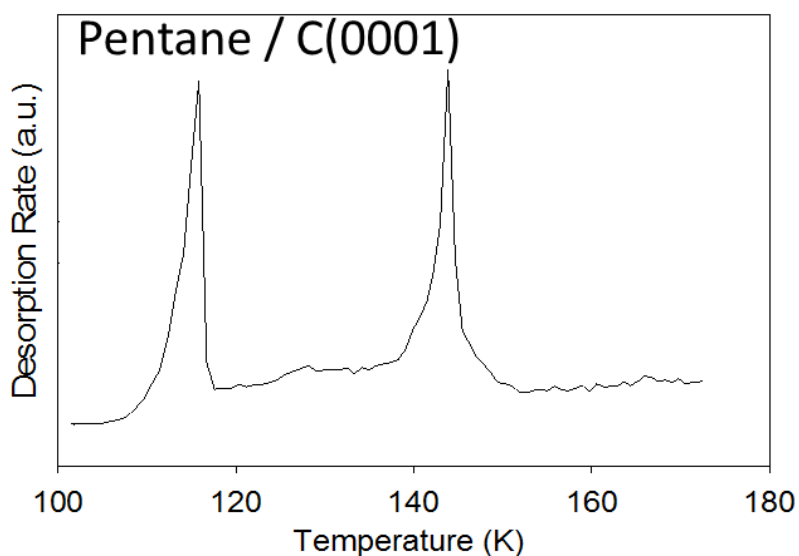


**Figure 2.6.** TPD of Pentane from C (0001), monitored at  $m/z = 43$  and a ramp rate of 1 K/s.

The quantitative analysis of TPD spectra proposed by P.A. Redhead<sup>33</sup> follows classical chemical kinetic theory. The measured ion signal is proportional to the desorption rate of the adsorbates:

$$I \propto -\frac{d\theta}{dt} = k\theta^n, \quad \text{Eq. (2.1)}$$

where  $I$  is the mass ion signal,  $\theta$  is the coverage,  $k$  is the desorption rate constant, and  $n$  is the order of the desorption process. In TPD/TPRS measurements, the temperature is a linear ramp, therefore:

$$T = T_0 + \beta t, \quad \text{Eq. (2.2)}$$

$$dT = \beta dt, \quad \text{Eq. (2.3)}$$

where  $\beta$  is the linear heating rate,  $T$  is temperature, and  $T_0$  is the initial temperature.

Substituting Eq. (2.3) into Eq. (2.1) yields:

$$-\frac{d\theta}{dT} = \frac{1}{\beta} k \theta^n. \quad \text{Eq. (2.4)}$$

The rate constant  $k$  is represented by the Arrhenius equation,

$$-\frac{d\theta}{dT} = \frac{1}{\beta} \nu \cdot \exp\left(-\frac{E_{ad}}{RT}\right) \theta^n, \quad \text{Eq. (2.5)}$$

where  $\nu$  is the pre-exponential factor,  $E_{ad}$  is the adsorption energy, and  $R$  is the universal gas constant. In this thesis, the TPD/TPRS experimental data are simulated by Eq. (2.5) to extract the pre-exponential factor  $\nu$ , the adsorption energy  $E_{ad}$ , and desorption order  $n$ . The MATLAB code for the TPD/TPRS kinetics simulation, utilizing the Runge-Kutta numerical integration method, is provided in Appendix B.

### 2.3.3 Scanning Tunneling Microscopy (STM)

Lithium ethylene dicarbonate (LEDC) is a key component in the early-stage solid electrolyte interphase (SEI) formation. The unique properties of LEDC—electron insulating, Li-ion conducting, and the capacity to stabilize SEI formation—make it the subject of extensive experimental and theoretical studies.<sup>29</sup> Yet basic structural information of LEDC (both in bulk and in the thin-film form) is not well-established. The purpose of creating Model System II (LEDC-DMF/Ag(111) model system) is to

study the structure of the LEDC film and gain insight on its structure-property relations. Dimethylformamide (DMF) is a polar solvent for LEDC, and was used to deposit LEDC using the aerosol liquid deposition method. The inclusion of DMF in the model system also allows the opportunity to investigate the interaction between LEDC and the polar solvent. STM is the surface structure imaging tool chosen to characterize Model System II, for its molecular/atomic resolution capability. Invented by Binnig and Rohrer in 1982 at the IBM Research Center in Zürich<sup>34</sup>, STM utilizes the quantum tunneling effect to image molecules and atoms. A STM system is composed of a sharp and conductive metal tip, a conductive sample and a computer-controlled feedback system to control the distance between the sample and the tip. (Figure 2.7) When operating, a bias voltage is applied between the sample and the tip, and the feedback control system brings the tip to within angstroms of the sample surface where the tunneling current begins to flow.

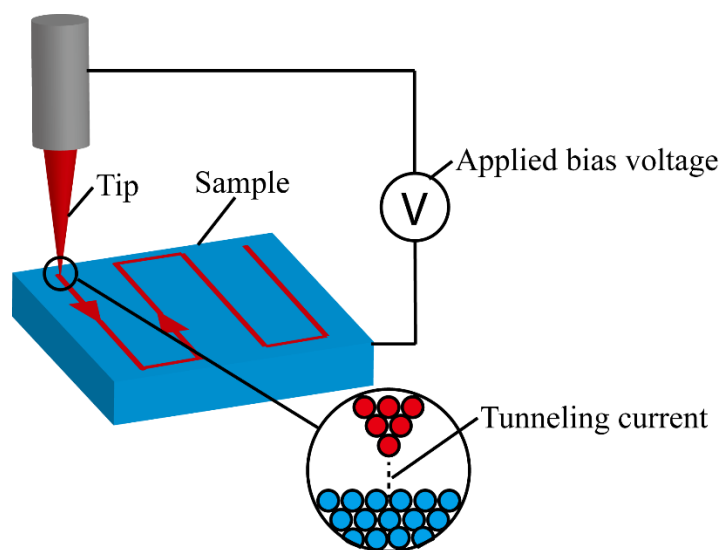


**Figure 2.7.** Schematic illustration of scanning tunneling microscope, showing the raster scanning of the STM tip (upper left) and tunneling junction (lower right).

Different models have been proposed to describe the tunneling process in STM. The simplest and most widely used model is an electron tunneling through a rectangular potential barrier. The tunneling current has an exponential relations with the potential barrier width<sup>35</sup>:

$$I \propto V \exp(-A\sqrt{\phi d}), \quad \text{Eq. (2.6)}$$

where V is the bias voltage, A is a coefficient close to unity ( $1.02 \text{ \AA}/(\text{eV})^{1/2}$ ), d is the potential barrier width, and  $\phi$  is the potential barrier height. Based on this model, if the tunneling current is held constant (the “constant current” mode of STM imaging), the vertical position recorded by STM will be the topography of the surface under scanning.

The real situation is much more complicated and the 1D potential barrier model does not suffice to interpret STM images for all material surfaces. More refined models have been proposed to handle materials with different electrolyte properties. One of the most important models is the s-wave tip model developed by J. Tersoff and D.R. Hamann.<sup>36</sup> This model presumes that the geometry of the tip apex is a symmetric metal sphere and only the s states of the metal tip participate the tunneling process. In this case, the tunneling current at the center of the sphere with radius  $r_0$  is proportional to the local density of states (LDOS) under low bias voltage, expressed as:

$$I \propto eV \rho_s(E_F) \rho_t(E_F, r_0) \exp \left[ -\frac{2d}{\hbar} \sqrt{m \frac{(\phi_s + \phi_t)}{2}} \right], \quad \text{Eq. (2.7)}$$

where I is the tunneling current, e is the charge of an electron, V is the bias voltage,  $\rho_s(E_F)$  is the LDOS of the sample at the Fermi level,  $\rho_t(E_F, r_0)$  is the LDOS of the

center of the sphere tip apex at the Fermi level,  $d$  is the tip-sample separation distance,  $\hbar$  is the reduced Planck constant,  $m$  is the electron mass, and  $\phi_s$  and  $\phi_t$  are the workfunctions of the sample and the tip, respectively.

The STM used in these studies is an Omicron STM-1 room temperature system. The measurement procedure is as follows: after the microaerosol liquid deposition was performed in the loadlock, the sample was immediately transferred into the STM analysis compartment of the main chamber. All UHV-STM images were taken at room temperature with constant current mode (current setpoint: 0.15-0.20 nA) and electropolished tungsten tips. The gap voltage was set as 1.000 V, with tip grounded and sample biased.

## Chapter 3 Adsorption and Reaction Branching of Molecular Carbonates on Lithiated C(0001) Substrates

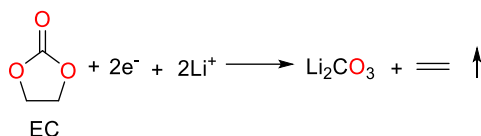
This chapter has been published as Song, W.; Bharath, S.; Reutt-Robey, J. *The Journal of Physical Chemistry C* 2014, 118, 19017. I performed all TPD measurement and data analysis. Satyaveda Bharath assisted in the initial preparation and Auger electron spectroscopy measurement of the Li-C(0001) substrates. The MATLAB code for TPD simulation was provided by Dr. Andrew Gellman and subsequently modified by me for this specific system.

### 3.1 Introduction

The Li-ion rechargeable battery (LIB) is the energy storage device that powers a variety of modern inventions, ranging from smart phones to electrical vehicles. Despite these successes, further applications are hindered by the limited energy density, capacity decay after charge-discharge cycles and safety.<sup>7,14</sup> One key contributing factor to capacity decay and safety is the electrochemically-driven reactions that occur at the graphite anode-electrolyte interface.<sup>37</sup> During initial charging, the decomposition of the ethylene carbonate (EC) based electrolytes leads to the formation of a passivating layer on the anode known as the solid-electrolyte interphase (SEI).<sup>38,39,40</sup> The formation and dissolution of SEI consumes  $\text{Li}^+$  and causes capacity loss to LIB. Extensive research has been devoted to the study of the SEI formation and its major composition is established.<sup>28,41</sup> Already, refinements in electrolyte formulation have led to interphases with improved stability and cycling

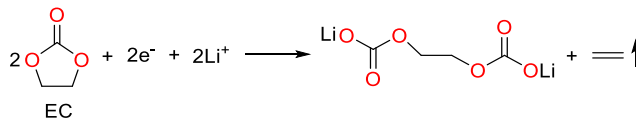
performance.<sup>21,42</sup> Mechanistic aspects of SEI formation, however, are not fully understood and further investigation is needed to guide improvements in electrolyte formulation.

The components of the SEI have been identified as a complex mixture of lithium salts<sup>43,29,44</sup> and oligomers<sup>45,46,47</sup> to polymers<sup>48,49</sup> with composition depending on SEI thickness and battery cycling. Lithium carbonate ( $\text{Li}_2\text{CO}_3$ ) is an important inorganic product that can be formed by direct two-electron reduction (Scheme 3.1).



**Scheme 3.1.** 2e- EC reduction pathway to  $\text{Li}_2\text{CO}_3$ .

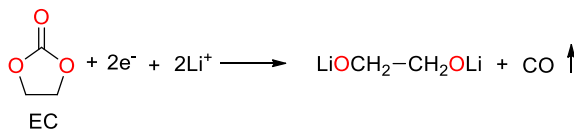
Another important early-stage SEI component is lithium ethylene dicarbonate (( $\text{LiOCOCCH}_2$ )<sub>2</sub> or LEDC).<sup>29</sup> Different pathways are proposed to account for the formation of LEDC. One widely cited reaction pathway to form LEDC is the single electron reduction of EC (Scheme 3.2)<sup>28</sup>.



**Scheme 3.2.** 1e<sup>-</sup> electron reduction of EC to form LEDC.

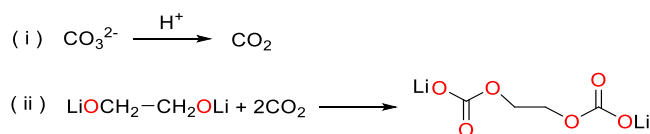
Anionic polymerization has been proposed as an alternative pathway to form LEDC during SEI growth.<sup>45</sup> In this mechanism, the LEDC is contained within polyethylene oxide (PEO)-based oligomers. At the initial stage of SEI formation,

however, *ab initio* molecular dynamics (AIMD) simulations predict that close contact between the EC molecules and the electron-rich anode generates LEDC via a lithium ethylene glycolate (LEG) intermediate (Schemes 3.3).<sup>19</sup>



**Scheme 3.3.** 2e- EC reduction pathway to form LEG.

At the electrode surface, LEG evolves to LEDC in the presence of CO<sub>2</sub> (Scheme 3.4).



**Scheme 3.4.** LEG pathway to form LEDC

In the present work, we focus on the very initial stage of SEI formation, revealing interactions between molecular carbonate electrolytes and lithium-modified graphite (C(0001)) prepared *in situ*. Temperature programmed desorption is used to quantify molecular electrolyte adsorption energies (nonreactive) on the graphite substrates. Temperature programmed reaction spectroscopy (TPRS) is then used to track EC reduction products, through the gases released upon thermal decomposition. We show that metallic lithium drives complete EC decomposition and perform a detailed mass balance analysis to quantify product branching. This provides important information on the distribution of lithium salts that form at the very onset of SEI formation.



### 3.2. Experimental Section

All experiments were conducted in an ultrahigh vacuum (UHV) apparatus with a base pressure of  $3 \times 10^{-10}$  torr, rapid-entry sample loadlock, facilities for *in-situ* sample processing and Auger electron spectroscopy (AES), temperature programmed desorption (TPD) and temperature programmed reaction spectroscopy (TPRS). Highly oriented pyrolytical graphite (HOPG) (Grade A, Micromash) was freshly cleaved, fixed on a stainless steel sample plate and transferred to the UHV sample manipulator. The sample was first annealed at 1000 K for 5h to create a clean C(0001) substrate.<sup>20</sup> A well-degassed SAES getter was used as the Li source. Three different model anode substrates were created: (i) clean C(0001), (ii) C(0001) with a submonolayer of ionic lithium, prepared by deposition of  $> 1$  monolayers of Li, held at 300 K to facilitate intercalation, (iii) a 5-monolayer film of Li(s) on C(0001), prepared by deposition on a 110 K substrate. Lithium exposure was calibrated by peak-to-peak amplitude in AES measurements.

Mixtures of EC and linear carbonates are used in LIB's to maintain liquid electrolytes over operational temperatures. In this research, dimethyl carbonate (DMC) is selected as a representative in linear carbonates group. Electrolytes ethylene carbonate (EC) (Sigma-Aldrich, anhydrous, 99%) and dimethyl carbonate (DMC) (Sigma-Aldrich, anhydrous,  $\geq 99\%$ ) were transferred into separate glass vials and degassed with multiple freeze-pump-thaw cycles prior to introduction to the sample through a UHV leak valve. Ethylene (Matheson, 99.9%) and ethylene oxide (Praxair, 99.9%) gases are used as mass spectrometry calibration standards to determine their sensitivity factors for product quantitation. Clean and lithiated C

(0001) surfaces were cooled to 100 K and dosed line-of-site with either DMC or EC. The dosing pressure is on the order of  $1 \times 10^{-8}$  torr), as measured by an ionization gauge calibrated for nitrogen and the exposures are given in units of Langmuirs ( $1 \text{ L} = 1 \times 10^{-6} \text{ torr}\cdot\text{s}$ , where  $1 \text{ L} \approx 1 \text{ monolayer}$ ).

A newly constructed temperature programmed desorption (TPD)/ reaction spectroscopy (TPRS) system was utilized for precise measurements of the surface binding energies/reactivities of molecular electrolytes. For these measurements, the sample faced the entrance of a quadruple mass analyzer (Pfeiffer Vacuum QME 200) mounted in a shroud. The 1 mm aperture at the conical entrance to the shroud was reproducibly positioned 3 mm from the sample. A type-K thermocouple was used to monitor the temperature (100 K – 1200 K range). A LabVIEW program was used for PID-temperature controlling, to achieve a linear temperature ramp rate (here 0.5 K/s – 2 K/s) while simultaneously collecting ion signals. The system supports temperature programmed reaction spectroscopy (TPRS) since up to 12 masses could be monitored simultaneously. Absolute sample temperatures were determined by obtaining TPD data for alkane calibrants ( $\text{C}_5\text{-C}_{10}$ ) on HOPG and comparing to literature desorption data. All temperatures are reported with an error of  $\pm 1 \text{ K}$ .

For the present study, TPRS provides for direct quantitation of those EC reduction products that release gases upon thermal decomposition. Product identification is based upon reported pathways for EC reactions. The inorganic reduction product, lithium carbonate is not measured directly by TPRS, but is readily quantified through application of detailed mass balance of calibrated exposures of ethylene carbonate.

### 3.3 Results and discussions

#### 3.3.1. Clean Graphite

We first determine the binding energies of molecular carbonates on C(0001). Coverage-dependent TPD spectra of EC and DMC from C(0001) (heating rate of 1 K/s) are presented in Figure 3.1 and 3.2. Both electrolyte molecules desorb without decomposition. Desorbing EC and DMC were monitored respectively through the  $m/q = 43$  and  $m/q = 45$  ion signal, the major cracking products of the parent ions with minimal overlap with residual chamber gases.

The coverage of TPD spectra of EC from pristine graphite were varied from 0.20 L to 3.0 L (Figure 3.1). Only one peak is observed and that peak does not saturate with increasing coverage. Such TPD spectra are indicative of zero-order desorption kinetics, where the desorption rate is independent of coverage,  $\theta$ , and depends only on the rate constant  $k$ . Zero-order kinetics indicates the formation of three dimensional islands of EC, revealing that EC dewets C(0001). This indicates EC-EC interactions are stronger than EC-C(0001) interaction. Evidently, dipole-dipole interactions between EC molecules (molecular dipole moment of 4.9D) dominate the weaker EC-C(0001) interactions. By plotting the leading edge of the TPD spectra in Arrhenius representation (shown in the inset of Figure 3.1), the EC desorption energy,  $E_d$ , is determined to be  $0.60 \pm 0.06$  eV, within experimental error of the EC vaporization enthalpy (0.65 eV) measured by the transpiration method at 298.15 K.<sup>21</sup>

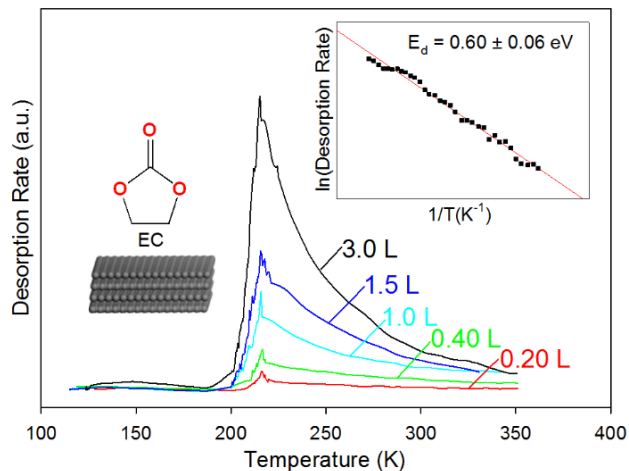


**Figure 3.1.** TPD spectra of EC desorption from C(0001). Inset shows the Arrhenius representation of the leading edge of the spectra, whose slope yields an adsorption energy of  $E_d = 0.60 \pm 0.06$  eV. Spectra were collected by monitoring  $m/q = 43$  at the heating rate of 1 K/s. For clarity, high frequency noise is removed by a low pass filter.

As a contrast to EC, the TPD spectra of DMC have three distinct peaks. (Figure 3.2) At low coverage (0.20 L), one peak appears at  $T = 180$  K. As the coverage increases to 0.50 L, a 2nd peak begins to appear at  $T = 160$  K and both peaks grow with increasing coverage. At even higher coverages (3.0 L and 4.0 L), a third peak is observed and the first two peaks gradually reach saturation. The third peak continues to grow with further increasing coverage. These three features represent monolayer, bilayer and multilayer of DMC desorption from C(0001). Distinct layer-dependent desorption features indicate that DMC wets the graphite surface and adopts a Volmer-Weber film growth mechanism. This indicates the DMC-surface interaction dominates the DMC-DMC interaction, and is consistent with the much weaker dipole moment of DMC (just 0.91 D for DMC vs. 4.9 D for EC). The monolayer desorption rate  $r$  is described by first-order desorption kinetics, expressed as

$$r = -\frac{d\theta}{dt} = k\theta = v \cdot \exp\left(-\frac{E_d(1-\alpha\theta)}{RT}\right)\theta, \quad \text{Eq. (3.1)}$$

where  $v$  is the desorption frequency factor,  $\alpha$  is a parameter to describe the intermolecular interactions,  $R$  is the universal gas constant and  $T$  is temperature. The observed monolayer TPD feature were simulated with Eq. (3.1) (shown in the Figure 3.2 inset). The desorption frequency factor  $v$  is estimated by the Campbell-Sellers relation<sup>22</sup> to be  $10^{17.6} \text{ s}^{-1}$  from the gas phase entropy of a structurally similar molecule<sup>23</sup> and  $E_d$  and  $\alpha$  were treated as adjustable parameters. The simulation yielded  $\alpha = -0.015 \text{ monolayer}^{-1}$  (consistent with weakly attractive interactions) and  $E_d = 0.64 \pm 0.05 \text{ eV}$ . The value of  $E_d$  is significantly higher than the DMC vaporization enthalpy of  $0.39 \text{ eV}$ , consistent with the wetting of molecules on C(0001).

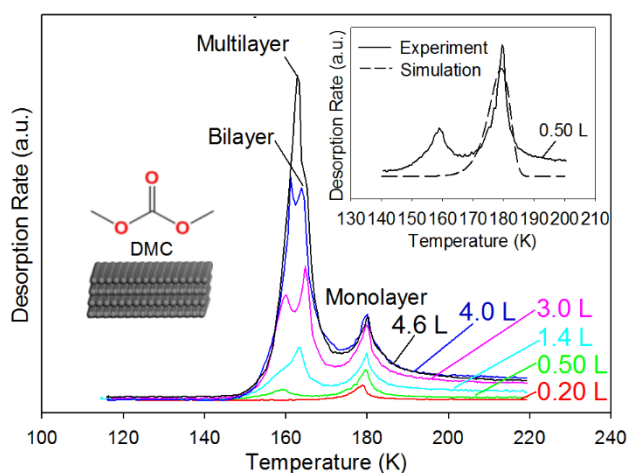


**Figure 3.2.** TPD spectra of DMC desorption from C(0001). Inset shows the simulation of DMC monolayer desorption via first-order desorption kinetics with an adsorption energy value adjusted of  $0.64 \pm 0.05 \text{ eV}$ . Spectra were collected by monitoring  $m/q = 45$  at the heating rate of  $1 \text{ K/s}$ .

### 3.3.2. Lithiated Graphite

We next investigated molecular carbonate interaction with lithiated C(0001) in a regime where lithium atoms ionize and the majority intercalate into the interlayer positions of graphite, leaving a sub-monolayer of surface lithium ions. Lithium ionization is confirmed by the appearance of a 42 eV Auger feature, also found in ionic lithium compounds such as LiF.<sup>24</sup> (The actual charge on the surface Li ions has been calculated as +0.8.<sup>25</sup>) EC and DMC were then separately deposited on the Li<sup>+</sup>/C(0001) surface at 100 K. The TPD spectra of EC and DMC on the lithiated surface are plotted in Figure 3.3 and 3.4.

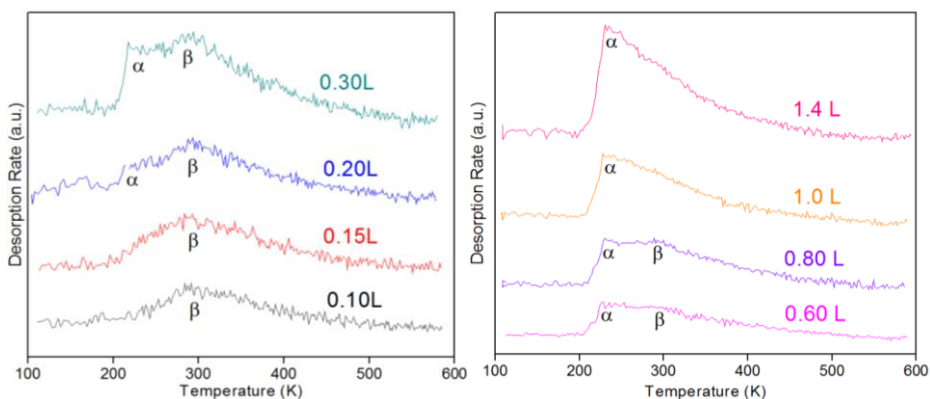


**Figure 3.3.** TPD spectra of EC on lithiated C(0001) 0.10 L – 0.30 L (left panel) and 0.60 L – 1.4 L (right panel), collected by monitoring  $m/q = 43$  at the heating rate of 1 K/s.

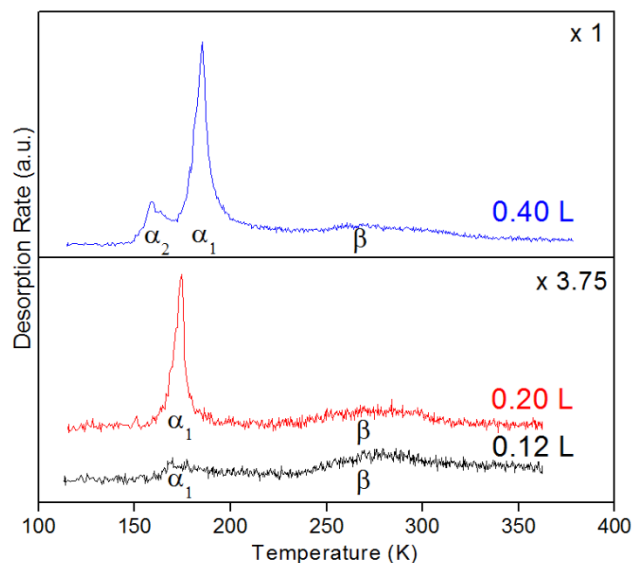


**Figure 3.4.** TPD spectra of DMC on lithiated C(0001) 0.12 L – 0.40 L, collected by monitoring  $m/q = 45$  at the heating rate of 1 K/s.

The EC desorption products from the lithiated surface are identical to those from clean C(0001), indicating that EC does not dissociate on lithiated graphite. At low EC coverages (0.10 L and 0.15 L), a very broad peak (peak  $\beta$ ) is centered at  $T = 285$  K. As the coverage increases to 0.20 L, a second peak ( $\alpha$ ) appears at  $T = 210$  K. In the higher coverage range (0.60 L – 1.4 L), peak  $\alpha$  outgrows peak  $\beta$  and finally overshadows it. The  $\beta$  feature is a new desorption state due to surface lithium ions. The substantial (more than 200K) width of this feature indicates a range of EC adsorption energies. The increased desorption temperature and substantial width of the  $\beta$  feature are attributed to EC interactions with surface  $\text{Li}^+$ . Dipolar EC molecules will surround  $\text{Li}^+$  and form solvation structures of the form  $\text{Li}^+(\text{EC})_n^-$ . As EC coverage increases, the  $\text{Li}^+$  charge eventually becomes fully shielded and EC resumes zero-order desorption kinetics, resulting in the appearance of the  $\alpha$  peak. The desorption energy of EC from the  $\text{Li}^+$  is thus not a constant value, but changes with

coverage (the closer EC to  $\text{Li}^+$  and lower  $n$ , the stronger the interaction energy). The desorption energy for the solvating EC ( $\beta$  feature) is found to range from 80 kJ/mol (0.83 eV) – 150 kJ/mol (1.55 eV) by assuming first order desorption kinetics (Figure 3.5). Bhatt *et al.* have performed gas phase DFT calculations on the average bonding energy between  $\text{Li}^+$  and EC in  $\text{Li}^+(\text{EC})_n$  complexes.<sup>26</sup> When the EC coordination number goes from  $n = 3$  to  $n = 1$ , their calculations determine an average bonding energy increase from 0.935 eV to 2.23 eV, comparable to the measured range of EC desorption energies on the lithiated substrate. The results reveal that EC interacts with  $\text{Li}^+$  at the C(0001) surface to form “half-solvation” shell-like structures. The range of experimental values is slightly lower than the range of calculated values, due to the partial charge (0.8e) of  $\text{Li}^+$  on the C(0001). The TPD spectra of DMC on lithiated graphite have a similarly broad  $\beta$  peak, but the intensity is reduced by DMC’s propensity for Volmer-Weber growth, consistent with the lower solvation shell forming ability of DMC vs. cyclic carbonates.<sup>27</sup>

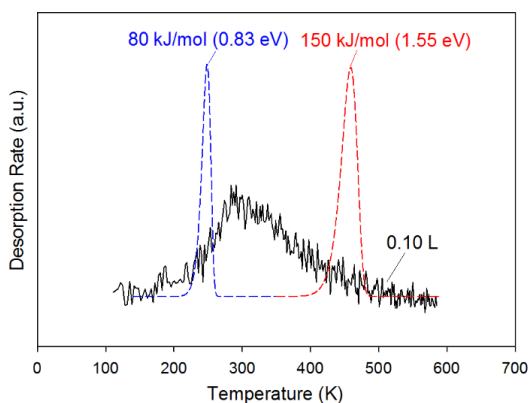


**Figure 3.5.** TPD spectrum of EC on  $\text{Li}^+/\text{C}(0001)$  (black), and simulations of the 1st order desorption energy profiles at the lower (blue) and upper (red) bounds of the experimental spectrum.



### 3.3.3 Impact of Metallic Lithium

The low workfunction of metallic lithium ( $2.49 \pm 0.02$  eV)<sup>28</sup> supports spontaneous electron transfer to molecular carbonates, driving carbonate decomposition. To study reactions that represent the very initial stage of SEI formation, metallic lithium films were deposited on C(0001) substrates held at 100 K. Low temperature suppressed the intercalation of lithium and an AES signature at 50 eV confirmed the formation of metallic lithium on the C(0001) surface.<sup>24</sup> The amount of the deposited lithium was determined to be ~5 monolayers. EC (0.20 L and 0.40 L) was subsequently deposited on Li<sub>(metal)</sub>/C(0001) and the mass range  $m/z = 1$  to 100 was first swept with TPRS to identify released gases. Complete EC decomposition in this submonolayer regime was verified by the absence of the parent molecular ion ( $m/z = 88$ ).

Four distinct gases were released during TPRS of the deposited EC: C<sub>2</sub>H<sub>4</sub>, C<sub>2</sub>H<sub>4</sub>O and CO<sub>2</sub> as shown in Figure 3.6, and much smaller amounts of organic ethylene glycols (Appendix C, Figure C1 and C2). The broad C<sub>2</sub>H<sub>4</sub> and CO<sub>2</sub> TPRS peaks with the 450 K onset and 570 K maxima, result from the thermal decomposition of LEDC. This assignment is based upon the reported release of C<sub>2</sub>H<sub>4</sub> and CO<sub>2</sub> at comparable temperature onset in the decomposition of bulk LEDC.<sup>44</sup> The C<sub>2</sub>H<sub>4</sub> and C<sub>2</sub>H<sub>4</sub>O peaks with 600 K maxima, are assigned to the thermal decomposition of LEG. This agrees with the higher decomposition temperature reported for LEG.<sup>13</sup> The present TPRS results indicate that LEG decomposes preferentially to C<sub>2</sub>H<sub>4</sub> (75.%) over C<sub>2</sub>H<sub>4</sub>O (25.%). This is consistent with theoretical predictions, which show a large energy barrier for C<sub>2</sub>H<sub>4</sub>O formation at the lithium metal interface.<sup>29</sup>

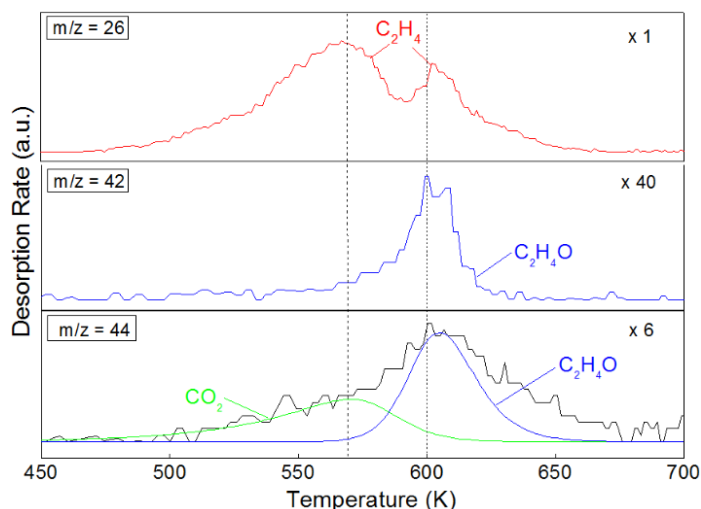


**Figure 3.6.** Temperature programmed reaction spectra (TPRS) of EC reduction products. Upper trace is  $C_2H_4$  (daughter ion  $m/z = 26$ ); middle trace is  $C_2H_4O$  (daughter ion  $m/z = 42$ ); lower trace ( $m/z = 44$ ) shows desorption peaks from both  $CO_2$  (570 K maximum) and  $C_2H_4$  (600 K maximum) and a corresponding fit to asymmetric logistical functional forms to quantify the  $CO_2$  (green curve) and  $C_2H_4O$  (blue curve) products.

In this monolayer regime, where EC interacts directly with metallic lithium, LEDC and LEG are the dominant organolithium reduction products observed. (Organic ethylene glycols account for 1.1% of the total EC reduction, Appendix C)

We next determine the chemical amount of each of the LEDC and LEG products that result from the reductive decomposition of EC doses of 0.40 L. For this quantitative analysis, the nitrogen equivalent coverage unit is converted to absolute coverage unit by relative ionization gauge gas correction factors, e.g. 0.40 L EC in nitrogen equivalent unit is 1.5 L in absolute coverage unit. (Appendix C, Figure C5) As

described more fully in the Appendix C, LEDC coverage can be directly determined from the area of the C<sub>2</sub>H<sub>4</sub> TPRS peak centered at 570 K via Eq (3.2).

$$\theta_{\text{abs}} = r \cdot g \cdot s \cdot A, \quad \text{Eq. (3.2)}$$

where  $\theta_{\text{abs}}$  is the absolute coverage,  $r$  is the relative ionization gauge gas correction factor,  $g$  the geometric scaling factor,  $s$  the gas sensitivity factor and  $A$  the area of the TPRS peak. The LEG coverage is similarly determined from the areas of the C<sub>2</sub>H<sub>4</sub> and C<sub>2</sub>H<sub>4</sub>O TPRS peaks centered at 600 K.

Based on this analysis, reduction of 1.5 L of ethylene carbonate results in the formation of  $0.64 \pm 0.12$  L of LEDC and  $0.40 \pm 0.05$  L of LEG, due to the absence of desorbing EC. The sum of the LEDC and LEG products- $1.04 \pm 0.17$  L accounts for 70.% of the EC dose. We know that EC undergoes complete decomposition due to the absence of the parent ion ( $m/z = 88$ ) in the TPRS sweeps. The remainder 30% of the EC decomposition products are thus determined, by the principle of mass balance, to result in the formation of the nondecomposing inorganic product Li<sub>2</sub>CO<sub>3</sub> (Scheme 3.1). Following the TPRS measurement, the surface thus contains the Li<sub>2</sub>CO<sub>3</sub> salt (Table 3.1), as well as the lithium oxide formed upon LEG decomposition. This mixture of inorganic lithium salts was further sensed by Auger electron spectroscopy through the growth of oxygen KLL (503 eV) signal.

**Table 3.1.** EC Decomposition Products on Li(metal)/C(0001) and Their Branching Ratios Based upon 1.5 L EC (in Absolute Coverage Units)

EC decomposition final product	LEDC	LEG	Li <sub>2</sub> CO <sub>3</sub>
absolute coverage (ML*)	0.64 ± 0.12	0.40 ± 0.05	0.5 ± 0.2
reaction percentage	43.%	27.%	30%

\*This assumes 1 L  $\equiv$  1 monolayer.

In the monolayer regime, we have shown the significant branching of organolithium salts in the reduction of EC. According to this detailed mass analysis, 70.% of the EC converts to two organolithium salts, LEDC and LEG. A much smaller amount (1.1%) of EC converts to non-specified organic ethylene glycols, characterized by lower desorption temperature. The remaining EC (30%) forms Li<sub>2</sub>CO<sub>3</sub>. This quantitative information on product distribution at well-defined interfaces, provides a necessary benchmark to model EC reduction. Knowledge of initial product distribution will assist efforts to create stable SEI films with desirable properties.

### 3.4 Summary

Molecular carbonates interact weakly with graphite C(0001) surfaces. EC exhibits zero-order desorption, indicating dewetting and clustering on the clean graphite surface and the adsorption energy is measured to be  $0.60 \pm 0.06$  eV. DMC, with its weaker intermolecular interactions, adopts a Volmer-Weber film growth mechanism and the monolayer adsorption energy is determined to be  $0.64 \pm 0.05$  eV. When the C(0001) system is lithiated to a submetallic extent, both EC and DMC remain intact, but exhibit a new desorption feature. The position and width of this new feature

indicates a substantially increased EC desorption energy that varies from 0.83 eV – 1.55 eV. This range of values is consistent with the formation of a "half" solvation shell ( $\text{Li}^+(\text{EC})_n^-$  and  $\text{Li}^+(\text{DMC})_n^-$ ). EC undergoes complete decomposition on Li metal films on C(0001), and the lithium ethylene glycol and lithium ethylene dicarbonate products are quantified through the corresponding ethylene and ethylene oxide TPRS desorption products. A 1.5 L EC film (absolute coverage units) decomposes into  $0.64 \pm 0.12$  L of LEDC (43.%),  $0.40 \pm 0.05$  L of LEG (27.%) and (by mass balance)  $0.5 \pm 0.2$  L of  $\text{Li}_2\text{CO}_3$  (30%). The present study models the initial-stage electrolyte–anode interactions in electrochemical cells, revealing the binding strengths of molecular electrolytes with graphite and lithiated graphite, as well as the reaction branching in EC reduction. In an electrochemical environment, branching ratios should depend additionally on the driving potential and the length scale for charge transfer (film thickness).

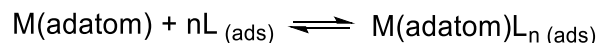
## Chapter 4 Complexation and Phase Evolution at Dimethylformamide-Ag(111) Interfaces

Chapter 4 research is a collaboration between myself, Qian Shao, Kevin Leung and Karen Gaskell. This work will be submitted for journal publication.

All depositions and scanning tunneling microscopy (STM) measurements were performed by me and Qian Shao. Kevin Leung performed density functional theory (DFT) calculations and Karen Gaskell performed X-ray photoelectron spectroscopy (XPS) measurement. I analyzed the experiment results, wrote the manuscript and prepared all figures.

### 4.1 Introduction

Molecular organization in thin films on metal surfaces has attracted great attention due to prospective applications in gas sensors, organic electronics and anti-corrosion coatings.<sup>50,51</sup> Among the various molecular building blocks to produce ordered films, surface coordination complexes arise as a distinctive class. In reported systems<sup>52-55</sup>, chemical adsorption has led directly to coordination complex formation, with metal adatoms released from the surface acting as coordination centers and adsorbed molecules as coordinating ligands. In such cases, the coordination bond energy is stronger than the typical van der Waals interactions between molecular adsorbates and metallic substrates<sup>51</sup>. The formation and equilibrium of surface coordination compounds is expressed as (Scheme 4.1):



**Scheme 4.1.** The reaction scheme of surface coordination complex formation,

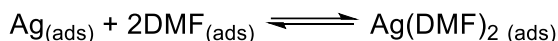
where M is the metal surface adatom, L is the adsorbed ligand and  $ML_n$  is the adsorbed coordination compound. As in their 3D (bulk) metal-organic framework (MOF) counterparts, multi-dentate ligands have been used to construct 2-D metal-organic networks. Metal-organic 2-D network films demonstrate tunable pore size<sup>56,57</sup> and adopt a variety of shapes<sup>58</sup>. Even with emerging application as electrocatalysts<sup>59</sup>, surface coordination complexes remain poorly understood due to complicating interactions with the substrate. Further research on complex formation and structure-property relations is needed to predict functional properties.

Solution-phase coordination complexes have been extensively studied, providing useful concepts for 2-D systems.<sup>60</sup> Surface coordination complexes have distinct properties from their solution counterparts<sup>51</sup> such as: (i) The formal oxidation state of the adsorbed metal coordination center differs from that in the solution phase because the coordination metal atom charge is mediated by the “Fermi sea” of the metallic substrate electrons; (ii) The geometry of the supported coordination compound is distinct, reflecting both the charge state of the coordination metal atom and its anisotropic interaction with the substrate. Additionally, ligand molecules in the coordination compound can interact with the metal surface, impacting the 2-D ordering of surface coordination compounds.

Polar solvent molecules present a particularly important class of ligands to explore. The nitrogen, oxygen, and sulfur atoms found in polar solvents can coordinate to transition metal centers via their lone-pair electrons. The dual role of such heterosolvents as solvent and ligand gives them unique properties. For example, N,N-Dimethylformamide (DMF,  $(CH_3)_2NCHO$ ) has demonstrated the capacity to act

as both solvent and ligand in Fe(II)-catalyzed atom transfer polymerization reactions<sup>61</sup> and in the solvation of the iconic MOF material—MOF-5<sup>62</sup>. In electrical energy storage systems, DMF is often used as the electrolyte<sup>63</sup> and demonstrated good charge-discharge characteristics with sulfolane in initial cycling of the graphite-lithium titanate oxide (Li<sub>4</sub>Ti<sub>5</sub>O<sub>12</sub>) system<sup>64</sup>. Restructuring of the electrode surface, through possible DMF complexation with substrate atoms, would impact electrochemical processes.

In the present work, we investigate interface formation between the polar solvent molecule DMF and the model electrode surface, Ag(111), mapping this active interface with molecular level detail. Controlled deposition of DMF is performed with a pulsed microaerosol molecular deposition source, and the resulting films are monitored by UHV-STM and XPS. Two distinct chemical species, adsorbed DMF and the Ag(DMF)<sub>2</sub> coordination complex, shown below in Scheme 4.2, give rise to three distinct 2-D structural phases. We track interface evolution in the binary films as a function of coverage, combining density functional theory (DFT) (with van der Waals correction) calculations with STM measurements to obtain structural models for all observed phases. We follow with a surface pressure-composition phase diagram to provide physical insight on structure evolution and identify strategies to control surface ordering of coordination complexes. These results expand our knowledge and understanding of Ag coordination chemistry and electrode structure.



**Scheme 4.2.** The formation of Ag(DMF)<sub>2</sub> on Ag(111).



## 4.2 Experimental Section

### 4.2.1 Sample Preparation

A single crystal Ag(111) substrate was prepared by repeated Ar<sup>+</sup> sputtering (1000 eV, 10 mA, 30 min) and annealing (763 K, 5 min) cycles. The Ag(111) was then used for microaerosol molecular beam deposition. DMF deposition was performed in the loadlock compartment (base pressure  $1.2 \times 10^{-9}$  torr) of an ultra-high vacuum chamber, integrated with a pulsed microaerosol molecular beam deposition system as previously described<sup>30</sup>. Briefly, DMF (Sigma Aldrich, 99%, anhydrous) was pumped into the pneumatic nebulizer (Glass Expansion) by a syringe pump and mixed with dry nitrogen carrier gas (22 psi) to generate an aerosol mist. The droplet size of the aerosol mist was reduced to 1-10  $\mu\text{m}$  diameter via a cyclonic spray chamber (Glass Expansion) and then fed into a solenoid-actuated molecular beam valve with a 1 mm orifice (Parker Series 9). Following expansion, the molecular beam passed through two stages of differential pumping before reaching the Ag(111). For long pulse trains (ca. 1000 pulses), pressure in the load-lock compartment reached  $1 \times 10^{-6}$  torr, rapidly decreasing to  $<5 \times 10^{-8}$  torr following the last valve closure. Film growth was performed by successive exposure to 2000 molecular beam pulses. This deposition process is illustrated in Figure 4.1.

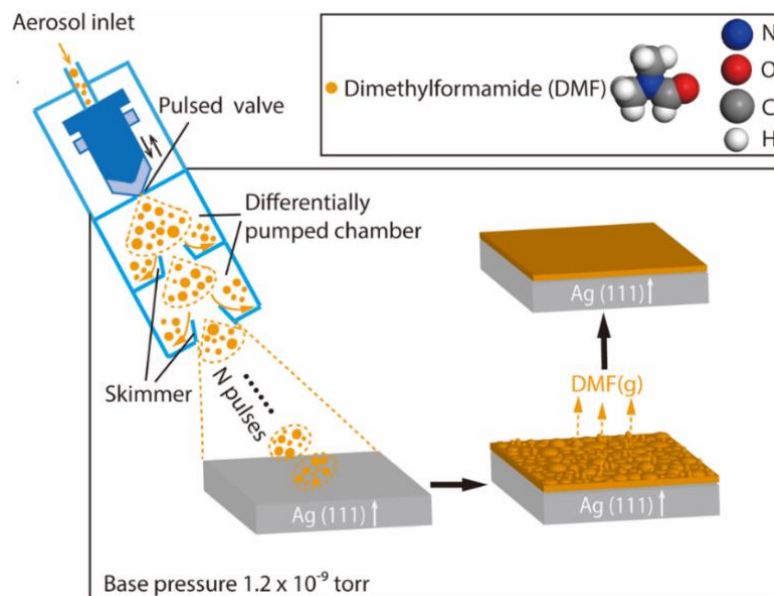


**Figure 4.1.** Experimental schematic of pulsed microaerosol molecular beam deposition of DMF on Ag(111). The molecular structure of DMF is shown in the upper right inset.

#### 4.2.2 STM Measurements

Following each 2000-pulse deposition of DMF, the sample was immediately transferred from the load-lock compartment into the analysis compartment (base pressure  $5 \times 10^{-10}$  torr) for UHV-STM imaging. All UHV-STM measurements were performed at room temperature with electrochemically etched tungsten tips. Typical constant-current imaging parameters used were -1.00 V gap voltage (negative sample bias) and tunnel currents of 0.15 - 0.20 nA. All image analysis was performed using the software Gwyddion<sup>65</sup>. As shown below, a total of 12000 pulses produced a saturating monolayer, in which species were molecularly resolved by STM and a maximum coverage of  $\Gamma = 2.58 \pm 0.02$  DMF (all forms)/nm<sup>2</sup> was determined. Under the simplified assumption that coverage depends linearly upon DMF exposure, each

2000-pulse deposition increased the surface coverage by  $\Gamma = 0.43 \pm 0.01$  DMF (all forms)/nm<sup>2</sup>. This is consistent with STM images acquired at submonolayer coverages.

### 4.2.3 XPS Measurements

X-ray photoelectron spectroscopy (XPS) was performed with a Kratos Axis 165 spectrometer with a monochromatized AlK $\alpha$  source (240 W) operating in hybrid mode. High resolution spectra were taken at pass energy of 20 eV. Following DMF deposition and STM analysis, the sample was extracted from the ultra-high vacuum chamber and rapidly transported under air to the XPS system for characterization (total ambient time < 5 min). XPS measurements were performed at an electron take-off angle of 20° with respect to sample surface to increase surface sensitivity. Data analysis was performed using the CASA XPS software, and the adventitious carbon 1s binding energy peak, set as 284.8 eV, was used for energy scale calibration.

### 4.2.4 Computational Details

DFT calculation was performed using the Vienna *ab initio* Simulation Package (VASP)<sup>66-68</sup>. The Perdew–Burke–Ernzerhof (PBE) functional<sup>69</sup> was used for exchange and correlation. The projector augmented wave (PAW) basis set was utilized with 400 eV cutoff. Van der Waals correction was added using the vdW-DF functional of Langreth and Lundqvist.<sup>70-72</sup>

## 4.3 Results

### 4.3.1 Low Coverages: Formation of 2-D gas (Phase I)

The initial deposition of DMF on the Ag(111) surface (2000 valve pulses, surface coverage  $\Gamma_{\text{DMF(all forms)}} = 0.43 \pm 0.01$  molecules/nm<sup>2</sup>), induces pronounced

changes in the surface morphology. Figure 4.2 shows STM images before and after DMF deposition. Prior to deposition, the Ag(111) terraces are atomically flat and the step edges are smooth. Post deposition, vacancy pits emerge on the terrace, and the step edges are significantly roughened. These morphological changes indicate DMF etching of the Ag(111) surface, suggesting possible complex formation with DMF. Under room-temperature imaging conditions, adsorbates are not imaged directly, but are sensed indirectly as increased tunneling noise. To characterize the DMF-Ag(111) interface and confirm that complexation is the source of Ag(111) etching, XPS measurements were next performed.

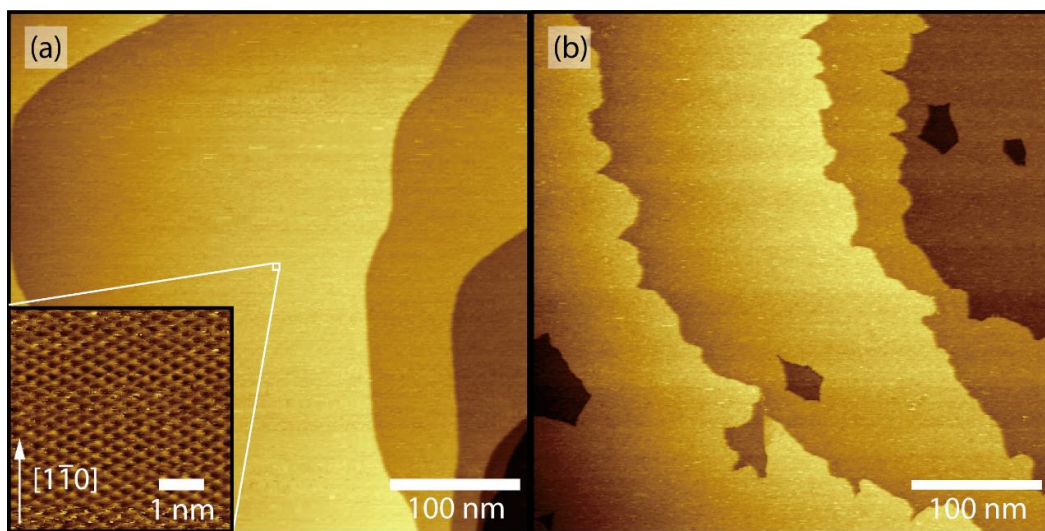


**Figure 4.2.** UHV-STM images ( $400 \text{ nm} \times 400 \text{ nm}$ ) of Ag(111) before (Figure 4.2a) and after (Figure 4.2b) deposition of  $0.43 \pm 0.01 \text{ DMF (all forms)/nm}^2$ , delivered by 2000 pulses of DMF microaerosol entrained in  $\text{N}_2$ .

After STM characterization, the sample was rapidly transferred to another vacuum system for XPS measurements. A surface element survey confirmed that DMF remains on the surface and intract following deposition. The N 1s spectrum

(Figure 4.3a) shows a single peak overlapping with the Ag background feature, indicating a single chemical environment (oxidation state) for the nitrogen atom. The C 1s core (Figure 4.3b) revealed amide carbon (O=CH-N) and amine carbon ((CH<sub>3</sub>)<sub>2</sub>N), as expected for DMF. The atomic concentration ratio of non-adventitious C : N : O is 20.1% : 6.9% : 8.8% ( 2.9 : 1.0 : 1.3), in good agreement with the stoichiometry of the deposited DMF (C<sub>3</sub>H<sub>7</sub>NO).

More insight into the chemical form of DMF is obtained from the O 1s core level spectrum. Figure 4.3c shows three distinct O 1s features: 530.85 eV (50.4%) indicating Ag-O bonding, 531.82 eV (38.2%) indicating carbonyl oxygen, and 533.71 eV (11.4%) indicating adventitious oxygen. The O 1s binding energies for ionic Ag-O have been extensively studied for both AgO and Ag<sub>2</sub>O, for which the O 1s peak appears in the 528.40 eV-529.80 eV window<sup>73,74</sup>. In the present sample, the 530.85 eV peak from Ag-O bond formation is shifted 1.05-2.45 eV above that reported for ionic Ag-O bonds, indicating a largely covalent Ag-O interaction. We thus assign the 530.85 eV feature to an Ag-DMF coordination complex, in which DMF coordinates to Ag adatoms through its carbonyl O atom. The peak at 531.85 eV (nonbonding carbonyl oxygen) is attributed to the presence of additional DMF adsorbed on Ag(111). The relative areas of the O 1s core components indicate that the total DMF ligands coordinated to Ag adatoms are 32% more abundant than adsorbed DMF at this coverage. Annealing the Ag(111) surface at 343 K for 5 min did not significantly change the XPS peaks except for a decrease in adventitious carbon, indicating the relative stability of DMF on Ag(111).

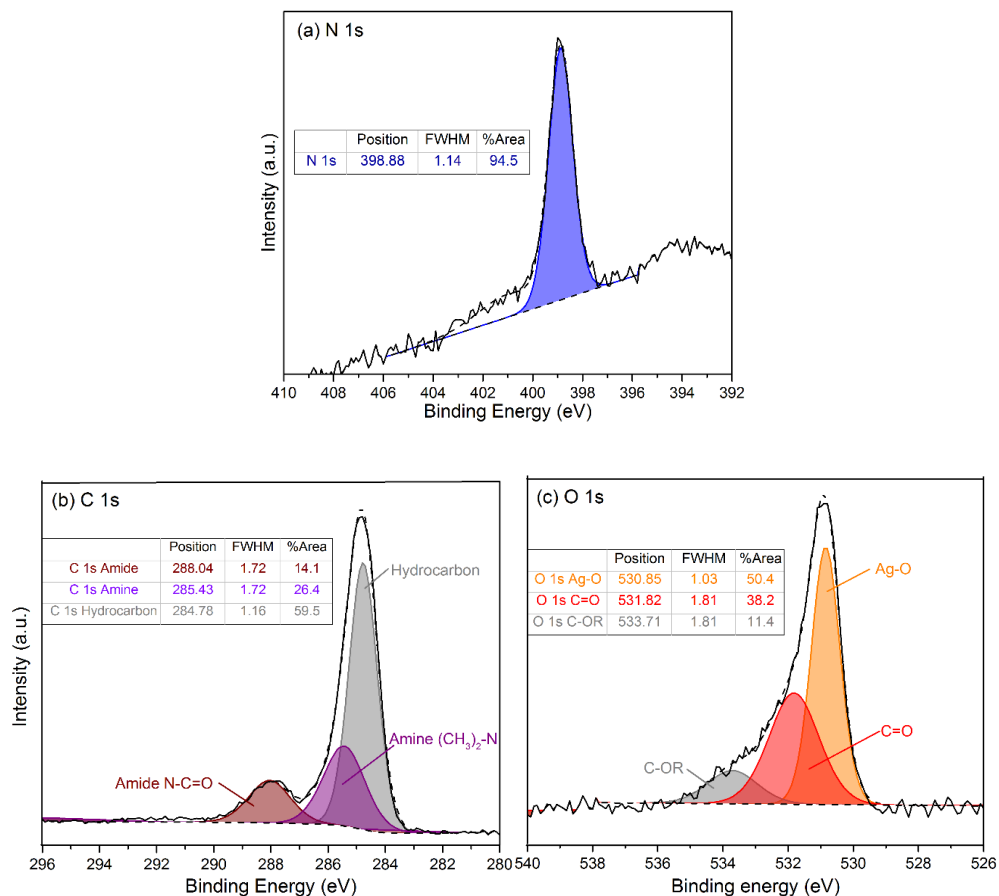


**Figure 4.3.** Core level XPS spectra of (a) N 1s, (b) C 1s, and (c) O 1s, fitted with peaks having a 70% Gaussian and 30% Lorentzian peak shape.

### 4.3.2 Medium Coverages: Island Formation and Growth (Phase II)

Further increases in DMF deposition lead to striking changes in morphology. At a coverage of  $\Gamma_{\text{DMF (all forms)}} = 0.86 \pm 0.01$  molecules/nm<sup>2</sup>, needle-like islands (labelled as Phase II) appear (Figure 4.4a-b). These dark islands grow from the upper step edges and on large terraces with long axes (fast-growth direction) aligned with the substrate  $[1\bar{1}0]$  close-packed direction. The apparent height of the islands is just  $0.06 \pm 0.02$  nm relative to underlying Ag(111), and islands appear dark relative to the

coexisting adlayer phase (Phase I), which has an apparent height of  $0.27 \pm 0.02$  nm relative to the Ag(111) substrate. (Apparent height was determined by height histogram analysis, not shown.) Upon further doubling the coverage to  $\Gamma_{\text{DMF (all forms)}} = 1.72 \pm 0.02$  molecules/nm<sup>2</sup>, the dark islands coarsen predominantly by increasing in width. (Figure 4.4c-d)

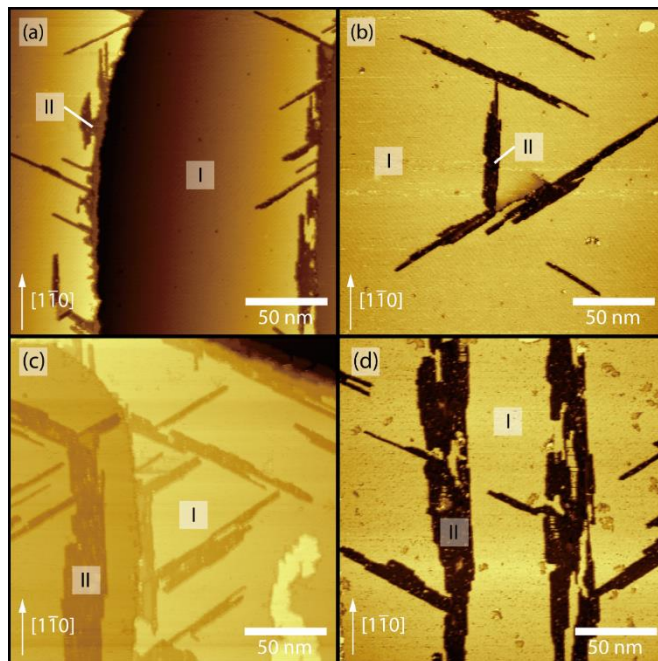


**Figure 4.4.** UHV-STM images ( $200 \text{ nm} \times 200 \text{ nm}$ ) following sequential DMF deposition: (a-b) 4000 pulses to a DMF coverage of  $\Gamma_{\text{DMF (all forms)}} = 0.86 \pm 0.01$  molecules/nm<sup>2</sup> reveals nucleation of elongated islands at upper step edges (a) and on large terraces (b); (c-d) 8000 pulses to a DMF coverage of  $\Gamma_{\text{DMF (all forms)}} = 1.72 \pm 0.02$  molecules/nm<sup>2</sup> reveals continued growth and change in island aspect ratio.

Higher resolution STM images of these dark islands (Phase II) reveal molecularly-resolved features (Figure 4.5a). A fast Fourier transform (FFT) of the molecularly-resolved Phase II images gives near-square lattice parameters of  $5.86 \pm$

$0.02 \text{ \AA} \times 5.80 \pm 0.04 \text{ \AA}$ . The lattice constant for the elongated (fast growth) direction is commensurate with the substrate (twice the neighbor substrate atom spacing of  $2.89 \text{ \AA}$ ), consistent with the faster island growth along the substrate  $[\bar{1}\bar{1}0]$  close-packed direction. We attribute Phase II to a near-square arrangement of adsorbed DMF molecules, as the repeat distance is simply too small to accommodate a silver coordination complex. A proposed structural model of the DMF arrangement in Phase II is shown in Figure 4.5b. This model was additionally supported through DFT calculations with van der Waal corrections, and the structure of Figure 4.5b is the relaxed geometry from these calculations. A DMF adsorption energy of  $0.43 \text{ eV/molecule}$  is estimated from these calculations. Previous experimental<sup>75</sup> and computational<sup>76</sup> studies of molecular DMF have shown that DMF has a nearly planar structure due to  $\pi$  electron delocalization in the N-C=O group. The arc-like protrusions observed in STM images (Figure 4.5a) are thus attributed to the N-C=O group, and is consistent with the relaxed structural model (Figure 4.5b)

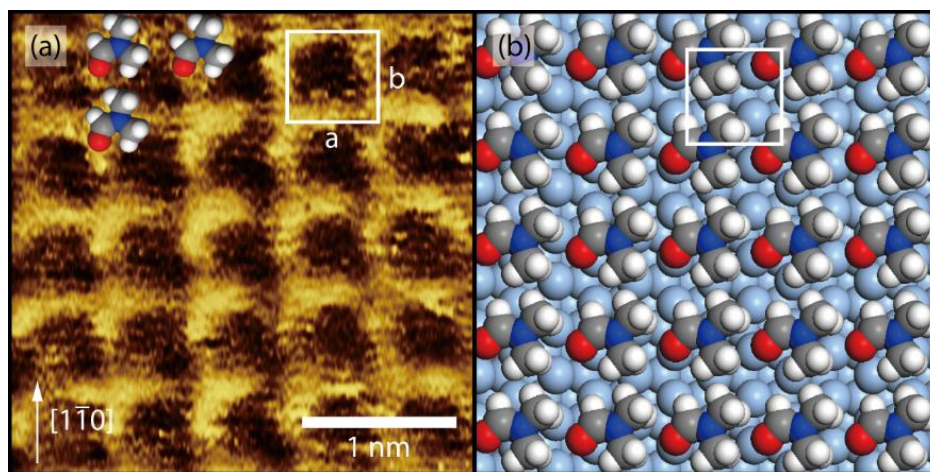


**Figure 4.5.** (a) Molecularly resolved UHV-STM image ( $3 \text{ nm} \times 3 \text{ nm}$ ) of Phase II and (b) the DFT + vdW computational relaxed model of DMF/Ag(111). Within this



structural model the N-C=O group corresponds to the arc-shaped protrusion in the STM image.

#### 4.3.3 Near-Saturation Monolayer: Condensation of Ag(DMF)<sub>2</sub> islands (Phase III)

Upon increasing the deposition amount to  $\Gamma_{\text{DMF (all forms)}} = 2.15 \pm 0.02$  molecules/nm<sup>2</sup>, a proliferation of bright islands (Phase III) nucleates within the disordered 2-D gas phase (Phase I) (Figure 4.6a). Higher resolution magnified STM images of the emergent bright islands reveal straight chains of protrusions, appearing predominantly as double rows (Figure 4.6b). The long axes of these chain structures are oriented in a wide range of angles, indicating a lack of registration to the Ag(111) substrate. In the following, we show that the double-row chain-like protrusions arise from the condensation of Ag(DMF)<sub>2</sub> coordination complexes within the disordered 2-D gas phase.

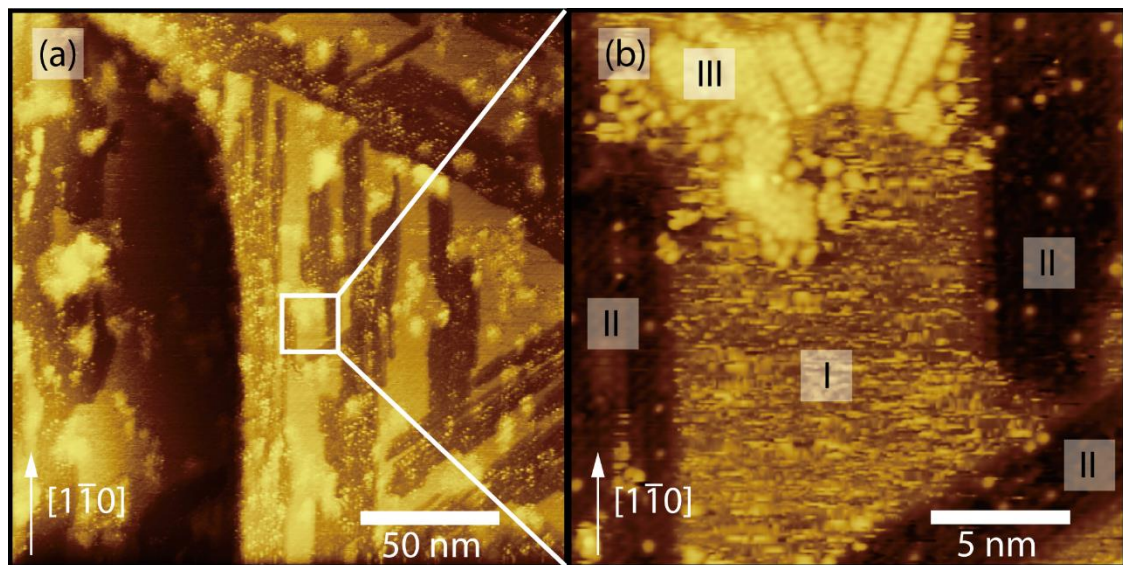


**Figure 4.6.** Onset condensation of Ag(DMF)<sub>2</sub> complexes (Phase II) at  $\Gamma_{\text{DMF (all forms)}} = 2.15 \pm 0.02$  molecules/nm<sup>2</sup>: (a) 200 nm × 200 nm image and (b) 20 × 20 nm image reveal coexistence of 2-D gas (Phase I), DMF island phase (Phase II) and Ag(DMF)<sub>2</sub> islands (Phase III).

#### 4.3.4 Saturated Monolayer: DMF (Phase II) – Ag(DMF)<sub>2</sub> (Phase III) Coexistence

Increased DMF deposition to 12000 DMF pulses at room temperature reaches a saturation coverage of  $\Gamma_{\text{DMF (all forms)}} = 2.58 \pm 0.02$  molecules/nm<sup>2</sup>, as shown in Figure 4.7a-c. At this coverage the 2-D gas phase (Phase I) has largely disappeared, and STM images reveal the coexistence of two phases – dark DMF islands (Phase II) and bright condensates of Ag(DMF)<sub>2</sub> complexes (Phase III) (Figure 4.7a,b). Higher resolution magnified images of Phase III reveal double-row chain-like structures, identified as linear chains of Ag(DMF)<sub>2</sub> complexes. The DMF ligands are imaged as bright protrusions, giving the double-row appearance. Evidently the Ag(DMF)<sub>2</sub> coordination complexes, which form upon etching Ag(111) (Figure 4.1b) and were identified by XPS spectroscopy in Phase I, require nearly saturation surface coverages in order to condense into linear aggregates. A structural model for these linear aggregates, consistent with STM images, is given in Figure 4.7d.

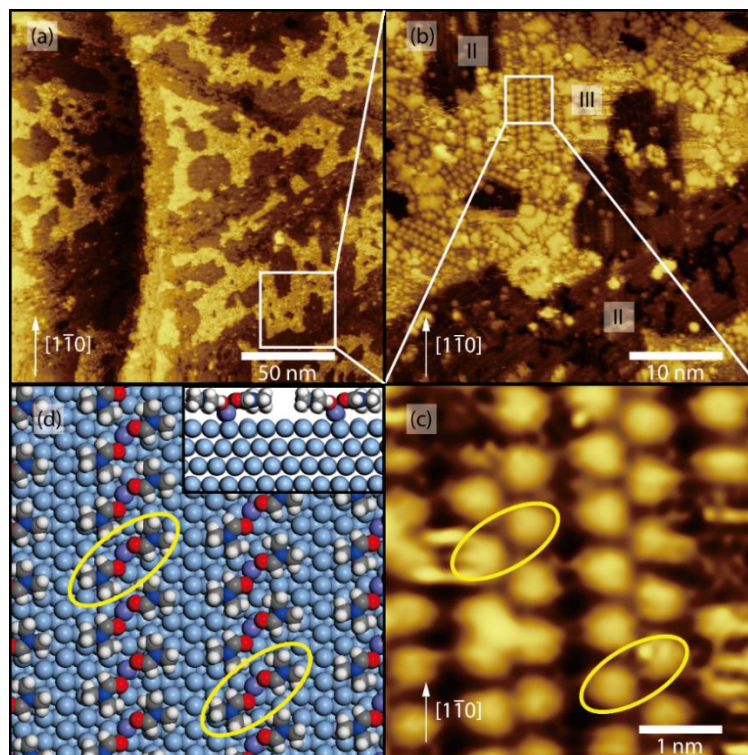


**Figure 4.7.** STM images of DMF-Ag(111) interface at saturation coverage: (a) Large scale image shows coexistence of Phase II and Phase III; (b) Higher resolution image shows re of double-row structures (Phase III) along the substrate  $[1\bar{1}0]$  direction; (c) Higher resolution magnified image of double-row structures; (d) Top-view and side-view of  $\text{Ag}(\text{DMF})_2$  double-row structural models.

The bright islands consist of condensed chains of  $\text{Ag}(\text{DMF})_2$  with an intra-chain nearest-neighbor  $\text{Ag}(\text{DMF})_2$  separation of  $0.705 \pm 0.003$  nm and an inter-chain next-nearest neighbor  $\text{Ag}(\text{DMF})_2$  separation of  $1.490 \pm 0.010$  nm. Interestingly, at saturation coverage, the azimuthal alignment of the  $\text{Ag}(\text{DMF})_2$  chains rotates from their initial alignment at lower coverage (Figure 4.6) to  $[1\bar{1}0]$  (Figure 4.7d). The surface pressure exerted by the surrounding DMF phase (Phase II) accounts for the

initial condensation of  $\text{Ag}(\text{DMF})_2$  and the subsequent chain rotation at higher coverages.

We note that the present images of  $\text{Ag}(\text{DMF})_2$  surface coordination complexes are consistent with previous STM studies of coordination complexes of  $\text{Cu}$ <sup>77</sup> and  $\text{Au}$ <sup>53,78</sup> on metallic surfaces, in that the coordinating metal atoms appear dark in the STM images. Feng and co-workers<sup>53,79</sup> have shown through DFT calculation that Au charge depletion occurred in Au-dimethylsulfoxide (DMSO) complexes on  $\text{Au}(111)$ , reducing available states of the coordinated Au adatoms for electron tunneling. In the present case, Ag – O coordination bond formation in the  $\text{Ag}(\text{DMF})_2$  structure evidently causes similar Ag charge depletion.

## 4.4 Discussion

### 4.4.1 Composition and Phase Diagram

We have shown that the increasing deposition of DMF on  $\text{Ag}(111)$  leads to the evolution of three distinct structural phases. The properties of these phases are summarized in Table 4.1. In the low coverage regime, a single 2-D phase (gas phase, Phase I) is formed. The composition of Phase I at this coverage regime was determined by XPS to be a mixture of DMF and  $\text{Ag}(\text{DMF})_2$ . With increasing coverage, Phase II (near-square DMF lattice islands) appear in co-existence with Phase I (2-D gas). Increasing DMF deposition increases DMF island sizes. As the saturation coverage approaches,  $\text{Ag}(\text{DMF})_2$  coordination complexes begin to condense (as Phase III) within the 2-D gas phase (Phase I). At the final saturation coverage, the 2-D gas phase (Phase I) is lost, and the surface consists of two

coexisting phases: Phase II (near-square DMF lattice islands) and Phase III (condensed islands of Ag(DMF)<sub>2</sub> chains).

**Table 4.1. Composition and Structure of Different Phases**

Phase	Composition	Structure	Density (adsorbates/nm <sup>2</sup> )
I	DMF, Ag(DMF) <sub>2</sub>	2-D gas	0 – 0.7 ± 0.1*
II	DMF	2-D near-square lattice, a = 5.86 ± 0.02 Å, b = 5.80 ± 0.04 Å	2.94 ± 0.02
III	Ag(DMF) <sub>2</sub>	2-D chain-like structure Intra-chain: 0.705 ± 0.003 nm Inter-chain: 1.490 ± 0.010 nm	0.86 ± 0.04

\*Maximum density is estimated from adsorbate density for Phase III.

In order to understand surface phase evolution, it is instructive to correlate observed phase transformations to surface pressure. Surface pressure (usu. represented as  $\Pi$ ) is the 2-D analogue of pressure in 3D. Adsorbed species can undergo phase transformations in response to surface pressure changes.<sup>58</sup> Several formulae have been developed and utilized to calculate the surface pressure in the monolayer regime.<sup>80</sup> The generalized Frumkin equation of state is the state-of-the art equation for multi-component systems, and was used here to estimate the surface pressure for the 2-D gas consisting of DMF and Ag(DMF)<sub>2</sub>.<sup>81</sup> The generalized Frumkin equation is:

$$\Pi = -\frac{k_B T}{a_\infty} \ln \left( 1 - \sum_i \Gamma_i a_{i\infty} \right) - \sum_{i,k} \alpha_{ik} \Gamma_i \Gamma_k, \quad Eq. (4.1)$$

$$a_\infty \equiv \frac{\sum_i \Gamma_i a_{i\infty}}{\sum_i \Gamma_i}, \quad Eq. (4.2)$$

where  $\Pi$  is the surface pressure,  $k_B$  the Boltzman constant,  $T$  temperature,  $a_{i\infty}$  the minimal possible area per molecule for component  $i$ ,  $a_\infty$  the average minimal possible area per molecule in a multicomponent mixture,  $\Gamma_{i(k)}$  is the number of molecules per unit monolayer area for component  $i(k)$  in the mixture,  $\alpha$  the interaction factor between different components. For simplicity, we neglect the interaction term  $\alpha_{ik}$ , an omission that is more justifiable in the low-medium pressure regime. We estimate  $a_{i\infty}$  from component packing densities measured in Phase II (near-square DMF lattice island) and Phase III (condensed islands of  $\text{Ag}(\text{DMF})_2$  chains), increasing each 2-D component volume by 10% to account for density increase upon condensation. Coverage values,  $\Gamma_{i(k)}$ , were determined directly from the statistical analysis of UHV-STM images.

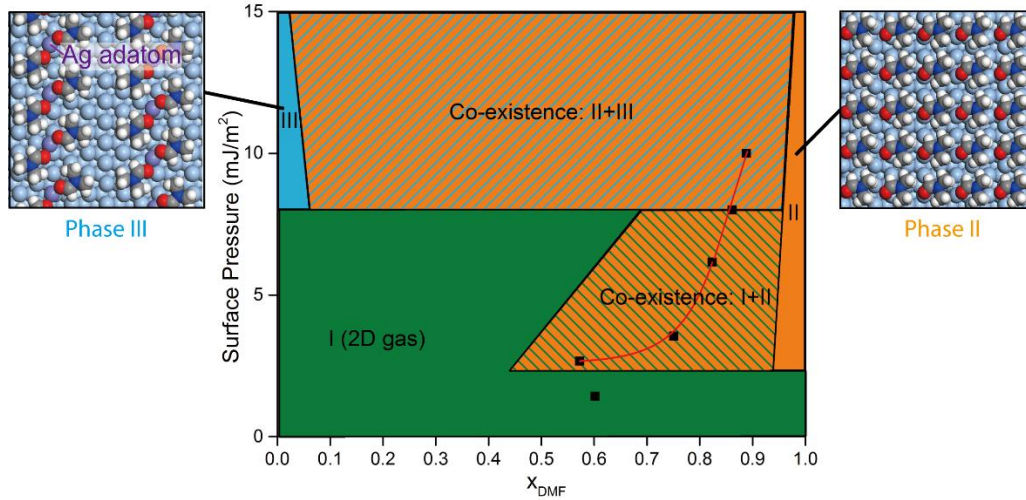


**Figure 4.8.** Surface Pressure – Composition phase diagram of the binary DMF- $\text{Ag}(\text{DMF})_2$  phases on  $\text{Ag}(111)$  at room temperature.  $X_{\text{DMF}} = \Gamma_{\text{DMF}} / (\Gamma_{\text{DMF}} + \Gamma_{\text{Ag}(\text{DMF})_2})$ . Actual measured points shown as squares. Surface pressure is estimated from Eq. (4.1).

The surface pressure and composition information extracted from measurements allows us to construct a semi-quantitative composition vs. surface pressure phase diagram (Figure 4.8). The composition of the DMF-Ag(DMF)<sub>2</sub> binary phases is shown along the horizontal axis, and the calculated surface pressure is shown along the vertical axis. The three observed phases—Phase I (2-D gas), Phase II (near-square DMF lattice island) and Phase III (condensed islands of Ag(DMF)<sub>2</sub> chains) are represented by three different solid colors. Two phase co-existence regions—region I+II and region II+III are represented as hatched colors of the coexisting phases. The square data points represent the actual sequential DMF deposition experiments. In general, surface pressure increases with surface coverage. The singular Phase I (2D gas) is observed only at lower surface pressures. Increasing coverage (2-D pressure) drives the film, in turn, through the co-existing I+II region and then the co-existing II+III regions.

#### 4.4.2 Phase Evolution and Surface Energetics

We next relate the phase evolution to the distinct surface chemical properties of the two components, DMF and Ag(DMF)<sub>2</sub>. According to our DFT computation, DMF has a binding energy of just 0.43 eV/molecule on Ag(111), indicating a relatively weak surface interaction. However, DMF also has a substantial dipole moment of 3.86 D, and head-to-tail DMF-DMF dipolar interactions help drive island formation, and formation of needle-like islands. Alignment of the DMF islands (fast growth direction) with the underlying Ag lattice along  $[1\bar{1}0]$ , indicates DMF island growth is also favored by electronic interaction with the Ag substrate. This is consistent with the fact that the formation of DMF islands occurs at a relatively low surface pressure.

In contrast, nucleation of Ag(DMF)<sub>2</sub> islands requires  $\sim 3$  higher surface pressure than the onset of DMF islands. Moreover, Ag(DMF)<sub>2</sub> islands are not in atomic registration with the substrate at lower surface pressures. Only after surface pressure exceeds  $\Pi = \sim 8 \text{ mJ/nm}^2$  do Ag(DMF)<sub>2</sub> chains align with the underlying Ag lattice along  $[1\bar{1}0]$ . Linear Ag(DMF)<sub>2</sub> chains are stabilized by weakly attractive O··H intra-chain hydrogen-bonding interactions. However inter-chain interactions involve H to H “contacts” that are largely repulsive. This accounts for the higher 2-D pressures needed to condense Ag(DMF)<sub>2</sub> islands and the  $0.22 \pm 0.02 \text{ nm}$  gap and offset-registration in neighboring Ag(DMF)<sub>2</sub> chains. The alignment of Ag(DMF)<sub>2</sub> islands to the substrate  $[1\bar{1}0]$  direction as saturation coverage is approached is attributed to anisotropic surface stress that results from coexisting  $[1\bar{1}0]$  registered DMF islands.

We now consider the energetics of Ag(DMF)<sub>2</sub> formation, which involves the complexation of DMF with Ag adatoms, as described in Scheme 4.3. We estimate the energetics of surface Ag(DMF)<sub>2</sub> formation from two microscopic steps: Step (i) is the detachment of Ag adatoms from the Ag(111) monatomic step edge, with a reported energy cost of 0.515 eV/atom based upon Effective Medium Theory (EMT) calculations<sup>82</sup>. Step (ii) is the complexation of the Ag adatom with two adsorbed DMF molecules, with an associated energy gain of 0.577 eV/molecule based on our present DFT computations. The overall reaction to form Ag(DMF)<sub>2</sub> has an energy change of 0.062 eV/molecule, consistent with its spontaneous formation. This small energetic preference for Ag(DMF)<sub>2</sub> formation is also consistent with the observed coexistence of adsorbed DMF and Ag(DMF)<sub>2</sub>. The equilibrium constant  $K_{\text{eq}}$  for complex formation at room temperature is roughly  $e^{-\Delta E/kT} = 0.08$ , which is consistent



with the experimentally observed equilibrium constant at saturation coverage,  $K_{\text{eq, exp}} = \theta_{\text{Ag(DMF)}_2} / \theta_{\text{DMF}}^2 \approx 0.06$ . Additional support that the system is in equilibrium is provided by the stability of the surface phases. For a given surface coverage (phase composition), negligible change in surface phase composition was observed in STM measurements acquired over a 48-hour period at room temperature or following mild thermal annealing (to 343 K).



**Scheme 4.3.** The formation of  $\text{Ag}(\text{DMF})_2$  and two underlying reaction steps.

#### 4.4.3 Coordination Chemistry of Ag: Surface vs. Solution and Solid State

Finally, we compare the  $\text{Ag}(\text{DMF})_2$  surface adatom coordination complex with the  $\text{Ag}^+(\text{DMF})_n$  coordination complex found in both liquid and solid phases.  $\text{AgL}_n^+$  complexes exhibit different geometries with coordination numbers depending on the environment.<sup>83</sup> In pure ligand solvents, Ag typically forms  $\text{AgL}_4^+$  complexes with a tetrahedral geometry. Indeed, an extended X-ray absorption fine structure spectroscopy (EXAFS) study showed that  $\text{Ag}(\text{DMF})_4^+$  forms a tetrahedron through Ag-O bonding in neat DMF.<sup>84</sup> However,  $\text{Ag}^+$  is known to favor the linearly coordinated  $\text{AgL}_2^+$  in other liquid and solid phases.<sup>83</sup> The coordination number of the  $\text{Ag}(\text{DMF})_2$  surface coordination complex matches that of the linearly coordinated  $\text{AgL}_2^+$ , presumably reflecting a partial positive charge-state of the Ag coordination atom, and its interaction with the Ag(111) substrate.

We have shown that the interaction between the polar heterosolvent DMF and Ag(111), an important electrode and catalyst, leads to the spontaneous formation of Ag(DMF)<sub>2</sub> surface coordination complexes in co-existence with surface DMF. This has important implications for surface chemistry and electrochemistry under such polar solvents. Coexisting DMF and Ag(DMF)<sub>2</sub> phases have distinct structures and surface potentials. Such surface heterogeneity will translate to local variations in surface chemical and electrochemical processes. For example, rates for solute deposition or reaction under weak driving potential will differ substantially over different phases. Complexation effects should be taken into account for accurate descriptions of polar solvent – electrode metal surface systems.

#### 4.5 Summary

We have presented experimental and theoretical investigations of the surface chemistry between the highly polar heterosolvent, DMF, and a model metal electrode surface, Ag(111). Liquid microaerosol depositions on Ag(111) leads to the spontaneous formation of the Ag(DMF)<sub>2</sub> coordination complex and coexistence of DMF<sub>(ads)</sub> and Ag(DMF)<sub>2</sub>. The Ag(DMF)<sub>2</sub> coordination complexes form by coordination of DMF carbonyl oxygen atoms to Ag adatoms. With increasing DMF deposition, the attendant increase in surface pressure drives a series of phase transformations from Phase I (2-D gas mixture of DMF<sub>(ads)</sub> and Ag(DMF)<sub>2</sub>) to coexisting Phase I and Phase II (near-square DMF lattice islands) to coexisting Phase II and Phase III (condensed islands of Ag(DMF)<sub>2</sub> chains). The near-square DMF lattice phase (Phase II) has a unit cell of  $5.86 \pm 0.02 \text{ \AA} \times 5.80 \pm 0.04 \text{ \AA}$ , and consists of head-to-tail arrangements of DMF dipolar molecules. STM images resolve the

delocalized N-C-O  $\pi$  bond as an arc-like protrusion. The chain-like  $\text{Ag}(\text{DMF})_2$  islands (Phase III) consist of  $\text{Ag}(\text{DMF})_2$  chains arranged with intra-chain distance of  $0.705 \pm 0.003$  nm and inter-chain distance of  $1.490 \pm 0.010$  nm. Chain-Chain interactions at this distance are slightly repulsive, and thus this phase is observed only at near saturation coverage, where surface pressure overcomes chain-chain repulsion.

A semi-quantitative pressure-composition phase diagram was developed to assist in the interpretation of 2-D phase equilibria, and to allow for future phase prediction under other experimental conditions. The discovery of  $\text{Ag}(\text{DMF})_2$  coordination complex formation on  $\text{Ag}(111)$  reveals the complexity of DMF interaction with silver and expands our understanding of silver coordination chemistry on the surface. The ordering of  $\text{Ag}(\text{DMF})_2$  under surface pressure (here induced by co-adsorbates) presents a useful strategy to control the surface morphology at interfaces and expand the available molecular architecture on metal surfaces.

## Chapter 5 Lithium Ethylene Dicarboxylate (LEDC) –

### Dimethylformamide (DMF) Monolayer Films on Ag(111)

Chapter 4 revealed DMF-Ag(111) interactions and interface evolution as a function of DMF coverage. This highly polar solvent is also able to dissolve LEDC, a key component of the early-stage solid electrolyte interphase (SEI) formation. In Chapter 5 we undertook STM structural investigations of this key SEI component. In particular, we examined the structure of monolayer films generated on Ag(111) by the pulsed aerosol deposition of LEDC in DMF solution. This is a collaborative work between myself, Kang Xu and Peter Zavalij. I prepared all thin film samples and did all STM measurement. Kang Xu synthesized the LEDC. Peter Zavalij performed XRD measurement at the University of Maryland College Park and analyzed the data with some assistance from me. I prepared the sample for synchrotron XRD measurement, performed at Argonne National Laboratory (ANL) by ANL staff.

#### 5.1 Introduction

The liquid electrolyte in commercial Li-ion batteries (LIB) is a mixture of ring molecular carbonates and linear molecular carbonates (Figure 5.1, ring carbonates and linear carbonates). The ring carbonates used are generally ethylene carbonate (EC), fluoroethylene carbonate (FEC) and vinylene carbonate (VC), while the linear carbonates include dimethyl carbonate (DMC), ethylmethyl carbonate (EMC) or diethyl carbonate (DEC). During the charging cycle, the reductive decomposition of ring carbonates and linear carbonates leads to the formation of the solid electrolyte interphase (SEI)<sup>28</sup>. As described in Chapter 3, the reductive decomposition products

of linear carbonates are lithium alkyl monocarbonates ( $\text{LiOOCOR}$ , R is the alkyl group), with exact chemical formula depending on the linear carbonate in use. The reductive decomposition product of ethylene carbonate (EC) is lithium ethylene dicarbonate ( $(\text{CH}_2\text{OCOOLi})_2$ , LEDC) (Figure 5.1, one key SEI early-stage product). Due to the almost universal presence of ethylene carbonate (EC) in the liquid electrolyte formula in LIB, LEDC has been intensively studied both experimentally and theoretically.<sup>29,44,85-87</sup>

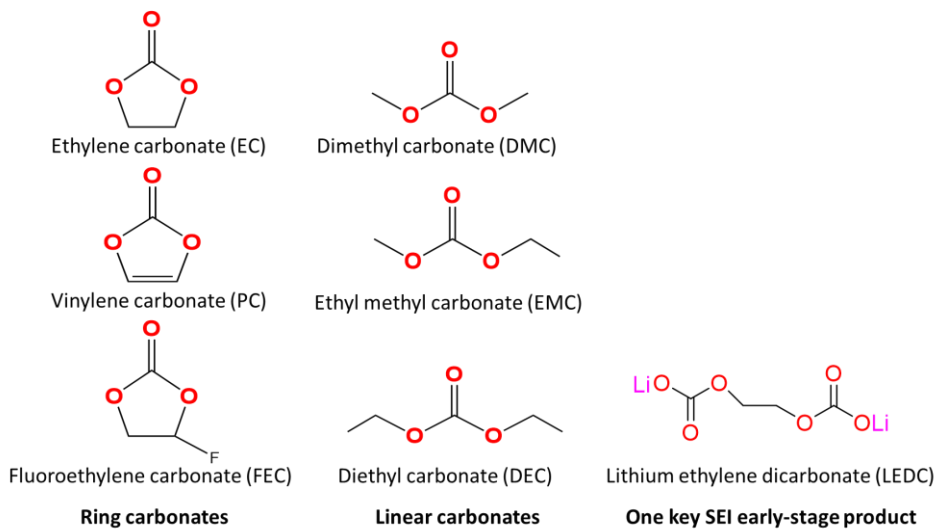


**Figure 5.1.** Molecular structures of ring carbonates and linear carbonates as well as SEI early-stage product—lithium ethylene dicarbonate (LEDC).

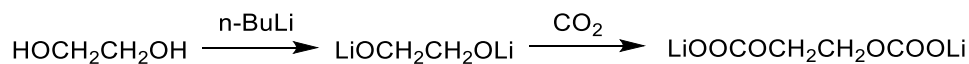
Lithium ethylene dicarbonate (LEDC) is an organolithium salt. It is a moisture sensitive material and undergoes thermal decomposition at an onset temperature of 120 °C.<sup>44</sup> The synthesis of pure LEDC has been achieved by different routes.<sup>26,44</sup> The ion conductivity of LEDC was measured to be  $1 \times 10^{-9}$  S/cm by electrochemical impedance spectroscopy (EIS),<sup>86</sup> and there is much interest in relating this ion conductivity to the LEDC crystal structure. Previous conventional powder X-ray

diffraction studies on bulk LEDC have determined that LEDC has an orthorhombic unit cell with a lattice constant of  $a = 14.100 \text{ \AA}$ ,  $b = 12.66 \text{ \AA}$ , and  $c = 5.20 \text{ \AA}$ .<sup>87</sup> However, the detailed coordinates of the LEDC structure could not be determined from these lower resolution measurements. In this thesis, the structure of LEDC was revisited with synchrotron X-ray diffraction at the Argonne National Laboratory (ANL) to obtain high-resolution data for crystal structure determination. To complement these reciprocal space investigations, we additionally prepared ultrathin LEDC films on Ag(111) using a microaerosol liquid deposition method. The resulting LEDC films were imaged by UHV-STM to determine molecular-level details of the 2D film structure and interaction with its polar solvent dimethylformamide (DMF). The combined efforts to resolve the structures of both bulk and thin-film LEDC provide further insight on the role of LEDC in the solid electrolyte interphase (SEI) formation.

## 5.2 Experimental Methods

Pure LEDC has been synthesized by two different methods in this work.<sup>26,87</sup> LEDC synthesized by the Duma-Peligot method (Scheme 5.1) was used in both the synchrotron and conventional X-ray measurements and the STM measurements, due to its higher purity as indicated by nuclear magnetic resonance (NMR) spectroscopy.<sup>26,87</sup> The LEDC synthesis was performed at the US Army Research Lab by collaborator Dr. Kang Xu, and subsequently transferred and preserved under nitrogen until use. For the conventional XRD measurement, a Bruker D8 Advance system with a  $\text{CuK}\alpha$  radiation source was used and the moisture sensitive material was hermetically sealed in a plastic sample container in the nitrogen glovebox. The

laboratory XRD data collection time was 8 hours. For the synchrotron measurements, LEDC powder was directly loaded into the Kapton capillary tube inside the nitrogen glovebox. Under nitrogen atmosphere, the Kapton capillary tube ends were sealed by epoxy (Devcon), cured for 5 mins, and assembled with the tube mounting base and magnetic cap. This procedure provided sufficient atmosphere insulation based on previous moisture-sensitive material studies by other workers, as confirmed by the present measurements. Synchrotron measurements were performed at the 11-BM beamline synchrotron facility at the Argonne National Laboratory (ANL). Data was collected at 295.0 K with a X-ray wavelength of 0.41384 Å (30 keV) and standard scan time of ~1 hr. The resulting diffraction data are shown in the results section.



**Scheme 5.1.** Synthesis of LEDC using the Duma-Peligot based method.

For the microaerosol liquid deposition method, the LEDC-saturated DMF solution was prepared in the following manner: 25 ml of dimethylformamide (DMF) (Sigma-Aldrich, anhydrous, 99%) solvent was first transferred into a sealed 25 ml glass container (Corning) inside the nitrogen glovebox. The LEDC powders were gradually added into the DMF solvent until LEDC solubility diminished and LEDC precipitated out of solution. The sealed container was then extracted from the glovebox and sonicated for 30 mins to assist the dissolution of LEDC in DMF. The concentration of the LEDC-saturated DMF solution was estimated to be ~0.4 M based on the solubility of lithium propylene dicarbonate (LPDC) in DMF (LPDC has a high structure similarity to LEDC)<sup>44</sup>. The sonicated solution was then moved back

into the glovebox and filtered through a PTFE filter (pore size: 0.22  $\mu\text{m}$ ) to remove undissolved LEDC. The resulted homogenous LEDC/DMF solution ( $\sim 0.4$  M) was transferred into an air-tight glass syringe (Hamilton 2.5 mL) for liquid microaerosol deposition. The deposition procedure was as previously described in Chapter 4.

## 5.3 Results

### 5.3.1 X-ray diffraction studies of bulk LEDC

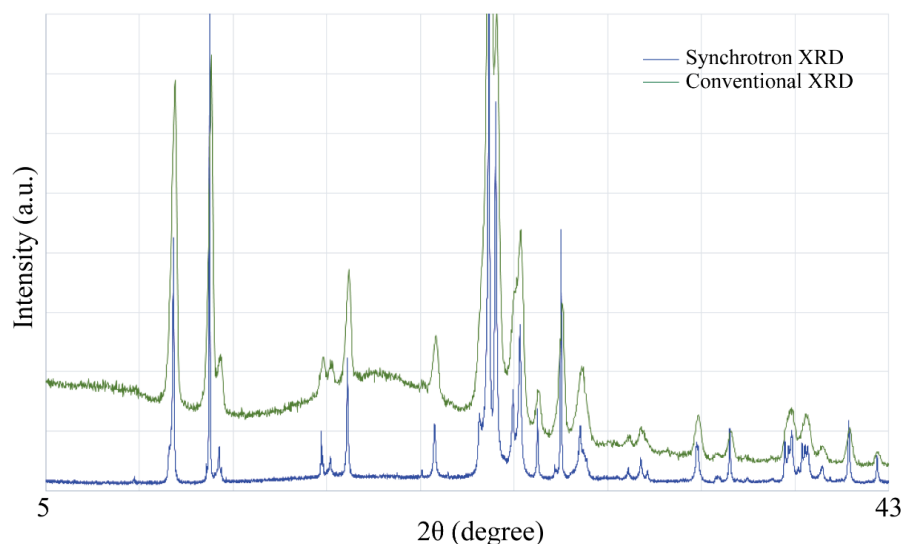


**Figure 5.2.** X-ray diffraction data for bulk LEDC: synchrotron data (blue trace) and conventional data (green trace).

Synchrotron and conventional XRD measurement data are shown in Figure 5.2. To determine the crystal structure, the X-ray diffraction pattern was compared to that of simulated structure using the TOPAS software package.<sup>88</sup> For these simulations, the number of LEDC per unit cell was assumed to be 4-6, corresponding to LEDC densities in the range  $1.16 \text{ g/cm}^3$ - $1.74 \text{ g/cm}^3$  that is typical of organic materials. A thorough testing of the relevant point groups—from more symmetric Pnca to less



symmetric P21/c, P21/n, and Pcn2 did not produce a satisfactory fit. The effort to resolve the structure is still in progress.

### 5.3.2 STM imaging of microaerosol-deposited LEDC/DMF films

In Chapter 4, we showed that the deposition of pure DMF solvent on Ag(111) produced a phase progression from a 2D disordered phase to ordered DMF islands and ordered  $\text{Ag}(\text{DMF})_2$  complexes with increasing coverage. We now show that the presence of the LEDC solute in the DMF solvent shifts this phase evolution. In particular, for films deposited from the LEDC saturated solution ( $\sim 0.4$  M), ordered DMF islands nucleate at a factor of four lower DMF coverages ( $\Gamma_{\text{DMF}} = 0.22 \pm 0.01$  molecules/ $\text{nm}^2$ ) than found in the pure DMF films ( $\Gamma_{\text{DMF}} = 0.86 \pm 0.01$  molecules/ $\text{nm}^2$ ). (Figure 5.3)

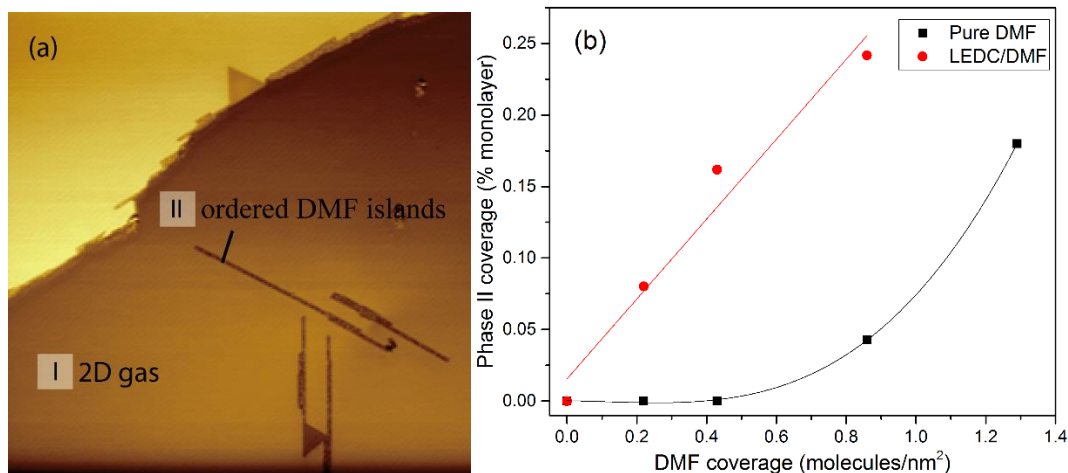


**Figure 5.3.**(a) Aerosol deposited films from LEDC-saturated DMF solution: STM image ( $200 \text{ nm} \times 200 \text{ nm}$ ) at a DMF coverage of  $0.22 \pm 0.01$  molecules/ $\text{nm}^2$  revealed two coexisting phases—2D gas (Phase I) and ordered DMF islands (Phase II), (b) coverage of ordered DMF islands (Phase II) plotted as a function of DMF coverage.

## 5.4 Discussion

The phenomenon of the early nucleation is summarized qualitatively in a DMF coverage vs. temperature phase diagram (Figure 5.4). The 2D gas-ordered DMF phase boundary has been shifted to the low coverage direction in the LEDC-saturated DMF solution deposition vs. pure DMF.

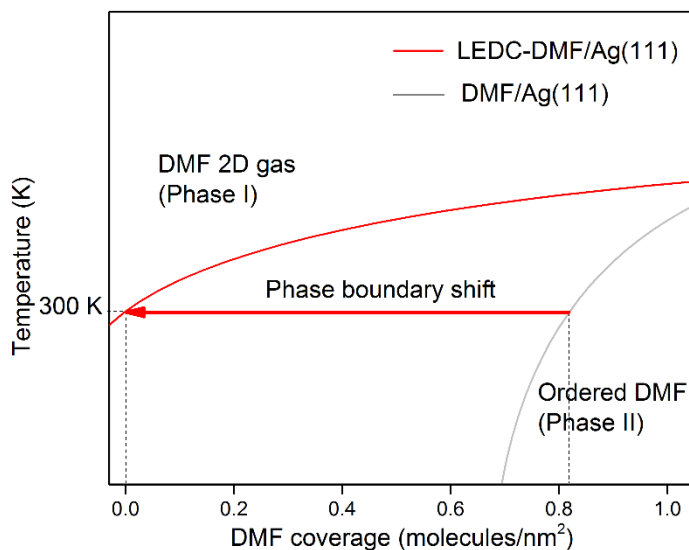


**Figure 5.4.** DMF coverage-temperature phase diagram in the submonolayer  $0 - 1.00 \pm 0.05$  DMF/nm<sup>2</sup> regime. The 2D gas-ordered DMF phase boundary shift is indicated by the red arrow.

The impact of the LEDC solute on the nucleation of DMF islands is understood through nucleation theory. The nucleation phenomenon has been extensively studied<sup>89</sup>, including studies of homogeneous nucleation and heterogeneous nucleation. The classical nucleation theory<sup>90,91</sup> states that the nucleation energy  $E$  is the sum of the interfacial energy  $\gamma$  per unit area between the phases and the difference in free energy per unit volume between the phases  $\Delta F$ , expressed as

$$E = -\Delta F + \gamma \quad (\text{Eq. 5.1})$$

The energy barrier for nucleation is the nucleation energy maximum, which determines the nucleation rate. The classical nucleation theory fails in the regime where the critical nucleus is very small (often 20-50 molecules) or the molecules are polar. In the present DMF/Ag(111) and LEDC-DMF/Ag(111) systems, DMF is a polar molecule (dipole moment: 3.86 D) and the critical nucleus size is < 50 molecules, as indicated by the STM measurement of the width of ordered DMF islands (phase II) at low ( $0.22 \pm 0.01$  molecules/nm<sup>2</sup>) DMF coverage. In this size regime, the classical nucleation approach has generally been superseded by the more predictive density functional approach.<sup>89</sup> In this density functional approach, the nucleation energy barrier is determined by the critical density profile  $\rho^*(r)$  rather than just the critical radius  $r$ . The critical density profile  $\rho^*(r)$  is the saddle point in the formation of the new phase: before the saddle point the cluster tends to shrink while after the saddle point the cluster tends to grow. Once the cluster of the critical density profile  $\rho^*(r)$  has formed, further nucleation becomes energetically favorable. In the DMF/Ag(111) case (discussed in Chapter 4), ordered DMF condensed from the disordered DMF 2D gas from line defects (step edge) on a large terrace on Ag(111). Evidently, upper step edges interact more favorably with the adsorbed DMF molecules and possibly increase the 2D local density of DMFs beyond the critical density  $\rho^*(r)$  based on the density functional approach, leading to the nucleation of ordered DMF islands. Similarly, in the LEDC-DMF case, LEDC is an organolithium ionic salt, consequently solvation of 2D LEDC-DMF also increases the local density of DMF on Ag(111) surface and drives the early nucleation of ordered DMF islands.

In the LEDC-DMF case, the local density of DMF is higher than that in the pure DMF case at the same total surface DMF coverage. This suggests that the ion ( $\text{Li}^+$ )-dipole (DMF) interaction is stronger than the weaker Ag step edge – DMF interaction. This effect shifts the 2D gas-DMF island phase boundary towards lower DMF coverage (Figure 5.4).

In order to obtain a further insight of how LEDC seeds nucleation, we must consider the LEDC surface coverage. Based on the concentration of LEDC in DMF at room temperature of  $\sim 0.4$  M and the assumption that the relative LEDC:DMF concentration is preserved on transfer to Ag(111), the ratio between LEDC molecules and DMF molecules is 1.0 LEDC : 32.5 DMF. (The greater volatility of DMF makes this an upper bound for DMF). Accordingly,  $\sim 8$  LEDC molecules are expected in a phase II region of  $100 \text{ nm}^2$ . The molecularly resolved image of the LEDC-seeded DMF islands with this area is shown in Figure 5.5. In addition to the DMF molecules, arranged in a near-square lattice shown with red unit-cell guidelines, larger protrusions are also present. The larger protrusions, labelled in green, are less regularly ordered. As such structures are not observed in pure DMF islands, we attribute them to LEDC. Based upon this assignment, we can explore structural models for the LEDC seeds embedded in the DMF islands. Fig. 5.6 provides a perspective view of a model of a single LEDC “seed” and the surrounding DMF layer. In this structural model, the longer axis of the LEDC molecule has a dimension of  $\sim 10 \text{ \AA}$  (measured from  $\text{Li}^+$  center to  $\text{Li}^+$  center), approximately twice that of the DMF-DMF distance in the ordered DMF islands. In this model, the DMF molecules are flipped at the end of the LEDC due to preferred electrostatic interaction between

$\text{Li}^+$  and the carbonyl oxygen in DMF. In the actual film, the two “flipped” DMF molecules are likely to be disordered and may not be imaged directly. This appears to be the case in the actual STM image: in Figure 5.5, the bright protrusion (LEDC) has depressions on either side, which may reflect the presence of the flipped DMF. The DMF-LEDC-DMF complex, circled in Figure 5.6, has a width of 2.4 nm, roughly half of the width of the DMF islands at lowest DMF coverage case ( $\Gamma_{\text{DMF}} = 0.22 \pm 0.01$  molecules/ $\text{nm}^2$ , Figure 5.3(a)). It is also worth noting that the LEDC bright protrusions are formed in the central region of the DMF islands and aligned along the long DMF island axis (or fast growth direction). This may reflect attractive LEDC-LEDC interactions or LEDC-Ag(111) interactions.

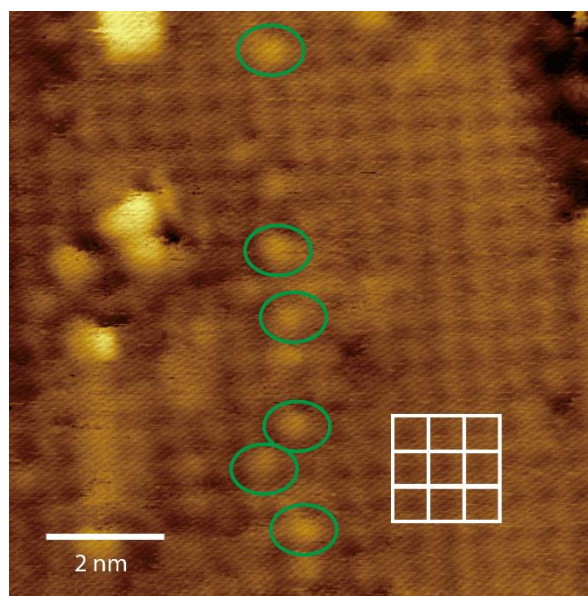


**Figure 5.5.** UHV-STM image ( $10 \text{ nm} \times 10 \text{ nm}$ ) of LEDC-seeded DMF islands with  $0.43 \pm 0.01 \text{ DMF}/\text{nm}^2$  on Ag(111). White grid shows the DMF unit cell repeat. Protrusions encircled in green are attributed to solvated LEDC.

A proposed structural model of LEDC/DMF on Ag(111) is given in Figure 5.6.

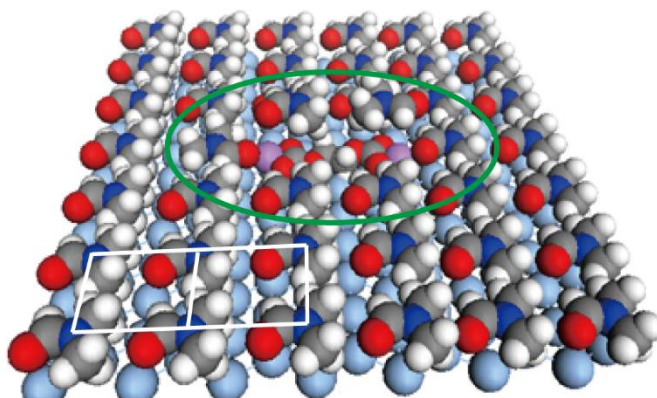


**Figure 5.6.** Structural model of DMF-solvated LEDC on Ag(111). The white grid shows the DMF unit cell repeat and the green ellipse shows solvated LEDC.

## 5.5 Summary

I have found that LEDC solutes seed early nucleation of ordered DMF islands in monolayer films on Ag(111). I attribute this early nucleation to the formation of a solvated LEDC structure. The formation of DMF solvated LEDC structures within the 2D DMF gas on Ag(111) increases the local density of DMF about LEDC. This increase in local density accounts for the early nucleation of the ordered DMF islands. High resolution STM images of the DMF islands seeded by LEDC show irregular protrusions in addition to the regularly ordered DMF features. These irregular protrusions are tentatively assigned to the LEDC solute seeds. A structural model of the solvated solute seeds, embedded in the DMF film network, is presented. The width of the solvated solute seed (~2.5 nm) is comparable to the width of the smallest LEDC-seeded nucleation islands (~5 nm). This may mean the actual “seed” contains at least 2 additional DMF molecules, or that the observed islands have coarsened (grow larger than the seed) before captured by the STM.

The impact of the LEDC solute on the solvent structure may also play an important role in the early-stage SEI formation. In actual Li-ion battery systems, electrolyte molecules such as ethylene carbonate and dimethyl carbonates also have significant molecular dipole moments and dielectric constants, comparable or even larger in magnitude to DMF. Such polar solvents can likewise be expected to solvate LEDC, as well as other organolithium and inorganic lithium components of the early state SEI. This solvation will increase the specific adsorption of polar solvent molecules at the electrode surface, leading to further reductive decomposition of the electrolyte molecules upon battery cycling. This mechanism is a key step in the passivation layer formation on the electrode surface.

High-resolution synchrotron X-ray diffraction data of bulk LEDC confirmed that this organolithium salt to be pure and highly ordered. Computer simulation of the diffraction features should, in principle, allow us to determine the exact position of all atomic coordinates in the LEDC crystal structure. However, the relatively weak X-ray scattering of lithium make it difficult to locate the lithium positions in computer simulation by X-ray measurements alone. To assist the structural determination from X-ray, complementary information on the structural position of the lithium ions is needed, possibly through neutron diffraction measurements.

## Chapter 6 Summary and Outlook

In this dissertation, two surface science models have been created under ultra-high vacuum (UHV) to understand the very initial stage of solid electrolyte interphase (SEI) formation at carbon anode surfaces in the LIB. The first model system, Model System I, is an electrolyte-Li/graphite C(0001) system. The detailed interactions between the molecular electrolyte and the model carbon anode surfaces with varied extent of lithiation has been revealed. These detailed interactions range from simple physical adsorption to more complex reductive chemical reactions. The resultant reductive reaction products were identified and further quantified by tracking their thermal decomposition products. One of the key products formed, lithium ethylene dicarbonate (LEDC), is the reductive decomposition product of the universal electrolyte, ethylene carbonate (EC). LEDC was singled out for further structural studies. Two different approaches have been adopted to study the structure of LEDC. The first involved synchrotron X-ray diffraction on synthesized pure LEDC to determine the exact atomic coordinates in its bulk crystals. The second applied the liquid microaerosol deposition technique to fabricate lithium ethylene dicarbonate (LEDC) – dimethylformamide (DMF) thin films on Ag(111). Further imaging of the monolayer thin film structure was done by ultra-high vacuum - scanning tunneling microscopy (UHV-STM). The obtained LEDC-DMF thin film structure provided new insight on how LEDC can increase the specific adsorption of polar solvent molecules at the electrode surface, leading to further reductive decomposition of the electrolyte molecules upon battery cycling. This mechanism is a key step in the passivation layer formation on the electrode surface.



Another component of this PhD research was the development of a temperature programmed desorption/temperature programmed reaction spectroscopy (TPD/TPRS) system to study the interactions in Model System I (electrolyte-Li/graphite C(0001) system). The temperature programmed desorption (TPD) technique measures the desorption energy of adsorbed molecules on the substrate surface, revealing the binding strength and film growth mechanisms of the adsorbed molecules. The temperature programmed reaction spectroscopy (TPRS) method simultaneously monitors different desorption products from the reactive surface. In this work, TPRS provided the first quantitative branching ratios of the surface chemical reactions under study.

The findings from the two model systems are summarized in the following paragraphs:

In Chapter 3, molecular carbonates have been studied and varying strengths of interactions were found between the molecular electrolytes and lithium-graphite substrate. Weak physisorptive interaction was found for EC and DMC on clean graphite (C(0001)). Chemisorptive interaction was found for EC and DMC on lithiated graphite ( $\text{Li}^+/\text{C}(0001)$ ). Reductive decomposition was observed for EC on metallic lithium ( $\text{Li}(s)/\text{C}(0001)$ ). In the weakly interacting case, TPD measurement revealed that EC de-wets the clean graphite surface and forms 3D islands. The measured desorption energy matches vaporization enthalpy of EC, indicating EC desorbs from the 3D islands. Interestingly, DMC was found to wet the clean graphite C(0001) surface and the desorption energy was measured as  $0.64 \pm 0.05$  eV. On the lithiated C(0001) surface, EC and DMC were found to bind more strongly and to

form 2D solvation shell-like structures on lithiated graphite ( $\text{Li}^+\text{-C}(0001)$ ). On metallic lithium supported on graphite, TPRS revealed that metallic Li ensues the decomposition of EC. The different reaction pathways were related to desorption products, and branching ratio was determined to be 70.%(organolithium products) : 30%( inorganic lithium product). The obtained branching ratio provides important information on the distribution of lithium salts that form at the very onset of SEI formation.

In Chapter 4, the focus was on a key component in the SEI, LEDC. In the investigation of LEDC-DMF/Ag(111) model system, the LEDC was solvated in the aprotic polar solvent DMF and the LEDC-saturated DMF solution was delivered to the Ag(111) by the microaerosol liquid deposition method. The interactions between the dimethylformamide (DMF) and Ag(111) were additionally investigated in control studies. In the DMF/Ag(111) studies, two different species were identified and characterized on Ag(111): the adsorbed DMF, and  $\text{Ag}(\text{adatom})\text{DMF}_2$  coordination complexes. As DMF coverage increases from low coverage to a full monolayer, the state of the surface evolves. The two species present on Ag(111), adsorbed DMF and  $\text{Ag}(\text{adatom})\text{DMF}_2$ , undergo phase separation and transformations at different DMF coverage. At lower coverages, adsorbed DMF and  $\text{Ag}(\text{adatom})\text{DMF}_2$  form a 2D gas mixture. At intermediate coverages, the adsorbed DMF undergoes partial phase separation and condensation into ordered DMF islands from the 2D gas mixed binary phase. Approaching saturation coverage, the  $\text{Ag}(\text{adatom})\text{DMF}_2$  complex condenses from the disordered 2D gas phase, into ordered chain-like structure. A semi-

quantitative composition-surface pressure phase diagram was developed to summarize the phase evolution.

Chapter 5 is a continuation of the effort to obtain structural information on the early-stage SEI formation. The LEDC-saturated DMF solution was deposited on Ag(111) and the formed LEDC-DMF monolayer film was compared to that deposited from DMF alone. Pure LEDC was synthesized and characterized by synchrotron X-ray diffraction, to confirm phase purity. The LEDC-saturated DMF solution was deposited on Ag(111) using microaerosol liquid deposition and the surface morphology was measured by UHV-STM. The ordered DMF islands appear  $\times 4$  lower DMF deposition coverage in LEDC-saturated DMF than that in pure DMF deposition. This early nucleation of ordered DMF islands was attributed to the seeding effect of LEDC-DMF solvation structure on Ag(111). The ionic ( $\text{Li}^+$ )-dipole (DMF) interaction between LEDC and DMF increases the local DMF density, shifting the boundary between 2D gas-ordered DMF phase transformations towards lower DMF deposition coverage direction. The seeded nucleation of ordered DMF islands has implication on the mechanism of early-stage SEI formation. At an LIB's interface, the formed LEDC would attract the polar electrolyte solvent to the electrode surface, and accelerate the SEI formation.

For this thesis, I have expanded knowledge through model interfaces related to the Li-ion battery energy storage system, especially on the initial formation of the SEI. The knowledge obtained could help design new electrolyte formula that could improve the electrode-electrolyte interface property or design new electrode surfaces, thereby leading to the Li-ion battery that is safer and has longer cycle life.

Based on the results from this dissertation, I proposed the following experiments to further understand the early-stage SEI formation:

The X-ray synchrotron diffraction studies of pure lithium ethylene dicarbonate (LEDC,  $(\text{LiOCOOCH}_2)_2$ ) gave high-resolution diffraction peaks, yet the structure could not be determined by XRD alone. Despite the increased intensity of the synchrotron X-rays, the weak X-ray scattering ability of low-Z elements like lithium poses challenges to determine their accurate positions in the crystal structure. Neutron diffraction is another diffraction technique that could resolve this challenge. Unlike X-rays, neutrons do not interact with electrons but with nucleus (nucleus spin to be more specific), and the scattering ability of atomic nucleus does not increase with atomic mass.<sup>92</sup> In fact, low-Z elements (hydrogen, lithium, etc.) contribute significantly to the neutron diffraction pattern. This information will complement the diffraction information obtained from the synchrotron X-ray measurement and help resolve the accurate atomic coordinates in LEDC crystal.

The lithium ethylene dicarbonate (LEDC) – dimethylformamide (DMF) film here primarily characterized by UHV-STM as the structure of the DMF solvent, with LEDC solute embedded at low densities. The greater adsorption of DMF prevented the observation of LEDC network structures. A polar solvent that could dissolve LEDC but weakly interact with Ag(111) is needed. An alternative choice for liquid microaerosol deposition is using acetonitrile (ACN,  $\text{CH}_3\text{CN}$ ). ACN has lower vapor pressure compared to dimethylformamide (DMF) and the coordination ability between N-Ag is weaker (vs. O-Ag coordination). A new model system lithium

ethylene dicarbonate (LEDC) – acetonitrile (ACN) / Ag(111) leads to the possibility of directly imaging lithium ethylene dicarbonate (LEDC) on Ag(111).

In a broader sense, this dissertation revealed how the polar organic solvent molecules-ionic solute interactions can drive film structures at electrode surfaces. Such phenomena are ever present in a battery interface and must be understood to be harnessed for improved battery performance.

## Appendices

## Appendix A. Temperature Calibration of the Constructed TPD/TPRS System

In the constructed TPD/TPRS system, the temperature sensor is not attached directly to the graphite surface so that samples can be easily exchanged without breaking vacuum. The temperature in the TPD/TPRS system is measured at the copper support for the sample plate, and must thus be calibrated to obtain absolute values for the graphite surface temperature. The following procedure was used for graphite surface temperature calibration of the constructed TPD/TPRS system, described in Sec. 2.3.2 and utilized in Chapter 3 studies of molecular carbonates on lithiated graphite substrates:

(1) Temperature calibration standards for graphite surfaces were provided from the literature report of alkane temperature programmed desorption spectra from graphite surfaces at a ramp of 2 K/s [Paserba, K. R.; Gellman, A. J. *J. Chem. Phys.* **2001**, 115, 6737.]. In this literature study, a thermocouple was directly attached to a ~0.25 mm thick tantalum foil used to mount the graphite surface, providing accurate surface temperature values for desorption. The temperature values for the maximum monolayer desorption rates for C<sub>5</sub> (pentane) – C<sub>10</sub> (decane), provide convenient calibration standards in the temperature range from 164 K – 248 K, as summarized in Table A1;

(2) Using the Redhead analysis method, the maximum desorption rate for a monolayer of alkane (TPD spectrum peak) can be obtained for other linear ramp rates. Here 1 K/s is used as an example;

(3) The converted literature values (1 K/s here) were compared with the experimental values on the constructed system at the same ramp rate (1 K/s here) and a temperature calibration curve is generated.

**Table A1.** Literature Values\* of Multilayer and Monolayer Alkane (C<sub>5</sub>-C<sub>10</sub>) Desorption Temperature from Graphite

Alkanes	Multilayer Peak Location (K)	Monolayer Peak Location@2 K/s (K)
Pentane (C <sub>5</sub> H <sub>12</sub> )	133	164
Heptane (C <sub>7</sub> H <sub>16</sub> )	154	211
Octane (C <sub>8</sub> H <sub>18</sub> )	171	220
Decane (C <sub>10</sub> H <sub>22</sub> )	193	248

\*Paserba, K. R.; Gellman, A. J. *J. Chem. Phys.* **2001**, 115, 6737.

In my TPD/TPRS studies of Chapter 3, the temperature ramp rate used is 1 K/s.

The literature values are thus converted to values at 1 K/s based on the Redhead analysis method described in [Redhead, P.A. *Vacuum* **1962**, 12, 203].

For first-order desorption, the ion signal I is proportional to the desorption rate – dθ/dT, and the desorption rate is described by the following equation:

$$I \propto -\frac{d\theta}{dT} = \frac{1}{\beta} v \cdot \exp\left(-\frac{E_{ad}}{RT}\right) \theta, \quad \text{Eq. (A1.1)}$$

At the peak in the desorption spectrum, T=Tp, the change in desorption rate becomes zero:

$$\frac{d}{dT} \left[ -\frac{d\theta}{dT} \right] = \frac{d}{dT} \left[ \frac{1}{\beta} v \cdot \exp\left(-\frac{E_{ad}}{RT}\right) \theta \right] = 0, \quad \text{Eq. (A1.2)}$$

Eq. (A1.2) thus becomes

$$\frac{E_{ad}}{RT^2} \left[ \frac{1}{\beta} v \cdot \exp\left(-\frac{E_{ad}}{RT}\right) \theta \right] + \left[ \frac{1}{\beta} v \cdot \exp\left(-\frac{E_{ad}}{RT}\right) \right] \frac{d\theta}{dT} = 0, \quad \text{Eq. (A1.3)}$$

Substituting Eq. (A1.1) into dθ/dT in Eq. (A1.3) gives,

$$\left[ \frac{1}{\beta} v \cdot \exp\left(-\frac{E_{ad}}{RT}\right) \theta \right] \left[ \frac{E_{ad}}{RT^2} - \frac{1}{\beta} v \cdot \exp\left(-\frac{E_{ad}}{RT}\right) \right] = 0 \quad \text{Eq. (A1.4)}$$



The term in the first square bracket in Eq. (A1.4) has a non-zero value, and the term in the second square bracket must therefore be zero. Thus

$$\frac{E_{ad}}{RT^2} = \frac{1}{\beta} v \cdot \exp\left(-\frac{E_{ad}}{RT}\right) \quad Eq.(A1.5)$$

For the same desorption process, R,  $E_{ad}$  and  $v$  are constant, and the difference in ramp rate  $\beta$  results in different peak temperature  $T_p$ . Assuming two different ramp rate  $\beta_1$  and  $\beta_2$ , there will be two different peak temperature  $T_{p1}$  and  $T_{p2}$ . Substituting  $\beta_1$ ,  $\beta_2$ ,  $T_{p1}$  and  $T_{p2}$  into Eq.(A1.5) gives:

$$\frac{E_{ad}}{RT_{p1}^2} = \frac{1}{\beta_1} v \cdot \exp\left(-\frac{E_{ad}}{RT_{p1}^2}\right) \quad Eq.(A1.6)$$

and

$$\frac{E_{ad}}{RT_{p2}^2} = \frac{1}{\beta_2} v \cdot \exp\left(-\frac{E_{ad}}{RT_{p2}^2}\right) \quad Eq.(A1.7)$$

Dividing Eq. (A1.6) by Eq. (A1.7) gives:

$$\frac{T_{p2}^2}{T_{p1}^2} = \frac{\beta_2}{\beta_1} \cdot \exp\left[\frac{E_{ad}}{R} \left(-\frac{1}{T_{p1}^2} + \frac{1}{T_{p2}^2}\right)\right] \quad Eq.(A1.8)$$

Eq. (A1.8) allows us to calculate the peak temperature  $T_{p2}$  if  $T_{p1}$ ,  $\beta_2$  and  $\beta_1$  are known.

Applying Eq. (A1.8) to calculate the peak temperature  $T_{p2}$  at  $\beta_2 = 1$  K/s for alkanes C<sub>5</sub>-C<sub>10</sub> yields the calculated values summarized in Table A2.

**Table A2.** Literature-Values and Raw Experimental Values for Monolayer Alkane (C<sub>5</sub>-C<sub>10</sub>) Peak Desorption Temperature (K) from Graphite at 1K/s Ramp Rate

Alkanes	Monolayer Peak Desorption Maximum from Redhead-computed Literature Values	Measured Values for the Monolayer Peak Desorption Maximum in the TPD/TPRS System prior to Calibration	Calibrated values of TPD/TPRS System from Eq. (4.1.9)
Pentane (C <sub>5</sub> H <sub>12</sub> )	162	144	162
Heptane (C <sub>7</sub> H <sub>16</sub> )	208	179	206
Octane (C <sub>8</sub> H <sub>18</sub> )	217	189	218
Decane (C <sub>10</sub> H <sub>22</sub> )	244	211	245

Based on the literature desorption values of C<sub>5</sub> (pentane)-C<sub>10</sub> (decane), obtained by Redhead conversion to a ramp rate of 1K/s, and our own directly measured values of C<sub>5</sub>(pentane)-C<sub>10</sub> (decane) acquired at the same 1 K/S ramp rate., the following temperature calibration curve was generated:

$$T = 1.2312T_0 - 14.843 \quad (R^2 = 0.9973), \quad \text{Eq. (A1.9)}$$

where T is the calibrated temperature and T<sub>0</sub> is the original experimental value prior to calibration. Based upon this approach, the maximum error in graphite surface temperature in the TPD/TPRS system at a ramp rate of 1K/s is 2 K. This method could also be used to generate temperature calibration curve at other linear temperature ramp rates.

## Appendix B. The MATLAB Code for the TPD/TPRS Kinetics

### Simulation Utilizing the Runge–Kutta Numerical Integration Method

File name: ratelaw.m

```
function [ rate ] = ratelaw ( theta, T, A, Ed )
%rate law gives the reaction rate for certain surface
coverage

R = 8.314;
rate = -A * theta * exp(-Ed/(R*T));
%first-order desorption kinetics for monolayer desorption

end
```

File name: ramp.m

```
function [ Tp, fwhm ] = ramp( theta0, beta, A, Ed )
%ramp solves the surface differential equation using RK4
%a constant heating rate is assumed over Tlow < T <Thigh
%the peak desorption temperature and fwhm are solved
using peakprop
%-----

%temperature step of RK4 in Kelvin
tempstep = 0.01;

%time step of RK4 in seconds
h = tempstep/beta;

%low and high temperature bounds in K
Tlow = 100;
Thigh = 300;

%lower bound for rate values to prevent number system
looping at ~ 10^-308
lub = 10^-60;

N = round((Thigh-Tlow)/tempstep)+1;

T = zeros(N,1);
rate = zeros(N,1);
```

```

%temperature profile
for i = 1:N
    T(i) = Tlow + (i-1)*tempstep;
end

rate(1) = -1*ratelaw(theta0, T(1), A, Ed);
thetaprev = theta0;

for j = 2:N
    k1 = ratelaw(thetaprev, T(j-1), A, Ed);

    thetak1 = thetaprev + 0.5*h*k1;
    Thalf = T(j-1) + 0.5*(T(j)-T(j-1));

    if (thetak1 >= 0)
        k2 = ratelaw(thetak1, Thalf, A, Ed);
    else
        k2 = 0;
    end

    thetak2 = thetaprev + 0.5*h*k2;

    if (thetak2 >= 0)
        k3 = ratelaw(thetak2, Thalf, A, Ed);
    else
        k3 = 0;
    end

    thetak3 = thetaprev + h*k3;

    if (thetak3 >= 0)
        k4 = ratelaw(thetak3, T(j), A, Ed);
    else
        k4 = 0;
    end

    thetatest = thetaprev + 1/6 * h * (k1 + 2*k2 + 2*k3 +
k4) ;

    if( (thetaprev ~= 0) || (thetatest >= 0) || (k2 <= 0)
|| (k3 <= 0) || (k4 <= 0))
        thetacurr = thetatest;
    else
        thetacurr = 0;
    end

    if (rate(j-1)>=lub)

```

```

        rate(j) = -1*ratelaw(thetacurr, T(j), A, Ed);
    else
        rate(j) = 0;
    end

    thetaprev = thetacurr;
end

[Tp, fwhm] = peakprop(T,rate);

End

```

Filename: peakprop.m

```

function [ xpeak, fwhm ] = peakprop( x,y )
%peakprop finds the peak location and full width at half
maximum
%-----

N = length(x);

ymax = max(y);

for i = 1:N
    if ( y(i)== ymax)
        ipeak = i;
        xpeak = x(i);
    end
end

left = 0;
right = 0;

%finds indices of vector one step right of half max on
each peak side
for j = 1:N
    if( (left == 0) && (j < ipeak) && (y(j) >0.5*ymax) )
        left = j;
    end

    if( (right == 0) && (j > ipeak) && (y(j) < 0.5*ymax)
)
        right = j;
    end
end
end

```

```


```

%prevents a divide by 0 error near right endpoint
%also results in fwhm = 0 as trigger flag
if ( right == N )
    left=round(N/2);
    right=round(N/2);
end

%prevents later referencing index 0
if ( left <= 1)
    left = 2;
end

if ( right <= 1)
    right = 2;
end

%interpolates values above and below 0.5*ymax on each
side of peak
xleft = x(left-1)+(0.5*ymax-y(left-1))*(x(left)-x(left-
1))/(y(left)-y(left-1));
xright = x(right-1)+(0.5*ymax-y(right-1))*(x(right)-
x(right-1))/(y(right)-y(right-1));

fwhm = xright - xleft

end

```


```

Filename: peakfit.m

```

function [ error ] = peakfit( x )
%peakfit calculates model values and compares to
experimental TPD data sets
%-----

%scale factors for parameters
scaleA = 1;
scaleEd = 10000;

A = scaleA*10^(x(1));
Ed = scaleEd*x(2);

%coverage varying results
covg1 = xxx.xx;
%xxx.xx is the coverage value to be entered

Tplcovgdata = xxx.xx;
%xxx.xx is the peak temperature to be entered

```

```

w1covgdata = xxx.xx;
%xxx.xx is the peak width to be entered

%calculate covg varying model values
[Tp1covgmodel, w1covgmodel] = ramp(covg1, 1, A, Ed);

%coverage Tp errors
error(1) = (Tp1covgdata - Tp1covgmodel)/Tp1covgdata;

%coverage width errors
error(2) = log(w1covgdata/w1covgmodel)/log(w1covgdata);

end

```

Filename: optimizefit.m

```

%optimizes TPD data fits

%initial guess
%x0(1) = log(A)/scaleA
%x0(2) = Ed/scaleEd
%scaleA = 1, scaleEd = 10000
z0 = [44 6.7925];
lb = [43.75 1];
ub = [48.35 10];

%nonlinear least squares
[z, resnorm] =
lsqnonlin(@peakfit,z0,lb,ub,optimset('DiffMinChange',1e-
4,'DiffMaxChange',1e-1,'Display','iter','MaxIter',100));

```

## Appendix C

### Representative Cracking Products of Gases Released from the Decomposition of EC Reduction Products during TPRS

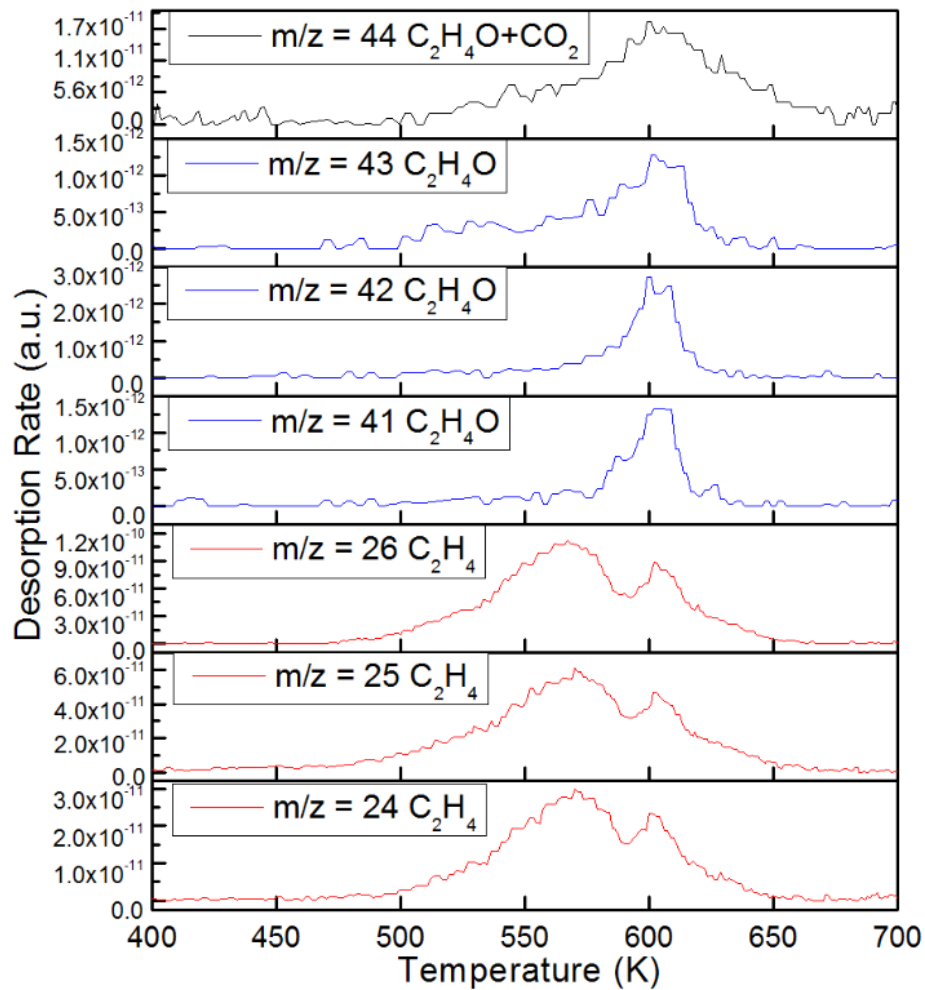


**Figure C1.** The cracking products of  $m/z = 24-26$  and  $m/z = 41-44$  shown in the high temperature range (400 K – 700 K) confirm the identity of the released gaseous products ethylene, ethylene oxide and  $CO_2$ .



## Desorption of Minor Products Organic Ethylene Glycols

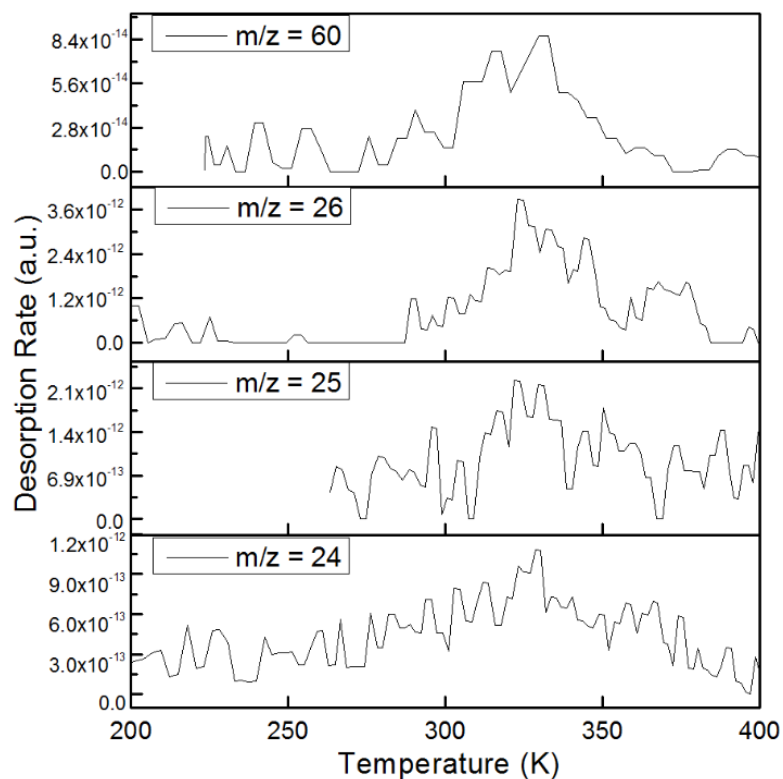


**Figure C2.** The cracking products from  $m/z = 24-26$  and  $m/z = 60$  shown in the low temperature range (200 K – 400 K) due to very small amounts of organic ethylene glycols. Peak areas indicate glycols account for 1.1% of EC decomposition as determined by the calibration process described below. The same scaling for desorption rate is used in Figure C1.

## Desorption of Minor Products Organic Ethylene Glycols Detailed Mass Balance Analysis of EC Decomposition Products Measured by Temperature Programmed Reaction Spectroscopy (TPRS)

Absolute coverages of the reduction products LEDC and LEC are determined from the integrated TPRS peak areas of gases released by decomposition via the relation:

$$\theta_{\text{abs}} = r \cdot g \cdot s \cdot A,$$

where  $\theta_{\text{abs}}$  is the absolute coverage,  $r$  the relative ionization gauge gas correction factor,  $g$  the geometric scaling factor,  $s$  the gas sensitivity factor and  $A$  the area of the TPRS peak. The integrated peak area of each TPRS peak is determined following a linear background subtraction. The ethylene oxide TPRS spectrum has a single peak so the integral is a simple sum. The ethylene TPRS spectrum has two overlapping peaks, which were fit with asymmetric logistic peaks, as shown below (Figure C3), for integration by simple summation.

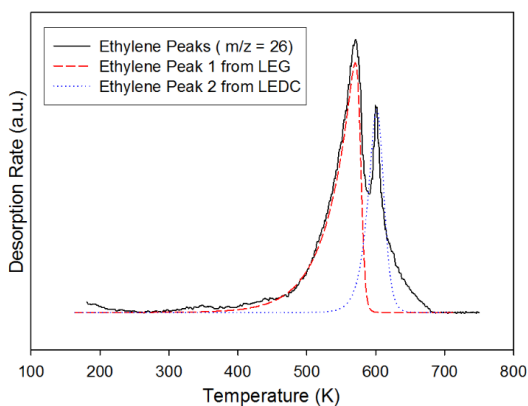


**Figure C3.** Ethylene TPRS spectrum contains two peaks, fit with two asymmetric logistic functions. Integrated areas of the functions (TPRS peaks) are provided in Table C1.

**Table C1.** TPRS Peak Areas for EC Coverage of 1.5 L

	ethylene peak 1	ethylene peak 2	ethylene oxide peak
mass to charge ratio (m/z)	26	26	43
peak maximum temperature (K)	570	600	600
peak area	$6.7 \times 10^{-9} \pm$ $1.2 \times 10^{-9}$	$3.3 \times 10^{-9} \pm$ $0.5 \times 10^{-9}$	$5.3 \times 10^{-11} \pm$ $0.3 \times 10^{-11}$

We next relate the integrated areas of the TPRS features to coverage by determining the ion gauge sensitivity factor,  $s$ . This is done by establishing an empirical relationship between the partial pressure of the gas of interest (measured by the nude Bayer-Albert ion gauge) and the ion mass signal (measured by the mass spectrometer) to give the mass sensitivity factor(s) for each gas. This was done at mass 26 for Ethylene and mass 43 for both Ethylene Oxide and Ethylene Carbonate. These empirical relationships are shown below. (Figure C4)

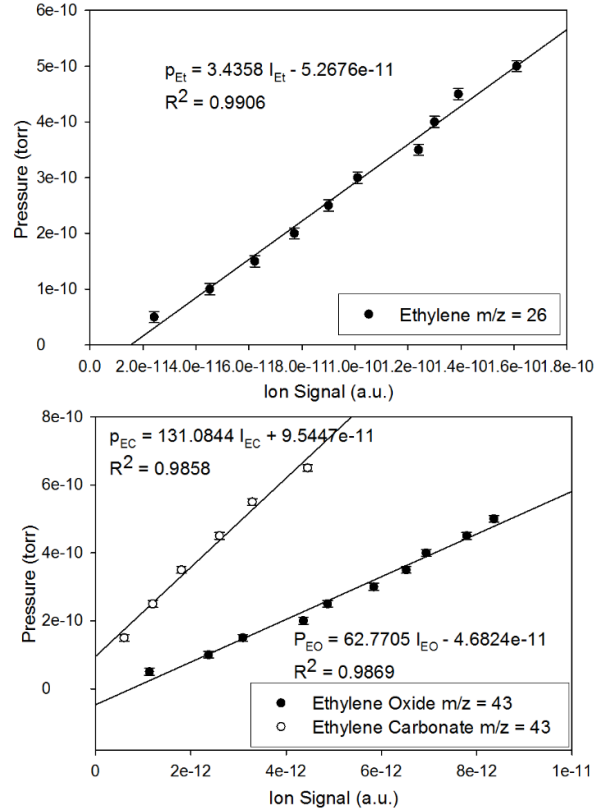


**Figure C4.** The sensitivity factors  $s$  for ethylene, ethylene oxide and ethylene carbonate are obtained through calibration curve of ion signal  $I$  vs. pressure  $p$  measured by the ionization gauge calibrated for nitrogen.

Based upon the above empirical relationship between mass spectrometry ion signal and partial pressure, we can express the integrated area of each desorption peak in exposure units of torr·s. (Table C2, Row 2). This step is simply:

$$\text{Raw Coverage} = s \cdot A$$

Furthermore, in an actual TPD measurement, we collect only a fraction of the desorbing ions due to the sampling geometry. We can determine this geometric sampling factor  $g$  directly by measuring the TPD of EC for precisely determined exposures. An exposure of 1.5 L EC, gives rise to a measured TPD area of  $1.9 \times 10^{-10}$

torr·s. The geometric scaling factor  $g$  (which is attenuating) is thus determined to be 12 (Table C2).

**Table C2.** The Determination of Geometric Sampling Factor  $g$

deposition Amount	TPD peak area	raw coverage (torr·s)	deposition exposure (torr·s)	scaling factor
EC 1.5 L	$1.9 \times 10^{-10}$	$3.4 \times 10^{-8}$	$4.0 \times 10^{-7}$	12

Finally, in order to obtain absolute coverages, we account for the different relative ionization gauge correction factor  $r$  for each gas. These values have been previously determined as 2.3 for  $C_2H_4$  and 2.5 for  $(CH_2)_2O$ .<sup>93</sup> For ethylene carbonate, this value was approximated to be 3.8 from the parametric dependence of the relative ionization gauge factor on molecular polarizability<sup>93-96</sup>, as shown in Figure C5.

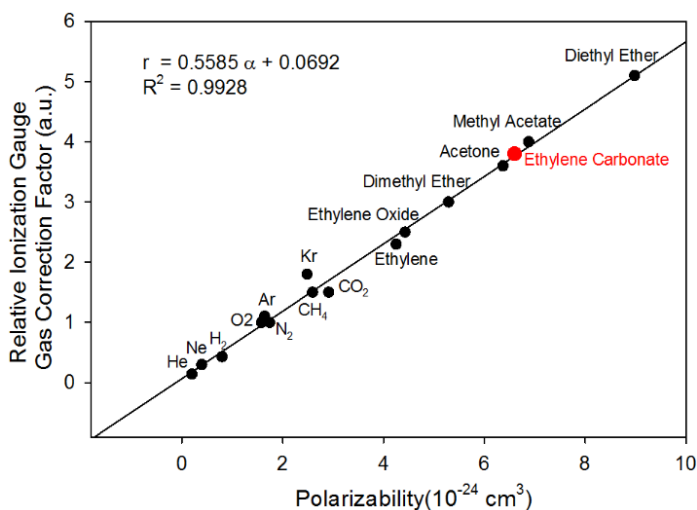


**Figure C5.** Determination of ethylene carbonate relative ionization gauge gas correction factor by the polarizability  $\alpha$  vs. relative ionization gauge gas correction factors  $r$  relation graph. The  $r = 3.8$  for ethylene carbonate is interpolated from the  $\alpha$  vs.  $r$  relation.

With g, s and r determined, we obtain the absolute coverage of EO and Et, as reported in Table C3.

**Table C3.** Determination of Absolute Coverages for Different Species from Measured TPRS Peak Areas (Based upon 1.5 L of EC Decomposition on Li(s)/C(0001))\*

desorption species	ethylene@570 K	ethylene@600 K	ethylene oxide @600 K	No desorption
source product	LEDC	LEG	LEG	Li <sub>2</sub> CO <sub>3</sub>
reaction pathway	2e <sup>-</sup>	2e <sup>-</sup>	2e <sup>-</sup>	2e <sup>-</sup>
peak area	6.7×10 <sup>-9</sup> ± 1.2×10 <sup>-9</sup>	3.3×10 <sup>-9</sup> ± 0.5×10 <sup>-9</sup>	5.3×10 <sup>-11</sup> ± 0.3×10 <sup>-11</sup>	not applicable
raw coverage conversion (torr·s)	2.3×10 <sup>-8</sup> ± 0.4×10 <sup>-8</sup>	1.1×10 <sup>-8</sup> ± 0.2×10 <sup>-8</sup>	3.3×10 <sup>-9</sup> ± 0.2×10 <sup>-9</sup>	
geometric scaling factor	12			
geometric factor scaled coverage (torr·s)	2.8×10 <sup>-7</sup> ± 0.5×10 <sup>-7</sup>	1.3×10 <sup>-7</sup> ± 0.2×10 <sup>-7</sup>	4.0×10 <sup>-8</sup> ± 0.3×10 <sup>-8</sup>	
relative ionization gauge gas correction factor	2.3	2.3	2.5	
absolute coverage (10 <sup>-6</sup> torr·s or L)	0.64 ± 0.12	0.30 ± 0.05	0.10 ± 0.01	0.5 ± 0.2

\* The minority product organic ethylene glycols (1.1%, 0.016 L assuming the same parameters as ethylene) is not included in the table.

The absolute surface coverage of ethylene carbonate (1.5 L) undergoes complete decomposition. The calibrated desorption products ethylene and ethylene oxide, provide quantitation of the EC reduction products LEDC and LEG, as summarized in Table C3. The inorganic reduction product Li<sub>2</sub>CO<sub>3</sub> is thermally stable up to ~1000°C and does not release desorption products over the monitored thermal window (110 K

– 900 K). The amount of the  $\text{Li}_2\text{CO}_3$  is thus determined by detailed mass balancing as the difference between the amount of deposited EC and the amount of evolved ethylene and ethylene oxide following the deposition. The amount of ethylene glycols observed in these monolayer studies (Figure C2) correspond to only 1.1% of the exposed EC, and thus is neglected in this detailed mass analysis.

## Bibliography

- (1) *Key World Energy Statistics 2015*, International Energy Agency, 2015.
- (2) Peltier, W. R.; Tushingham, A. M. *Science* **1989**, *244*, 806.
- (3) Vermeer, M.; Rahmstorf, S. *Proc. Natl. Acad. Sci. U. S. A.* **2009**, *106*, 21527.
- (4) Emanuel, K. *Nature* **2005**, *436*, 686.
- (5) Meehl, G. A.; Tebaldi, C. *Science* **2004**, *305*, 994.
- (6) Chen, H.; Cong, T. N.; Yang, W.; Tan, C.; Li, Y.; Ding, Y. *Prog. Nat. Sci.* **2009**, *19*, 291.
- (7) Tarascon, J. M.; Armand, M. *Nature* **2001**, *414*, 359.
- (8) Han, X.; Ouyang, M.; Lu, L.; Li, J. *Energies* **2014**, *7*, 4895.
- (9) Lide, D. R. *CRC Handbook of Chemistry and Physics, 87th Edition* **2006**.
- (10) Whittingham, M. S. *Science* **1976**, *192*, 1126.
- (11) Whittingham, M. S.; Chalcogenide Battery. U.S. Patent 4009052, Feb 22, 1977.
- (12) Mizushima, K.; Jones, P. C.; Wiseman, P. J.; Goodenough, J. B. *Mater. Res. Bull.* **1980**, *15*, 783.
- (13) Goodenough, J. B.; Park, K.-S. *JACS* **2013**, *135*, 1167.
- (14) Tarascon, J. M. *Phil. Trans. R. Soc. A: Math., Phys. Eng. Sci.* **2010**, *368*, 3227.
- (15) Bourderau, S.; Brousse, T.; Schleich, D. M. *J. Power Sources* **1999**, *81–82*, 233.
- (16) Wachtler, M.; Besenhard, J. O.; Winter, M. *J. Power Sources* **2001**, *94*, 189.
- (17) David, L.; Bhandavat, R.; Barrera, U.; Singh, G. *Nat Commun* **2016**, *7*.
- (18) Boukamp, B. A.; Lesh, G. C.; Huggins, R. A. *J. Electrochem. Soc.* **1981**, *128*, 725.
- (19) Chan, C. K.; Peng, H.; Liu, G.; McIlwrath, K.; Zhang, X. F.; Huggins, R. A.; Cui, Y. *Nat Nano* **2008**, *3*, 31.
- (20) Wang, C. S.; Wu, G. T.; Zhang, X. B.; Qi, Z. F.; Li, W. Z. *J. Electrochem. Soc.* **1998**, *145*, 2751.
- (21) Matsuoka, O.; Hiwara, A.; Omi, T.; Toriida, M.; Hayashi, T.; Tanaka, C.; Saito, Y.; Ishida, T.; Tan, H.; Ono, S. S.; Yamamoto, S. *J. Power Sources* **2002**, *108*, 128.
- (22) Jeong, S.-K.; Inaba, M.; Mogi, R.; Iriyama, Y.; Abe, T.; Ogumi, Z. *Langmuir* **2001**, *17*, 8281.
- (23) MacGlashan, G. S.; Andreev, Y. G.; Bruce, P. G. *Nature* **1999**, *398*, 792.
- (24) Kamaya, N.; Homma, K.; Yamakawa, Y.; Hirayama, M.; Kanno, R.; Yonemura, M.; Kamiyama, T.; Kato, Y.; Hama, S.; Kawamoto, K.; Mitsui, A. *Nat. Mater.* **2011**, *10*, 682.
- (25) Lei, J.; Li, L.; Kostecky, R.; Muller, R.; McLarnon, F. *J. Electrochem. Soc.* **2005**, *152*, A774.
- (26) Nie, M.; Chalasani, D.; Abraham, D. P.; Chen, Y.; Bose, A.; Lucht, B. L. *J. Phys. Chem. C* **2013**, *117*, 1257.
- (27) Goodenough, J. B. A., H. D. ;Buchanan, M. V. *Report of the Basic Energy Sciences Workshop on Electrical Energy Storage, April 2-4, 2007* **2007**.



- (28) Xu, K. *Chem. Rev.* **2004**, *104*, 4303.
- (29) Zhuang, G. V.; Xu, K.; Yang, H.; Jow, T. R.; Ross, P. N. *J. Phys. Chem. B* **2005**, *109*, 17567.
- (30) Tskipuri, L.; Shao, Q.; Reutt-Robey, J. *J. Vac. Sci. Technol. A* **2012**, *30*, 031402.
- (31) Prutton, M. *Introduction to Surface Physics*; Oxford University Press: New York, United States, 1994.
- (32) Paserba, K. R.; Gellman, A. J. *J. Chem. Phys.* **2001**, *115*, 6737.
- (33) Redhead, P. A. *Vacuum* **1962**, *12*, 203.
- (34) Binnig, G.; Rohrer, H.; Gerber, C.; Weibel, E. *Phys. Rev. Lett.* **1982**, *49*, 57.
- (35) Kuk, Y.; Silverman, P. J. *Rev. Sci. Instrum.* **1989**, *60*, 165.
- (36) Tersoff, J.; Hamann, D. R. *Phys. Rev. B* **1985**, *31*, 805.
- (37) Arora, P.; White, R. E.; Doyle, M. *J. Electrochem. Soc.* **1998**, *145*, 3647.
- (38) Xu, K. *Energies* **2010**, *3*, 135.
- (39) Peled, E. *J. Electrochem. Soc.* **1979**, *126*, 2047.
- (40) Aurbach, D.; Ein-Eli, Y.; Chusid, O.; Carmeli, Y.; Babai, M.; Yamin, H. *J. Electrochem. Soc.* **1994**, *141*, 603.
- (41) Verma, P.; Maire, P.; Novák, P. *Electrochim. Acta* **2010**, *55*, 6332.
- (42) McMillan, R.; Slegel, H.; Shu, Z. X.; Wang, W. *J. Power Sources* **1999**, *81–82*, 20.
- (43) Zhuang, G. V.; Yang, H.; Ross, P. N.; Xu, K.; Jow, T. R. *Electrochem. Solid-State Lett.* **2006**, *9*, A64.
- (44) Xu, K.; Zhuang, G. V.; Allen, J. L.; Lee, U.; Zhang, S. S.; Ross, P. N.; Jow, T. R. *J. Phys. Chem. B* **2006**, *110*, 7708.
- (45) Gireaud, L.; Grugeon, S.; Laruelle, S.; Pilard, S.; Tarascon, J.-M. *J. Electrochem. Soc.* **2005**, *152*, A850.
- (46) Gireaud, L.; Grugeon, S.; Pilard, S.; Guenot, P.; Tarascon, J.-M.; Laruelle, S. *Anal. Chem.* **2006**, *78*, 3688.
- (47) Gachot, G.; Grugeon, S.; Armand, M.; Pilard, S.; Guenot, P.; Tarascon, J.-M.; Laruelle, S. *J. Power Sources* **2008**, *178*, 409.
- (48) Andersson, A. M.; Edström, K. *J. Electrochem. Soc.* **2001**, *148*, A1100.
- (49) Sloop, S. E.; Kerr, J. B.; Kinoshita, K. *J. Power Sources* **2003**, *119–121*, 330.
- (50) Barth, J. V. *Annu. Rev. Phys. Chem.* **2007**, *58*, 375.
- (51) Bartels, L. *Nat Chem* **2010**, *2*, 87.
- (52) Maksymovych, P.; Sorescu, D. C.; Yates, J. T. *Phys. Rev. Lett.* **2006**, *97*, 146103.
- (53) Feng, Z.; Velari, S.; Cossaro, A.; Castellarin-Cudia, C.; Verdini, A.; Vesselli, E.; Dri, C.; Peressi, M.; De Vita, A.; Comelli, G. *ACS Nano* **2015**, *9*, 8697.
- (54) Rodríguez-Fernández, J.; Lauwaet, K.; Herranz, M. Á.; Martín, N.; Gallego, J. M.; Miranda, R.; Otero, R. *J. Chem. Phys.* **2015**, *142*, 101930.
- (55) Lin, N.; Dmitriev, A.; Weckesser, J.; Barth, J. V.; Kern, K. *Angew. Chem. Int. Ed.* **2002**, *41*, 4779.
- (56) Schlickum, U.; Decker, R.; Klappenberger, F.; Zoppellaro, G.; Klyatskaya, S.; Ruben, M.; Silanes, I.; Arnau, A.; Kern, K.; Brune, H.; Barth, J. V. *Nano Lett.* **2007**, *7*, 3813.

- (57) Kühne, D.; Klappenberger, F.; Decker, R.; Schlickum, U.; Brune, H.; Klyatskaya, S.; Ruben, M.; Barth, J. V. *JACS* **2009**, *131*, 3881.
- (58) Liu, J.; Lin, T.; Shi, Z.; Xia, F.; Dong, L.; Liu, P. N.; Lin, N. *JACS* **2011**, *133*, 18760.
- (59) Wurster, B. Ph.D. Dissertation, EPFL, 2015.
- (60) Albert, M. R.; Yates, J. T. *The Surface Scientist's Guide to Organometallic Chemistry*; American Chemical Society: Washington D.C., USA, 1987.
- (61) Zhou, J.; Wang, J.; Han, J.; He, D.; Yang, D.; Xue, Z.; Liao, Y.; Xie, X. *RSC Advances* **2015**, *5*, 43724.
- (62) Brozek, C. K.; Michaelis, V. K.; Ong, T.-C.; Bellarosa, L.; López, N.; Griffin, R. G.; Dincă, M. *ACS Cent. Sci.* **2015**, *1*, 252.
- (63) Hanabusa, K.; Hiratsuka, K.; Kimura, M.; Shirai, H. *Chem. Mater.* **1999**, *11*, 649.
- (64) Máca, J.; Libich, J.; Sedlarikova, M.; Vondrak, J.; Fedorkova, A. S. *Int. J. Electrochem. Sci.* **2015**, *10*, 5264.
- (65) Nečas, D.; Klapetek, P. *Cent. Eur. J. Phys.* **2012**, *10*, 181.
- (66) Kresse, G.; Furthmüller, J. *Phys. Rev. B* **1996**, *54*, 11169.
- (67) Kresse, G.; Furthmüller, J. *Comput. Mater. Sci.* **1996**, *6*, 15.
- (68) Kresse, G.; Joubert, D. *Phys. Rev. B* **1999**, *59*, 1758.
- (69) Perdew, J. P.; Burke, K.; Ernzerhof, M. *Phys. Rev. Lett.* **1996**, *77*, 3865.
- (70) Dion, M.; Rydberg, H.; Schröder, E.; Langreth, D. C.; Lundqvist, B. I. *Phys. Rev. Lett.* **2004**, *92*, 246401.
- (71) Klimeš, J.; Bowler, D. R.; Michaelides, A. *Phys. Rev. B* **2011**, *83*, 195131.
- (72) Román-Pérez, G.; Soler, J. M. *Phys. Rev. Lett.* **2009**, *103*, 096102.
- (73) Kaushik, V. K. *J. Electron. Spectrosc. Relat. Phenom.* **1991**, *56*, 273.
- (74) Gerenser, L. J. *J. Vac. Sci. Technol. A* **1990**, *8*, 3682.
- (75) Ohtaki, H.; Itoh, S.; Yamaguchi, T.; Ishiguro, S.-i.; Rode, B. M. *Bull. Chem. Soc. Jpn.* **1983**, *56*, 3406.
- (76) Zhou, X.; Krauser, J. A.; Tate, D. R.; VanBuren, A. S.; Clark, J. A.; Moody, P. R.; Liu, R. *J. Phys. Chem.* **1996**, *100*, 16822.
- (77) Classen, T.; Fratesi, G.; Costantini, G.; Fabris, S.; Stadler, F. L.; Kim, C.; de Gironcoli, S.; Baroni, S.; Kern, K. *Angew. Chem. Int. Ed.* **2005**, *44*, 6142.
- (78) Shi, Z.; Lin, N. *JACS* **2009**, *131*, 5376.
- (79) Hla, S.-W. *ACS Nano* **2015**, *9*, 8644.
- (80) Rusanov, A. I. *J. Chem. Phys.* **2004**, *120*, 10736.
- (81) Fainerman, V. B.; Lucassen-Reynders, E. H.; Miller, R. *Colloids Surf., A* **1998**, *143*, 141.
- (82) Stoltze, P. *J. Phys. Condens. Matter* **1994**, *6*, 9495.
- (83) Fox, B. S.; Beyer, M. K.; Bondybey, V. E. *JACS* **2002**, *124*, 13613.
- (84) Tsutsui, Y.; Sugimoto, K.-i.; Wasada, H.; Inada, Y.; Funahashi, S. *J. Phys. Chem. A* **1997**, *101*, 2900.
- (85) Wang, Y.; Nakamura, S.; Ue, M.; Balbuena, P. B. *JACS* **2001**, *123*, 11708.
- (86) Borodin, O.; Zhuang, G. V.; Ross, P. N.; Xu, K. *J. Phys. Chem. C* **2013**, *117*, 7433.
- (87) Xu, K.; Zhuang, G. V.; Allen, J. L.; Lee, U.; Zhang, S. S.; Ross, P. N.; Jow, T. R. *J. Phys. Chem. B* **2006**, *110*, 7708.

- (88) Bruker, A. *User's Manual, Bruker AXS, Karlsruhe, Germany* **2005**.
- (89) Oxtoby, D. W. *Acc. Chem. Res.* **1998**, *31*, 91.
- (90) Volmer, M.; Weber, A. *Z. Phys. Chem.* **1925**, *119*, 277.
- (91) Becker, D.; Döring, W. *Ann. Phys.* **1935**, *24*, 719.
- (92) Fucke, K.; Steed, J. W. *Water* **2010**, *2*, 333.
- (93) Summers, R. L. *NASA Technical Note TN D-5285*, National Aeronautics and Space Administration, June 1969.
- (94) Holanda, R. *J. Vac. Sci. Technol.* **1973**, *10*, 1133.
- (95) Bosque, R.; Sales, J. J. *Chem. Inf. Comput. Sci.* **2002**, *42*, 1154.
- (96) *Handbook of Chemistry and Physics*; Lide, D. R., Ed.; CRC Press: Boca Raton, FL, 2006.